Naval Research Laboratory
Washington, DC 20375-5320

NRL/FR/7140--92-9391

Theory and Numerical Modeling of Low-Frequency Acoustic Scattering from Bubble Plumes Near the Sea Surface

R.F. GRAGG
D. WURMSER

Acoustic Systems Branch
Acoustics Division

December 18, 1992

REPORT DOCUMENTATION PAGE

Form Approved
OMB No. 0704-0188

1. AGENCY USE ONLY (*Leave Blank*)	2. REPORT DATE	3. REPORT TYPE AND DATES COVERED
	Decmeber 18, 1992	1992

4. TITLE AND SUBTITLE

Theory and Numerical Modeling of Low-Frequency Acoustic Scattering from Bubble Plumes Near the Sea Surface

5. FUNDING NUMBERS

PE - 62435N
PR - RJ35B01
WU - DN480-045

6. AUTHOR(S)

R. F. Gragg and D. Wurmser

7. PERFORMING ORGANIZATION NAME(S) AND ADDRESS(ES)

Naval Research Laboratory
Washington, DC 20375-5320

8. PERFORMING ORGANIZATION REPORT NUMBER

NRL/FR/7140--92-9391

9. SPONSORING/MONITORING AGENCY NAME(S) AND ADDRESS(ES)

Office of Naval Technology
Code 234
Arlington, VA 22217

Office of Naval Research
Code 11250A
Arlington, VA 22217

10. SPONSORING/MONITORING AGENCY REPORT NUMBER

11. SUPPLEMENTARY NOTES

12a. DISTRIBUTION/AVAILABILITY STATEMENT

Approved for public release; distribution unlimited.

12b. DISTRIBUTION CODE

13. ABSTRACT (*Maximum 200 words*)

From a theoretical foundation in boundary integral equations, we develop and implement a general method for computing the complex acoustic scattering amplitudes of bubble plumes near the sea surface. The implementation, named BIRPS (Boundary Integral Resonant Plume Scatter) incorporates surface-image and resonance effects, and allows user-specified plume shapes, interior sound speed functions, and depths. Simulations with model "intermediate" plumes reveal multiple sub-kHz resonant features. The resonance spectrum depends mainly on the plume's size, shape, and mean sound speed. The Q of a resonance depends on these parameters and on the sound speed gradient. Resonant scattering responses have a nonquadratic depth dependence and an elevation dependence whose complexity and frequency sensitivity increase with frequency. BIRPS may be joined with a continuous wave (CW) propagation model to proivde scattering simulations or with a multifrequency driver to generate reverberation predictions. Our results provide a theoretical/modeling component for the investigation of surface reverberation and are relevant to problems of resonant scattering from complex bodies in general.

14. SUBJECT TERMS

Resonance effects
Acoustic scattering
Complex scattering amplitude
Low-frequency surface reverberation
Near-surface bubble structures
Intermediate bubble plume

15. NUMBER OF PAGES

69

16. PRICE CODE

17. SECURITY CLASSIFICATION OF REPORT	18. SECURITY CLASSIFICATION OF THIS PAGE	19. SECURITY CLASSIFICATION OF ABSTRACT	20. LIMITATION OF ABSTRACT
UNCLASSIFIED	UNCLASSIFIED	UNCLASSIFIED	SAR

NSN 7540-01-280-5500

Standard Form 298 (Rev. 2-89)
Prescribed by ANSI Std 239-18
298-102

CONTENTS

THEORY AND NUMERICAL MODELING OF LOW-FREQUENCY ACOUSTIC SCATTERING FROM BUBBLE PLUMES NEAR THE SEA SURFACE

1. INTRODUCTION

In this report, we develop the physical theory and numerical techniques for modeling low-frequency scattering from acoustically penetrable bubble plumes, including surface-image and resonance effects. The model plumes can have arbitrary shapes, interior sound speed fields, and depths. In addition, a pressure relief boundary condition can be invoked at the air/sea interface, which is taken to be flat.

1.1 Background

At low sea states and frequencies, acoustic sea-surface reverberation is fundamentally just rough-surface scattering. However, there is now ample evidence that with increasing sea state and/or frequency, a second scattering process appears and eventually dominates. Reference 1 provides a complete review of the subject and we will not go further into the matter here except to say that it is now virtually certain that subsurface bubble structures are the scattering mechanism responsible. Even with that established, the acoustic situation remains somewhat unclear because scattering from such structures, particularly if they are resonant, is not well understood.

In the present context, "low frequency" simply means well below the resonant frequencies of the individual bubbles (e.g., $f < 900$ Hz, for 10-micron bubbles). In this regime, small concentrations of bubbles in the water (e.g., less than 1 % air by volume) have a negligible impact on the density but produce a dramatic increase in the medium's bulk compressibility (a sensitive function of the air volume fraction) and a commensurate reduction in sound speed [2, 3].

The work presented here was undertaken to clarify the scattering properties of one type of subsurface bubble structure, the so-called "intermediate bubble plume." These are localized collections of air bubbles that get injected into the surface scattering zone by plunging or breaking waves. They are characterized by void fractions on the order of 1% [4, 5] so that the interior sound speed may be as much as five times smaller than the sound speed outside. Because of these remarkably low interior sound speeds, intermediate bubble plumes can function as resonant cavities even at low frequencies. Only a few short-lived clouds of this type might be needed to produce a significant contribution to the scattering cross-section from near the ocean surface.

1.2 Approach

The essentials of our approach are all present in the standard treatment of one-dimensional scattering from a uniform object; i.e., a square well. Appendix A reviews the familiar solution

Manuscript approved May 29, 1992.

method: (a) write the fields inside and outside the scatterer as suitably general parameterized expressions, (b) impose physical continuity at the boundaries, (c) solve the boundary continuity conditions for the unknown parameters, and (d) insert these parameter values into the expression for the outgoing field far from the scatterer. Figure 1 shows the result of such a calculation for a well with a width of 3 m, exterior sound speed of 1500 m/s and interior sound speed of 100 m/s. The transmission coefficient is a smooth function of frequency punctuated by peaks where the internal resonances occur. The narrowness of these resonance peaks (i.e., the resonator's Q-factor) depends on the size of the object (i.e., the width of the well) and the sound speeds involved.

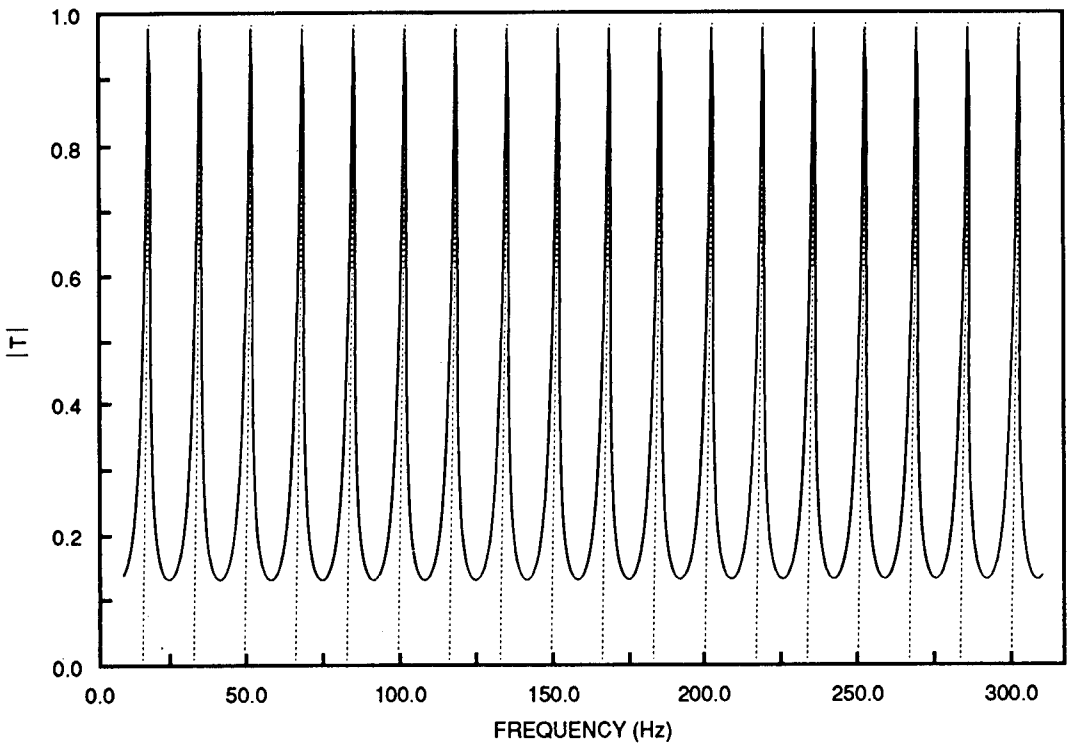

Fig. 1 – Magnitude of the transmission coefficient for a uniform 1-D object. Sound speeds: exterior 1500 m/s, interior 100 m/s; object size, 3 m. Dashed vertical lines are spaced at $\Delta f = 0.5 \times$ (interior speed)/(object size). See Appendix A for details.

The scattering problem in this report is much more complicated than that, but this complexity is really not fundamental: it is merely a byproduct of dealing in higher dimensions without the simplifying symmetry. In fact, the solution follows the same basic pattern. General expressions for the interior and exterior fields are given in terms of the Green's functions for the two regions. Physical continuity at the boundary is embodied in a pair of integral equations over the plume's surface. The solution of these boundary integral equations yields distributions of surface sources that, in effect, reradiate the scattered field. Finally, the far-field scattering amplitude appears as a surface integral over these equivalent distributions. The resulting spectra are qualitatively similar to Fig. 1, although the resonances are not nearly so sharp, regularly spaced, or uniform in height for realistic bubble plumes.

Our statement of the problem for this report has its limitations. Among these are the neglect of curvature and roughness in the sea surface (it is taken to be flat and smooth), time evolution of the plume itself, and very large interior sound speed gradients. By omitting these effects from

the current formulation we do not mean to dismiss them as unimportant. We are simply bounding the problem by deferring these components for consideration at a later time.

2. INTEGRAL FORMULATION

The plume's boundary is a surface $\mathcal{S}$ with outward normal direction $\hat{\mathbf{n}}$. The exterior region $\mathcal{E}$ has a constant sound speed and density. The interior $\mathcal{I}$ also has a constant density but its sound speed is a function of the air volume fraction and thus may vary from point to point. Since the sound speed throughout the bubbly water in $\mathcal{I}$ is lower than that of the normal water in $\mathcal{E}$ (Section 6), the opposite is true of the wavenumber $k = \omega/c$: its smallest values are found in the exterior. The situation is sketched in Figs. 2 and 3.

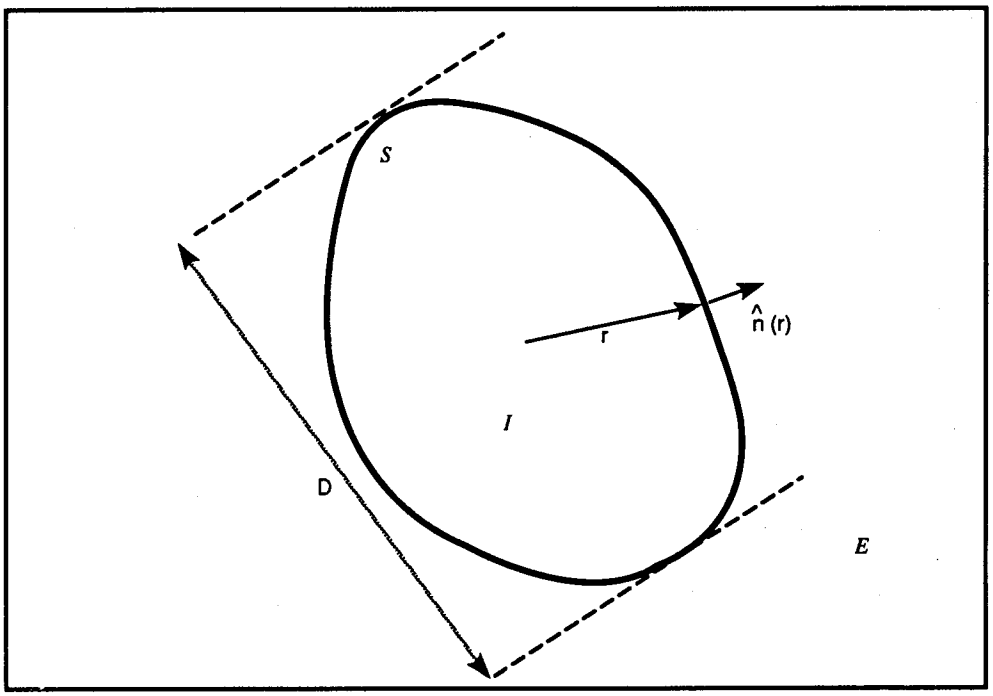

Fig. 2 – Sketch of a bubble plume showing its interior $\mathcal{I}$, exterior $\mathcal{E}$, surface $\mathcal{S}$, outward surface normal $\hat{\mathbf{n}}(\mathbf{r})$, and linear dimension D

If an actual sound speed discontinuity exists between bubbly and normal water, as shown on the right-hand side of Fig. 3 (a and b), that discontinuity marks the surface of the plume. If not, $\mathcal{S}$ may be taken to lie anywhere beyond the limit where c is effectively constant. (For that reason, the dotted line on the left-hand side of the figure could just as well be drawn farther to the left.) This report treats both the "sharp" and "fuzzy" boundary cases.

2.1 Equivalent Source Distributions

Kittappa and Kleinman [6] have used classical methods to formulate the boundary integral equations that govern continuous wave (CW) scattering from a penetrable body of very general shape. They allow the surface to have creases and corners, but restrict their attention to uniform homogeneous interiors. We, however, will focus on the contrasting case of a smooth surface and an inhomogeneous interior, since this more closely approximates the reality of bubble plumes in the

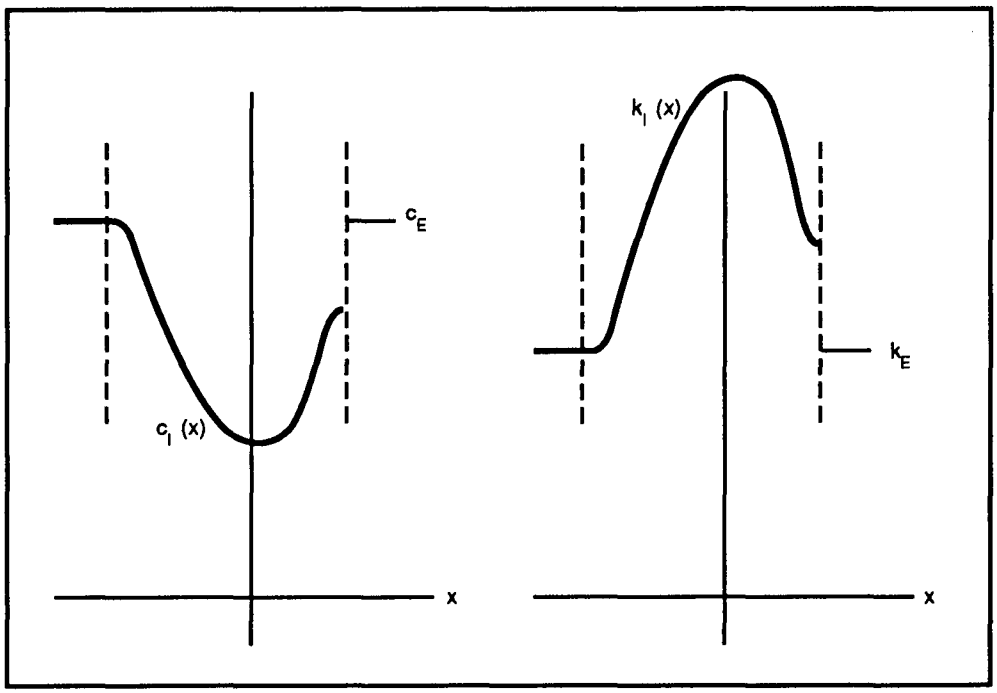

Fig. 3 – Sketches of sound speed and wavenumber as functions of one of the spatial coordinates. The dotted lines indicate the boundary surface $\mathcal{S}$.

ocean. By a straightforward adaptation of their approach to this case, one arrives at two integral equations, valid over the surface of the scatterer, that relate the total acoustic velocity potential U and its normal derivative V to their corresponding incident values U_{inc}, V_{inc}. These boundary integral equations are [6, Eqs. (3.5) and (3.19)]

$$U_{inc}(\mathbf{y}) + \int_{\mathcal{S}} dS(\mathbf{x})\,(A(\mathbf{x},\mathbf{y})U(\mathbf{x}) - B(\mathbf{x},\mathbf{y})V(\mathbf{x})) \;=\; (\bar{\rho}/\rho_{int})U(\mathbf{y}) \tag{1a}$$

and

$$V_{inc}(\mathbf{y}) + \int_{\mathcal{S}} dS(\mathbf{x})\,(C(\mathbf{x},\mathbf{y})U(\mathbf{x}) - D(\mathbf{x},\mathbf{y})V(\mathbf{x})) \;=\; (\bar{\rho}/\rho_{ext})V(\mathbf{y}) \tag{1b}$$

for $\mathbf{y} \in \mathcal{S}$, where $U(\mathbf{y})$ and $V(\mathbf{y})$ represent limiting values as $\mathbf{y} \to \mathcal{S}$ from within $\mathcal{E}$, the average of the two densities is denoted $\bar{\rho} = (\rho_{int} + \rho_{ext})/2$, and the kernels are

$$A(\mathbf{x},\mathbf{y}) \;=\; \frac{\partial}{\partial n(\mathbf{x})}\{G_{ext}(\mathbf{x},\mathbf{y}) - \;(\rho_{ext}/\rho_{int})\; G_{int}(\mathbf{x},\mathbf{y})\} \tag{2a}$$

$$B(\mathbf{x},\mathbf{y}) \;=\; \{G_{ext}(\mathbf{x},\mathbf{y}) - G_{int}(\mathbf{x},\mathbf{y})\} \tag{2b}$$

$$C(\mathbf{x},\mathbf{y}) \;=\; \frac{\partial^2}{\partial n(\mathbf{y})\partial n(\mathbf{x})}\{G_{ext}(\mathbf{x},\mathbf{y}) - G_{int}(\mathbf{x},\mathbf{y})\} \tag{2c}$$

$$D(\mathbf{x},\mathbf{y}) \;=\; \frac{\partial}{\partial n(\mathbf{y})}\{G_{ext}(\mathbf{x},\mathbf{y}) - \;(\rho_{int}/\rho_{ext})\; G_{int}(\mathbf{x},\mathbf{y})\} \tag{2d}$$

with '$\partial/\partial n$' indicating a derivative in the outward normal direction.

As observed in Ref. 6, the B kernel is always regular while C is weakly singular, i.e., it diverges as $\epsilon \equiv |\mathbf{x} - \mathbf{y}| \to 0$ but in a milder way than ϵ^{-2}, and A and D are at worst weakly

singular too. (In the familiar case where $\rho_{int} = \rho_{ext}$, A and D are regular.) Since the differential area element dS is proportional to ϵ^2, the integrals of C, A, and D are analytically well-behaved, though they are challenging numerically.

The field in the exterior region is the sum of incident and scattered parts, $U = U_{inc} + U_{sca}$, the scattered part being [6, Eq. (3.3) evaluated in the exterior]

$$U_{sca}(\mathbf{r}) = \int_{\mathcal{S}} dS(\mathbf{x}) \left(\partial G_{ext}(\mathbf{x},\mathbf{r})/\partial n(\mathbf{x})\, U(\mathbf{x}) - G_{ext}(\mathbf{x},\mathbf{r}) V(\mathbf{x}) \right) \tag{3}$$

for $\mathbf{r} \in \mathcal{E}$, in terms of the U, V surface data from Eq. (1). In this expression, the surface distributions U and V appear as monopole and dipole sources for the scattered field and are "equivalent source distributions" in that sense.

The field U_{inc} has thus far been left unspecified. Hereafter we focus our attention on the incident field from a point source at $\mathbf{s}$. With this choice and with the $\mathbf{s}$ dependence made explicit by writing $U(\mathbf{y}|\mathbf{s})$ and $V(\mathbf{y}|\mathbf{s})$, Eqs. (1) and (3) amount to the matrix equations

$$\begin{pmatrix} (\bar{\rho}/\rho_{int})U(\mathbf{y}|\mathbf{s}) \\ (\bar{\rho}/\rho_{ext})V(\mathbf{y}|\mathbf{s}) \end{pmatrix} + \int_{\mathcal{S}} dS(\mathbf{x}) \begin{pmatrix} -A(\mathbf{x},\mathbf{y}) & B(\mathbf{x},\mathbf{y}) \\ -C(\mathbf{x},\mathbf{y}) & D(\mathbf{x},\mathbf{y}) \end{pmatrix} \begin{pmatrix} U(\mathbf{x}|\mathbf{s}) \\ V(\mathbf{x}|\mathbf{s}) \end{pmatrix} = \begin{pmatrix} G_{ext}(\mathbf{y},\mathbf{s}) \\ \frac{\partial G_{ext}(\mathbf{y},\mathbf{s})}{\partial n(\mathbf{y})} \end{pmatrix} \tag{4}$$

for surface points $\mathbf{y} \in \mathcal{S}$ and

$$U_{sca}(\mathbf{r}|\mathbf{s}) = \int_{\mathcal{S}} dS(\mathbf{x}) \begin{pmatrix} \partial G_{ext}(\mathbf{x},\mathbf{r})/\partial n(\mathbf{x}), & -G_{ext}(\mathbf{x},\mathbf{r}) \end{pmatrix} \begin{pmatrix} U(\mathbf{x}|\mathbf{s}) \\ V(\mathbf{x}|\mathbf{s}) \end{pmatrix} \tag{5}$$

for exterior points $\mathbf{r} \in \mathcal{E}$. For any exterior source point $\mathbf{s}$, these equations are solvable for $U_{sca}(\mathbf{r}|\mathbf{s})$ at any exterior field point $\mathbf{r}$. In the next section, we concentrate on solving them in the far-field.

2.2 Far-Field Limit

We now pass to the far-field limit. With the origin in the vicinity of the scatterer, we allow $\mathbf{s}$ and $\mathbf{r}$ to recede to distant reaches of $\mathcal{E}$ so that $s, r \gg D$. Then we can expand the Green's function

$$G_{ext}(\mathbf{y},\mathbf{s}) = \frac{\exp\{ik_{ext}|\mathbf{y}-\mathbf{s}|\}}{4\pi|\mathbf{y}-\mathbf{s}|} \tag{6}$$

and its normal derivative at a surface point $\mathbf{y}$ to first order in (D/s) to obtain

$$G_{ext}(\mathbf{y},\mathbf{s}) \approx \frac{\exp\{ik_{ext}s\}}{4\pi s} P(\hat{\mathbf{s}},\mathbf{y}) \tag{7a}$$

$$\tfrac{\partial}{\partial n(\mathbf{y})}\, G_{ext}(\mathbf{y},\mathbf{s}) \approx \frac{\exp\{ik_{ext}s\}}{4\pi s} Q(\hat{\mathbf{s}},\mathbf{y}) \tag{7b}$$

where

$$P(\hat{\mathbf{s}},\mathbf{y}) = \exp\{-ik_{ext}\hat{\mathbf{s}}\cdot\mathbf{y}\} \tag{8a}$$

and

$$Q(\hat{\mathbf{s}},\mathbf{y}) = -ik_{ext}\, \hat{\mathbf{n}}(\mathbf{y})\cdot\hat{\mathbf{s}}\, P(\hat{\mathbf{s}},\mathbf{y})\,. \tag{8b}$$

Physically, this just means that the spherical incident field is approximately a plane wave throughout the scattering region. The phase of this plane wave is $\mathbf{k}_{ext}\cdot\mathbf{y}$, where the source direction is $\hat{\mathbf{s}} = -\hat{\mathbf{k}}_{ext}$. This estimate is valid only in the source terms on the right-hand side of Eq. (4). Similarly, for a distant receiver and a surface point $\mathbf{x}$, the estimates

$$G_{ext}(\mathbf{x},\mathbf{r}) \approx \frac{\exp\{ik_{ext}r\}}{4\pi r} P(\hat{\mathbf{r}},\mathbf{x}) \tag{9a}$$

and

$$\frac{\partial}{\partial n(\mathbf{x})} G_{ext}(\mathbf{x},\mathbf{r}) \approx \frac{\exp\{ik_{ext}r\}}{4\pi r} Q(\hat{\mathbf{r}},\mathbf{x}) \tag{9b}$$

apply in the scattered field integral, Eq. (5). As a result, in the far-field regime, the scattered field has the asymptotic form [7, 8]

$$F(\hat{\mathbf{r}}|\mathbf{k}_{ext})\frac{\exp\{ik_{ext}r\}}{4\pi r} \ . \tag{10}$$

This is an outgoing spherical wave modulated by a complex amplitude $F(\hat{\mathbf{r}}|\mathbf{k}_{ext})$ — the scattering amplitude or "far-field radiation pattern" in the direction $\hat{\mathbf{r}}$ that is produced by incident plane wave radiation with unit amplitude and wavevector $\mathbf{k}_{ext}$. Figure 4 shows that $\mathbf{k}_{ext} = k_{ext}\hat{\mathbf{k}}_{ext} = (\omega/c_{ext})(-\hat{\mathbf{s}})$. It follows that $F(\hat{\mathbf{r}}|\mathbf{k}_{ext})$ is the amplitude for scattering at frequency ω from direction $-\hat{\mathbf{s}}$ into direction $\hat{\mathbf{r}}$. Because the frequency is fixed, we are free to leave the k_{ext} dependence implicit and write the scattering amplitude as simply $F(\hat{\mathbf{r}}|-\hat{\mathbf{s}})$. This single-frequency far-field scattering amplitude is what we will model.

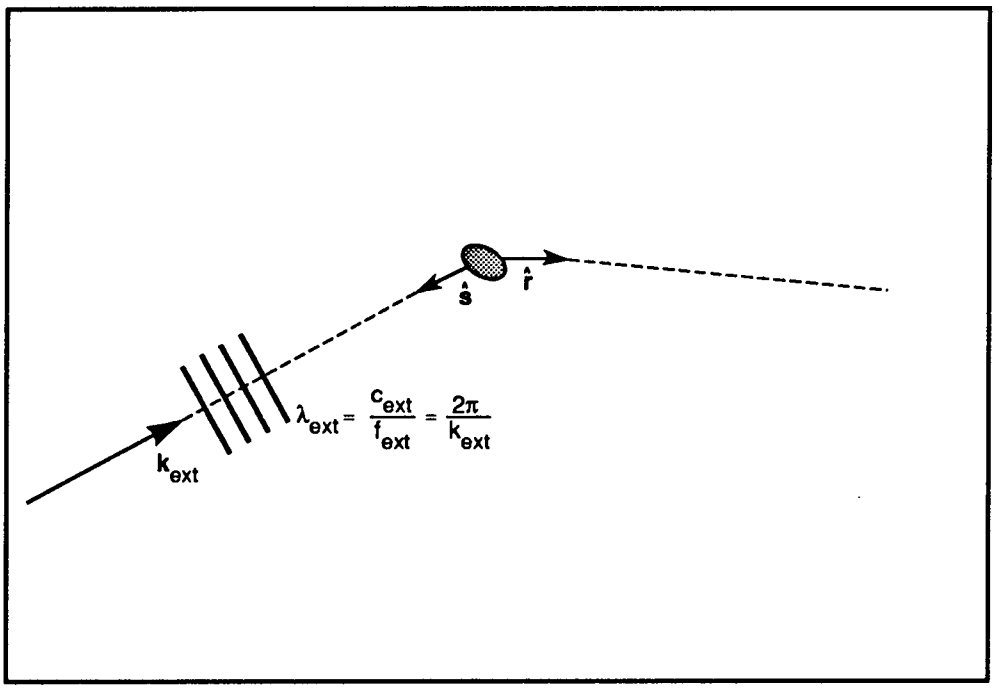

Fig. 4 – Sketch of the quantities involved in the scattering function

In a similar way, $U(\mathbf{y}|\mathbf{s})$ and $V(\mathbf{y}|\mathbf{s})$ have the far-field asymptotic forms

$$U(\mathbf{y}|\hat{\mathbf{s}})\frac{\exp\{ik_{ext}s\}}{4\pi s} \tag{11a}$$

and

$$V(\mathbf{y}|\hat{\mathbf{s}})\frac{\exp\{ik_{ext}s\}}{4\pi s} \tag{11b}$$

where $U(\mathbf{y}|\hat{\mathbf{s}})$ and $V(\mathbf{y}|\hat{\mathbf{s}})$ are factors that depend only on the direction of $\mathbf{s}$. In the far-field limit, neglecting spherical spreading factors $\exp\{ik_{ext}r\}/4\pi r$ and $\exp\{ik_{ext}s\}/4\pi s$, our task is first to solve the boundary continuity condition

$$\begin{pmatrix} (\bar{\rho}/\rho_{int})U(\mathbf{y}|\hat{\mathbf{s}}) \\ (\bar{\rho}/\rho_{ext})V(\mathbf{y}|\hat{\mathbf{s}}) \end{pmatrix} + \int_{\mathcal{S}} dS(\mathbf{x}) \begin{pmatrix} -A(\mathbf{x},\mathbf{y}) & B(\mathbf{x},\mathbf{y}) \\ -C(\mathbf{x},\mathbf{y}) & D(\mathbf{x},\mathbf{y}) \end{pmatrix} \begin{pmatrix} U(\mathbf{x}|\hat{\mathbf{s}}) \\ V(\mathbf{x}|\hat{\mathbf{s}}) \end{pmatrix} = \begin{pmatrix} P(\hat{\mathbf{s}},\mathbf{y}) \\ Q(\hat{\mathbf{s}},\mathbf{y}) \end{pmatrix} , \tag{12}$$

obtaining $U(\mathbf{x}|\hat{\mathbf{s}})$ and $V(\mathbf{x}|\hat{\mathbf{s}})$ throughout $\mathbf{x} \in \mathcal{S}$, and then to use these in calculating the scattering amplitude according to

$$F(\hat{\mathbf{r}}|-\hat{\mathbf{s}}) = \frac{1}{4\pi}\int_{\mathcal{S}} dS(\mathbf{x}) \left(Q(\hat{\mathbf{r}},\mathbf{x}), -P(\hat{\mathbf{r}},\mathbf{x})\right) \begin{pmatrix} U(\mathbf{x}|\hat{\mathbf{s}}) \\ V(\mathbf{x}|\hat{\mathbf{s}}) \end{pmatrix} . \tag{13}$$

As usual in scattering work, we are treating the exterior region as if the local value of c_{ext} prevailing near the scatterer actually extended to infinity in all directions. In environments where that approximation is valid, the scattered field is expressed simply and directly in terms of this scattering amplitude. Even when the exterior region is considerably more complex (in a shallow water waveguide, for example) the plane wave scattering amplitude remains a useful theoretical and computational intermediate quantity [9, 10]. The remainder of this section introduces the modification required to accommodate the simple departure from an infinite homogeneous exterior that will be needed for scattering from a near-surface plume — namely, the presence of the air/sea boundary.

2.3 Air-Sea Boundary Condition

We will take the flat air/sea interface $z = 0$ to be a pressure-release boundary. Temporarily shifting the origin up from the center of the plume to the interface, we resolve vectors into components parallel and perpendicular to that boundary, e. g., $\mathbf{x} = \mathbf{x}_{\|} + \mathbf{x}_{\perp}$, and denote the image under reflection by $\tilde{\mathbf{x}} = \mathbf{x}_{\|} - \mathbf{x}_{\perp}$. The pressure relief condition can be implemented at this stage of the problem simply by using the appropriate half-space exterior Green's function instead of Eq. (6). All of the above results remain valid if we simply replace $G_{ext}(\mathbf{x},\mathbf{y})$, $P(\hat{\mathbf{r}},\mathbf{x})$, and $Q(\hat{\mathbf{r}},\mathbf{x})$ by $G_{ext}(\mathbf{x},\mathbf{y}) - G_{ext}(\mathbf{x},\tilde{\mathbf{y}})$, $P(\hat{\mathbf{r}},\mathbf{x}) - P(\hat{\mathbf{r}},\tilde{\mathbf{x}})$, and $Q(\hat{\mathbf{r}},\mathbf{x}) - Q(\hat{\mathbf{r}},\tilde{\mathbf{x}})$. Explicitly, this means using

$$G_{ext}(\mathbf{x},\mathbf{y}) = \frac{\exp\left(ik_{ext}|\mathbf{x}-\mathbf{y}|\right)}{4\pi|\mathbf{x}-\mathbf{y}|} - \frac{\exp\left(ik_{ext}|\mathbf{x}-\tilde{\mathbf{y}}|\right)}{4\pi|\mathbf{x}-\tilde{\mathbf{y}}|} , \tag{14}$$

$$P(\hat{\mathbf{r}},\mathbf{x}) = -2i\sin\left(k_{ext}\,\mathbf{x}\cdot\hat{\mathbf{r}}_{\perp}\right)\exp\{-ik_{ext}\,\mathbf{x}\cdot\hat{\mathbf{r}}_{\|}\} , \tag{15a}$$

and

$$Q(\hat{\mathbf{r}},\mathbf{x}) = -2k_{ext}\left(\sin\left(k_{ext}\,\mathbf{x}\cdot\hat{\mathbf{r}}_{\perp}\right)\hat{\mathbf{r}}_{\|} + i\cos\left(k_{ext}\,\mathbf{x}\cdot\hat{\mathbf{r}}_{\perp}\right)\hat{\mathbf{r}}_{\perp}\right)\cdot\hat{\mathbf{n}}(\mathbf{x})\exp\{-ik_{ext}\,\mathbf{x}\cdot\hat{\mathbf{r}}_{\|}\} . \tag{15b}$$

This is sufficient if the interface lies entirely in the exterior, i.e., if the plume does not break the surface. We will assume so and proceed to treat plumes of that type.

3. GREEN'S FUNCTIONS

In this section, we develop expressions for the Green's functions and their gradients that are needed in the A, B, C, and D kernels of Eq. (2). For this, we define the relative vector $\mathbf{u} = \mathbf{x} - \mathbf{y}$ and exploit the fundamental gradients of its length u; thus

$$\frac{\partial}{\partial \mathbf{x}} u = \hat{\mathbf{u}} , \tag{16a}$$

$$\frac{\partial}{\partial \mathbf{y}} u = -\hat{\mathbf{u}} , \tag{16b}$$

and

$$\frac{\partial}{\partial \mathbf{y}} \frac{\partial}{\partial \mathbf{x}} u = -\mathbf{\Phi}/u , \tag{16c}$$

where $\hat{\mathbf{u}} = \mathbf{u}/u$ is the direction of $\mathbf{u}$, $\mathbf{\Pi} = \hat{\mathbf{u}}\hat{\mathbf{u}}$ is the projection operator in that direction, and $\mathbf{\Phi} = \mathbf{1} - \mathbf{\Pi}$ is the complementary projector onto the plane orthogonal to $\mathbf{u}$.

3.1 Exterior

Differentiation of Eq. (14) produces the following expressions for the half-space exterior Green's function and its spatial gradients:

$$G_{ext}(\mathbf{x},\mathbf{y}) = \frac{k_{ext}}{4\pi}\left(\frac{1}{w}e^{iw} - \frac{1}{v}e^{iv}\right) , \tag{17a}$$

$$\frac{\partial}{\partial \mathbf{x}} G_{ext}(\mathbf{x},\mathbf{y}) = \frac{k_{ext}^2}{4\pi}\left(\frac{q(w)}{w^2}e^{iw}\hat{\mathbf{u}} - \frac{q(v)}{v^2}e^{iv}\hat{\mathbf{u}}_{\downarrow}\right) , \tag{17b}$$

$$\frac{\partial}{\partial \mathbf{y}} G_{ext}(\mathbf{x},\mathbf{y}) = -\frac{k_{ext}^2}{4\pi}\left(\frac{q(w)}{w^2}e^{iw}\hat{\mathbf{u}} - \frac{q(v)}{v^2}e^{iv}\hat{\mathbf{u}}_{\uparrow}\right) , \tag{17c}$$

and

$$\frac{\partial}{\partial \mathbf{y}} \frac{\partial}{\partial \mathbf{x}} G_{ext}(\mathbf{x},\mathbf{y}) = \frac{k_{ext}^3}{4\pi}\left(\frac{p(w)\hat{\mathbf{u}}\hat{\mathbf{u}} - q(w)\mathbf{1}}{w^3}e^{iw} - \frac{p(v)\hat{\mathbf{u}}_{\uparrow}\hat{\mathbf{u}}_{\downarrow} - q(v)\tilde{\mathbf{1}}}{v^3}e^{iv}\right) \tag{17d}$$

in terms of the phase factors

$$w = k_{ext}|\mathbf{x} - \mathbf{y}|$$
$$v = k_{ext}|\mathbf{x} - \tilde{\mathbf{y}}| ,$$

the complex functions

$$q(\chi) = i\chi - 1$$
$$p(\chi) = \chi^2 + 3q(\chi) ,$$

and the unit vectors

$$\hat{\mathbf{u}}_{\downarrow} = \frac{\mathbf{x} - \tilde{\mathbf{y}}}{|\mathbf{x} - \tilde{\mathbf{y}}|}$$
$$\hat{\mathbf{u}}_{\uparrow} = \frac{\tilde{\mathbf{x}} - \mathbf{y}}{|\tilde{\mathbf{x}} - \mathbf{y}|}$$

(whose vertical components point downward and upward as indicated by the arrow subscripts) as well as the identity and reflection operators $\mathbf{1}$ and $\tilde{\mathbf{1}} = \mathbf{1} - 2\hat{\mathbf{e}}_z\hat{\mathbf{e}}_z$ for which $\mathbf{1}\mathbf{x} = \mathbf{x}$ and $\tilde{\mathbf{1}}\mathbf{x} = \tilde{\mathbf{x}}$.

3.2 Interior

Assuming small interior sound speed gradients in the sense that $|\Delta\lambda/\lambda| \ll 1$; i.e.,

$$\varepsilon_{WKB} \equiv \left| k_{int}^{-2}(\mathbf{r}) \frac{\partial k_{int}(\mathbf{r})}{\partial \mathbf{r}} \right| \ll 1 \ , \tag{18}$$

we may approximate the interior Green's function by the WKB-type form

$$G_{int}(\mathbf{x},\mathbf{y}) = \frac{e^{i\varphi(\mathbf{x},\mathbf{y})}}{4\pi u} \ . \tag{19a}$$

The required gradients are then

$$\tfrac{\partial}{\partial \mathbf{x}}\, G_{int} = G_{int} \left\{ i \frac{\partial \varphi}{\partial \mathbf{x}} - \frac{\hat{\mathbf{u}}}{u} \right\} \tag{19b}$$

$$\tfrac{\partial}{\partial \mathbf{y}}\, G_{int} = G_{int} \left\{ i \frac{\partial \varphi}{\partial \mathbf{y}} + \frac{\hat{\mathbf{u}}}{u} \right\} \tag{19c}$$

$$\tfrac{\partial}{\partial \mathbf{y}}\ \tfrac{\partial}{\partial \mathbf{x}}\, G_{int} = G_{int} \left\{ \frac{1}{u^2}(\mathbf{\Phi} - 2\mathbf{\Pi}) - \frac{\partial \varphi}{\partial \mathbf{y}} \frac{\partial \varphi}{\partial \mathbf{x}} + i \left(\frac{\hat{\mathbf{u}}}{u} \frac{\partial \varphi}{\partial \mathbf{x}} - \frac{\partial \varphi}{\partial \mathbf{y}} \frac{\hat{\mathbf{u}}}{u} + \frac{\partial^2 \varphi}{\partial \mathbf{y} \partial \mathbf{x}} \right) \right\} \tag{19d}$$

in terms of the spatial derivatives of the phase term φ. With the line segment from $\mathbf{y}$ to $\mathbf{x}$ parameterized by

$$\mathbf{z}(\xi) = \mathbf{y} + \xi \hat{\mathbf{u}} \ \cdots \ 0 \le \xi \le u \ , \tag{20}$$

this phase can be expressed as the line integral

$$\varphi(\mathbf{x},\mathbf{y}) = \int_0^u d\xi \, k_{int}(\mathbf{z}(\xi)) \tag{21}$$

from $\mathbf{z}(0) = \mathbf{y}$ to $\mathbf{z}(u) = \mathbf{x}$. Its first-order gradients are consequently

$$\frac{\partial \varphi}{\partial \mathbf{x}} = \mathbf{f}\cdot\mathbf{\Phi} + k_{int}(\mathbf{x})\hat{\mathbf{u}} \tag{22a}$$

$$\frac{\partial \varphi}{\partial \mathbf{y}} = \mathbf{e} - \frac{\partial \varphi}{\partial \mathbf{x}} \tag{22b}$$

and, with second-order spatial derivatives of the wavenumber neglected, the second-order gradient is

$$\frac{\partial^2 \varphi}{\partial \mathbf{y} \partial \mathbf{x}} \approx \frac{1}{u} \left(\hat{\mathbf{u}}\{\mathbf{f}\cdot\mathbf{\Phi}\} + \{\mathbf{f}\cdot\mathbf{\Phi}\}\hat{\mathbf{u}} + (\mathbf{f}\cdot\hat{\mathbf{u}} - k_{int}(\mathbf{x}))\mathbf{\Phi} \right) - \hat{\mathbf{u}}\mathbf{g}(\mathbf{x}) + 2(\mathbf{g}(\mathbf{x})\cdot\hat{\mathbf{u}})\mathbf{\Pi} \tag{22c}$$

in terms of the interior wavenumber gradient

$$\mathbf{g}(\mathbf{r}) = \frac{\partial k_{int}(\mathbf{r})}{\partial \mathbf{r}} \tag{23}$$

and its integrals

$$\mathbf{e} = \int_0^u d\xi \, \mathbf{g}(\mathbf{z}(\xi)) \tag{24a}$$

and

$$\mathbf{f} = \frac{1}{u} \int_0^u d\xi \, \xi \, \mathbf{g}(\mathbf{z}(\xi)) \ . \tag{24b}$$

Thus, the phase and its gradients can be computed by numerical quadrature and then used to compute the interior Green's function and its gradients.

With these explicit forms for the two Green's functions, we now have all of the components essential to the analytic specification of the scattering problem; namely, the kernels A, B, C, and D in the continuity condition (Eq. (12)) and the P and Q functions that appear in Eq. (12) as inhomogeneities and also as quadrature weights in the scattering amplitude equation, Eq. (13). The remaining task is to devise a means of getting a numerical solution.

4. WIREFRAME SOLUTION

4.1 Continuity Condition

To solve the continuity condition (Eq. (12)) numerically, we first 'tile' the plume surface. This means fitting $\mathcal{S}$ with a "wireframe" of N plane facets (the tiles) that are approximately uniform equilateral triangles (Fig. 5, for example) with centers at the points $\mathbf{x}_n$. We then approximate the surface integral as a sum over the wireframe, thus converting Eq. (12) into the algebraic expression

$$\begin{pmatrix} (\bar{\rho}/\rho_{int})\mathsf{I} - \mathsf{A} & \mathsf{B} \\ -\mathsf{C} & (\bar{\rho}/\rho_{ext})\mathsf{I} + \mathsf{D} \end{pmatrix} \begin{pmatrix} \mathsf{U}(\hat{\mathbf{s}}) \\ \mathsf{V}(\hat{\mathbf{s}}) \end{pmatrix} = \begin{pmatrix} \mathsf{P}(\hat{\mathbf{s}}) \\ \mathsf{Q}(\hat{\mathbf{s}}) \end{pmatrix} . \tag{25}$$

Here I is the $N \times N$ identity matrix; $\mathsf{U}(\hat{\mathbf{s}}), \mathsf{V}(\hat{\mathbf{s}})$ and $\mathsf{P}(\hat{\mathbf{s}}), \mathsf{Q}(\hat{\mathbf{s}})$ are the $N \times 1$ column matrices

$$U_n(\hat{\mathbf{s}}) = U(\mathbf{x}_n|\hat{\mathbf{s}}) , \tag{26a}$$

$$V_n(\hat{\mathbf{s}}) = V(\mathbf{x}_n|\hat{\mathbf{s}}) , \tag{26b}$$

and

$$P_n(\hat{\mathbf{s}}) = P(\hat{\mathbf{s}}|\mathbf{x}_n) , \tag{26c}$$

$$Q_n(\hat{\mathbf{s}}) = Q(\hat{\mathbf{s}}|\mathbf{x}_n) ; \tag{26d}$$

and $\mathsf{A}, \mathsf{B}, \mathsf{C}$, and D are $N \times N$ matrices with off-diagonal elements

$$A_{mn} = A(\mathbf{x}_n, \mathbf{x}_m)\, S_m , \tag{27a}$$

$$B_{mn} = B(\mathbf{x}_n, \mathbf{x}_m)\, S_m , \tag{27b}$$

$$C_{mn} = C(\mathbf{x}_n, \mathbf{x}_m)\, S_m , \tag{27c}$$

and

$$D_{mn} = D(\mathbf{x}_n, \mathbf{x}_m)\, S_m, \tag{27d}$$

where S_m is the area of the patch of the plume's surface subtended by the mth tile (see Appendix B). These $m \neq n$ matrix elements can be calculated directly from the definitions of Eq. (2) using the areas and normals of the surface patches and the Green's function gradients that were developed in the preceding section. The $m = n$ elements require separate consideration.

4.2 Diagonal Matrix Elements

The diagonal elements are complicated by the weak singularity of some of the kernels in Eq. (12), i.e., by their divergence as $\mathbf{x} \to \mathbf{y}$ [8]. Expressions for them are derived in Appendix

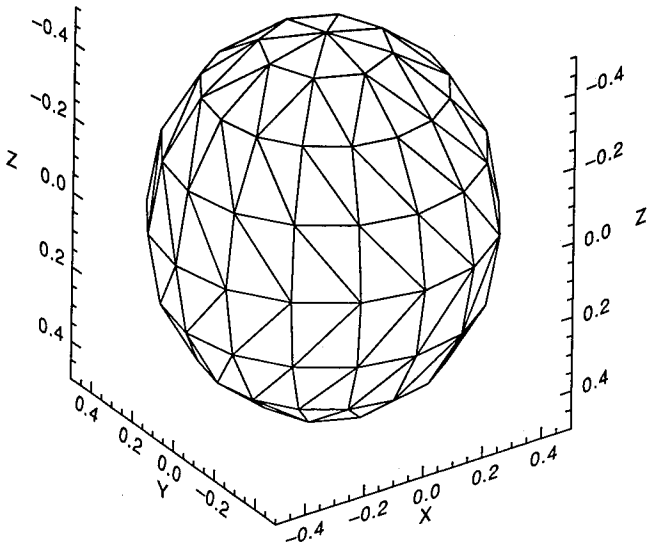

Fig. 5 – A spherical wireframe with 192 tiles

C and are summarized below. In these, $\hat{\mathbf{n}}_m$ and z_m are the mth surface patch's normal vector and center depth, $k_{int,m} = k_{int}(\mathbf{x}_m)$ is the interior wavenumber at the patch center, W_m is the integral $\int dS(\mathbf{x})\, 1/|\mathbf{x} - \mathbf{x}_m|$ over the mth patch (Appendix B) and, as before, $q(\xi) = i\xi - 1$. Also appearing: $\mu_m = 2z_m k_{ext}$, which measures the depth of the patch in units of the exterior wavelength; $\nu_m = \hat{\mathbf{e}}_z \cdot \hat{\mathbf{n}}_m$, which represents the vertical tilt of the normal; and $g_m = \hat{\mathbf{n}}_m \cdot \mathbf{g}(\mathbf{x}_m)$, the normal component of the wavenumber gradient.

The diagonal matrix elements are

$$A_{mm} = \left\{ -\frac{i}{2}\frac{\rho_{ext}}{\rho_{int}} g_m - \left(\frac{k_{ext}}{\mu_m}\right)^2 q(\mu_m) e^{i\mu_m} \nu_m \right\} \left(\frac{S_m}{4\pi}\right) \tag{28a}$$

$$B_{mm} = -\left\{ i(k_{int,m} - k_{ext}) + \left(\frac{k_{ext}}{\mu_m}\right) e^{i\mu_m} \right\} \left(\frac{S_m}{4\pi}\right) \tag{28b}$$

$$C_{mm} = -\frac{1}{2}(k_{int,m}^2 - k_{ext}^2)\left(\frac{W_m}{4\pi}\right) - \frac{i}{3}(k_{int,m}^3 - k_{ext}^3)\left(\frac{S_m}{4\pi}\right) + \left(\frac{k_{ext}}{\mu_m}\right)^3 \left[(\mu_m \nu_m)^2 + q(\mu_m)(1 + \nu_m^2)\right] \left(\frac{S_m}{4\pi}\right) \tag{28c}$$

$$D_{mm} = \left\{ +\frac{i}{2}\frac{\rho_{ext}}{\rho_{int}} g_m - \left(\frac{k_{ext}}{\mu_m}\right)^2 q(\mu_m) e^{i\mu_m} \nu_m \right\} \left(\frac{S_m}{4\pi}\right). \tag{28d}$$

The terms containing μ_m embody the surface-image effects. With the matrix elements provided by Eqs. (26) through (28), Eq. (25) can be solved for the values of the source densities U, V on each of the surface tiles.

4.3 Scattering Amplitude Equation

After Eq. (25) is solved for $\mathsf{U}(\hat{\mathbf{s}})$, $\mathsf{V}(\hat{\mathbf{s}})$, all that remains is to apply Eq. (13) in the wireframe approximation; i.e.,

$$F(\hat{\mathbf{r}}|-\hat{\mathbf{s}}) = \sum_{n=1}^{N} S_n\big(Q(\hat{\mathbf{r}},\mathbf{x}_n), -P(\hat{\mathbf{r}},\mathbf{x}_n)\big) \begin{pmatrix} U(\mathbf{x}_n|\hat{\mathbf{s}}) \\ V(\mathbf{x}_n|\hat{\mathbf{s}}) \end{pmatrix}$$
$$= \bar{\mathsf{Q}}^{\top}(\hat{\mathbf{r}})\mathsf{U}(\hat{\mathbf{s}}) - \bar{\mathsf{P}}^{\top}(\hat{\mathbf{r}})\mathsf{V}(\hat{\mathbf{s}}) \tag{29}$$

where $\bar{\mathsf{Q}}$ and $\bar{\mathsf{P}}$ correspond to Q and P with components weighted by the surface area elements ($\bar{Q}_n = S_n Q_n$, $\bar{P}_n = S_n P_n$) and ' $^{\top}$ ' indicates a matrix transpose.

5. MODELING METHODS

This section describes the numerical methods that we have used to implement the scattering formulation described above. We should point out now that the pressure-relief boundary condition that we have taken such pains to impose at the sea surface may be omitted, if desired, by simply omitting the v, μ_m terms in Eqs. (17) and (28) and reverting from Eq. (15) back to the elementary forms in Eq. (8). Indeed, during program development we supported this choice as a diagnostic option. We have retained that option so that the final model, known as BIRPS (Boundary Integral Resonant Plume Scatter), can also be used to model "free-space" scattering.

5.1 Construction of the Wireframe

All the wireframes are initially spherical. Their construction is handled by an algorithm that begins with 2^m tiles ($m > 2$) around the sphere's equator and repeatedly halves this number at higher latitudes to control the tile size, concluding with $2^3 = 8$ tiles around each of the poles. These spherical wireframes are usable without modification in problems dealing with spherical plumes. Figure 5 is the $m = 4$ case with a diameter of 1 m. Actually, wireframes of all shapes are generated in this "unit" form (with a maximum diameter of 1 m) for convenience and are simply scaled up or down as required for various problems.

To produce a wireframe for a nonspherical plume, we first simply project the spherical wireframe's vertices radially. Figure 6 is such a radial projection of the wireframe of Fig. 5 onto an ellipsoidal surface whose x, y, and z dimensions are in the ratio 1:2:3. Since this, too, is a "unit" wireframe, its actual measurements are 1/3 m by 2/3 m by 1 m. Projection always deforms the wireframe to some degree, shrinking some tiles and stretching others. This should be harmless *unless* some of the tiles end up larger than a fraction of the interior wavelength. That kind of distortion can degrade the capability for coherent simulation. When it occurs, we can compensate by further adjusting the wireframe. We do this by a process of simulated annealing applied so as to minimize the normalized variance of the tile edge lengths (Appendix D). This encourages the tiles to become as nearly equilateral and uniform in area as the shape of the plume and the topology of the wireframe will allow. The results of the procedure can be seen in Fig. 7.

The potential for modeling with such a wireframe can be assessed from the relation

$$\frac{N}{f^2} = \frac{a}{\alpha(\beta \bar{c_{int}})^2} \tag{30}$$

(obtained in Appendix E) in which a and $\bar{c_{int}}$ are the plume's area and average interior sound speed and α and β are the constants 0.43 and 0.25, respectively. For a given plume, this expression pertains to a uniform equilateral wireframe with tile sides equal to $\bar{\lambda}_{int}/4$. It can be used to estimate either the minimum N required for a particular f or the maximum f at which a given N is feasible. We will use it for both purposes and will refer to the result as the "marginal tiling estimate" for either N or f according to context.

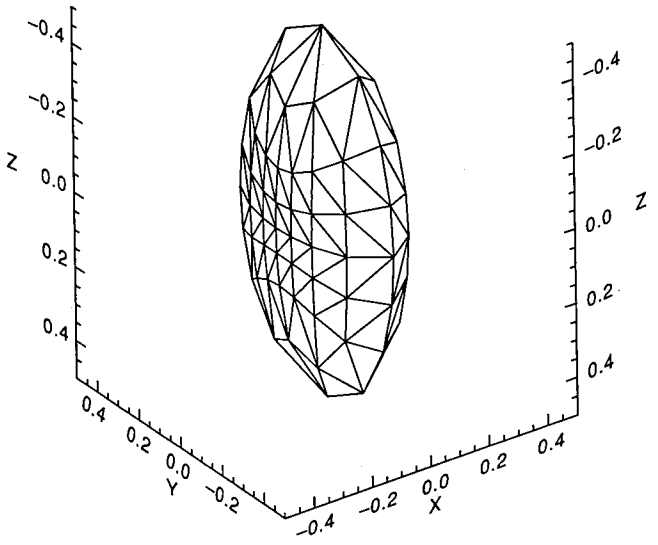

Fig. 6 – Spherical wireframe of Fig. 5 projected onto an ellipsoidal plume shape

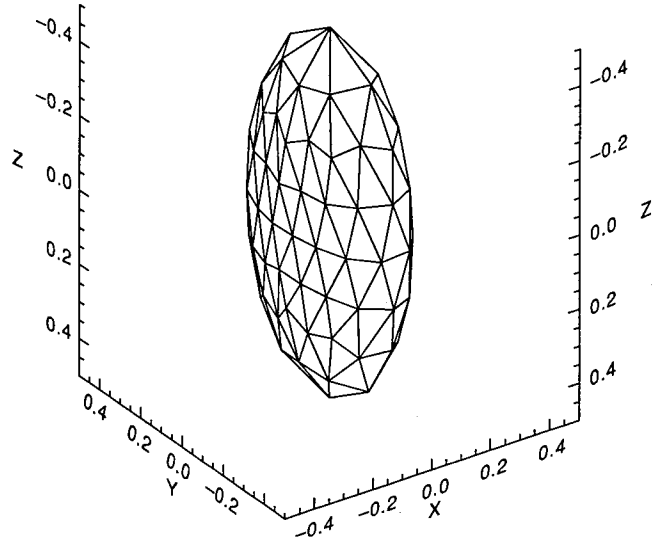

Fig. 7 – Ellipsoidal wireframe of Fig. 6 after annealing

We note as an aside that, although the above tiling scheme worked flawlessly, it is admittedly somewhat lacking in flexibility in that it provides no intermediate possibilities between $N = 16$ tiles for $m = 3$ and $N = 192$ for $m = 4$. While the latter proved entirely satisfactory here, it does represent a degree of numerical "overkill" that is undesirable for two reasons. First, there is the practical matter of computer run time. This increases roughly as N^2, so that using an $m = 4$ wireframe, for example, when the marginal tiling estimate is only 60 means unnecessarily prolonging the execution by a factor of $(192/60)^2 \approx 10$. Secondly, a tiling method that allowed any integral N, rather than just 16 or 192, would open the way to using a method like Richardson's deferred approach to the limit [11] to estimate the values of integrals in the $N \to \infty$ limit. This

could provide increased accuracy for less effort. In the end, it proved prohibitively difficult to devise such a scheme that achieved the desired flexibility while covering the sphere with tiles of controlled size and shape.

5.2 Numerical Computation of the Scattering Amplitude

Equation (25) is a $2N$-dimensional linear problem of the form $\mathsf{M}\mathsf{x} = \mathsf{b}$ and could be solved by a variety of standard methods. We chose the LU decomposition method with iterated improvement — a complex version of the implementation in *Numerical Recipes* [11]. For the modeling, we allow a discrete set of sources, i.e., incident multipath directions $\{\hat{\mathbf{s}}_\sigma;\ \sigma = 1, \cdots, N_{src}\}$, each corresponding to a linear problem

$$\mathsf{M}\mathsf{x}_\sigma = \mathsf{b}_\sigma\ , \tag{31}$$

where

$$\mathsf{x}_\sigma = \begin{pmatrix} \mathsf{U}(\hat{\mathbf{s}}_\sigma) \\ \mathsf{V}(\hat{\mathbf{s}}_\sigma) \end{pmatrix},\ \mathsf{b}_\sigma = \begin{pmatrix} \mathsf{P}(\hat{\mathbf{s}}_\sigma) \\ \mathsf{Q}(\hat{\mathbf{s}}_\sigma) \end{pmatrix}. \tag{32}$$

For a discrete set of outgoing directions $\{\hat{\mathbf{r}}_\rho;\ \rho = 1, \cdots, N_{rec}\}$, Eq. (29) amounts to

$$F_{\rho\sigma} = \mathsf{c}_\rho^\top \mathsf{x}_\sigma \tag{33}$$

where $F_{\rho\sigma} = F(\hat{\mathbf{r}}_\rho | -\hat{\mathbf{s}}_\sigma)$ and

$$\mathsf{c}_\rho = \begin{pmatrix} \bar{\mathsf{Q}}(\hat{\mathbf{r}}_\rho) \\ -\bar{\mathsf{P}}(\hat{\mathbf{r}}_\rho) \end{pmatrix}. \tag{34}$$

When there are $N_{src} > 1$ coherent arrivals, the overall scattering amplitude has the form

$$F_\rho = \sum_{\sigma=1}^{N_{src}} \alpha_\sigma F_{\rho\sigma} \tag{35}$$

with the relative amplitudes and phases of the multipath signals specified by the complex α_σ coefficients.

Since the whole procedure is analytically equivalent to

$$F_\rho = \mathsf{c}_\rho^\top \mathsf{M}^{-1} \left(\sum_{\sigma=1}^{N_{src}} \alpha_\sigma \mathsf{b}_\sigma \right),$$

numerical difficulties can be expected if M becomes ill-conditioned. We encountered this problem (and were forced to switch from LU to singular value decomposition as a remedy) only for environmental parameter values far outside the physical range for this application — interior sound speeds of 50 m/s for instance. Realistic model plumes did not resonate with a high enough Q-factor to cause the problem. Instead, the main problem for our approach is that $2N$ may be quite large. This requires plenty of RAM or a virtual memory system. Fortunately, current computers are adequate for most practical cases. The details of this point are discussed in Appendix E.

BIRPS is implemented in standard FORTRAN 77 and follows the pseudocode outline below. Steps (a) through (c) define the problem analytically and produce a discrete representation of it. Step (d) performs the LU decomposition. When $N_{src} > 1$, loops (e) and (l) scatter the multipath arrivals coherently.

```
(a)     select the shape of S and construct the wireframe
(b)     set the properties of E, I
(c)     compute M
(d)     LU-decompose M
(e)     for σ from 1 to N_src
(f)         compute b_σ
(g)         compute x_σ by LU back-substitution
(h)         apply iterated improvement to Mx_σ − b_σ = 0
        next σ
(i)     for ρ from 1 to N_rec
(j)         initialize:  F_ρ = 0
(k)         compute c_ρ
(l)         for σ from 1 to N_src
(m)             compute F_ρσ by Eq. (33)
(n)             accumulate:  F_ρ = F_ρ + α_σ * F_ρσ
            next σ
        next ρ
```

The plume shape is specified in step (a) by a 'unit radius function' subroutine

```
SUBROUTINE urf ( theta, phi, urad, uonv )
```

whose inputs `theta`, `phi` are the polar angles of a point on the plume surface and whose outputs `urad`, `uonv` are the radius and unit outward normal vector at that point. An interior sound speed profile is specified in terms of the slowness c^{-1} by a real-valued function `svp` whose entry points are the slowness itself,

```
ENTRY slow (xi),
```

and its three spatial gradient components,

```
ENTRY gam x (xi),
ENTRY gam y (xi), and
ENTRY gam z (xi).
```

The input argument `xi` is a distance which specifies the physical location in terms of a reference point and direction which are communicated in a `COMMON` block. The distance, reference point, and direction correspond to ξ, $\mathbf{y}$, and $\hat{\mathbf{u}}$, respectively, in Eq. (20), and the functions are evaluated at the point $\mathbf{z}(\xi)$.

Once the plume's shape and interior sound speed are specified, the numerical computations closely follow the analysis laid out in preceding sections. In particular, the Green's functions are computed as indicated in Section 3 with the interior wavenumber gradient $\mathbf{g}$, Eq. (23), obtained directly from the components of the slowness gradient, and the integrals $\mathbf{e}$ and $\mathbf{f}$, Eq. (24), computed using Romberg quadrature routines on the components of $\mathbf{g}$. Thus, to implement additional plume shapes and interior sound speeds beyond those used in this report, the user need only supply new versions of `urf` and `svp`.

6. PLUME RESULTS

In the following subsections we simulate plume scattering in a series of situations. Except as noted, all of these situations incorporate the pressure-relief condition at the sea surface and involve a single arrival. We will be computing the scattering amplitude F and plotting it (or rather its modulus, since F is complex) as a function of various parameters in the following figures. F is referred to a unit-amplitude incident plane wave and has the physical dimensions of a length.

The sound speed at any point inside a plume can be related to the air volume fraction through the general expression [2, Section 8.9]

$$c = \left[(\beta\rho_g + (1-\beta)\rho_\ell) \left(\frac{\beta}{\rho_g c_g^2} + \frac{1-\beta}{\rho_\ell c_\ell^2} \right) \right]^{-1/2} \tag{36}$$

which gives the effective sound speed c for a suspension of gas bubbles in a liquid in terms of β, the volume fraction of gas. Expert opinion [12] currently distinguishes three bubble structure categories by air volume fraction, namely "tenuous" ($\beta < 10^{-4}$), "intermediate" ($10^{-4} < \beta < 10^{-2}$), and "dense" ($10^{-2} < \beta$). The names refer to the number density of air bubbles thought to be present. Figure 8 is computed from Eq. (36) for air in water and covers the full "intermediate" range. The following simulations deal with interior sound speeds in the 300–800 m/s range and hence with the class of bubble structures known as intermediate plumes. The same method would also apply to tenuous plumes, without reliance on the approximations usually invoked in that regime [13–15], and to dense plumes, provided they are static and their sound speed gradients are not too large.

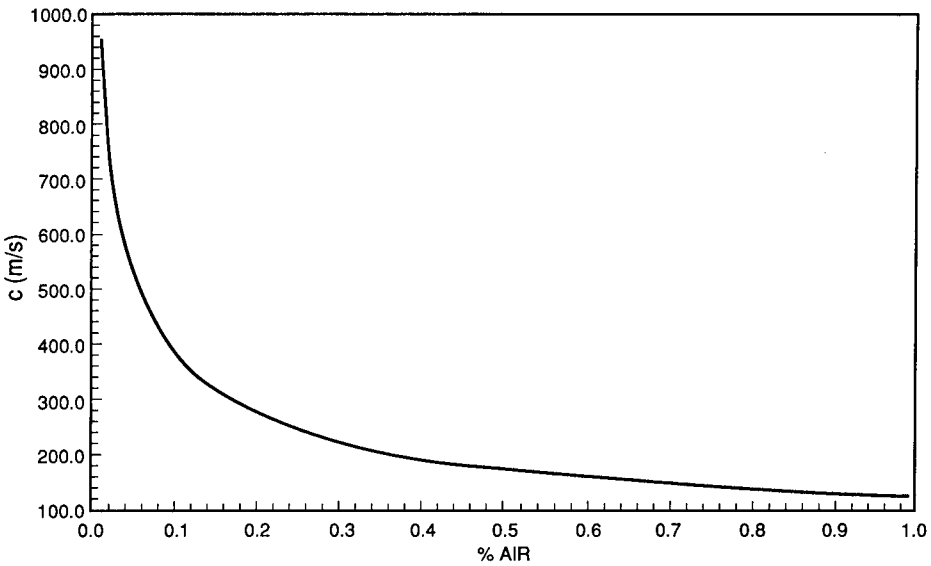

Fig. 8 – Sound speed from Eq. (36) for air suspended in water throughout the "intermediate plume" range, $0.01\% < \beta < 1\%$

6.1 Fundamental Features in Simple Situations

We begin by applying the BIRPS model to simple situations involving a spherical plume with an isovelocity interior. An important objective of this first set of simulations is to validate the model using fairly realistic physical parameters.

6.1.1 Azimuth Dependence

Figure 9 examines two things: the azimuth dependence of the scattering and the number of tiles required for accurate computations. The incident azimuth is 22.5° (i.e., 360° ÷ 16) so

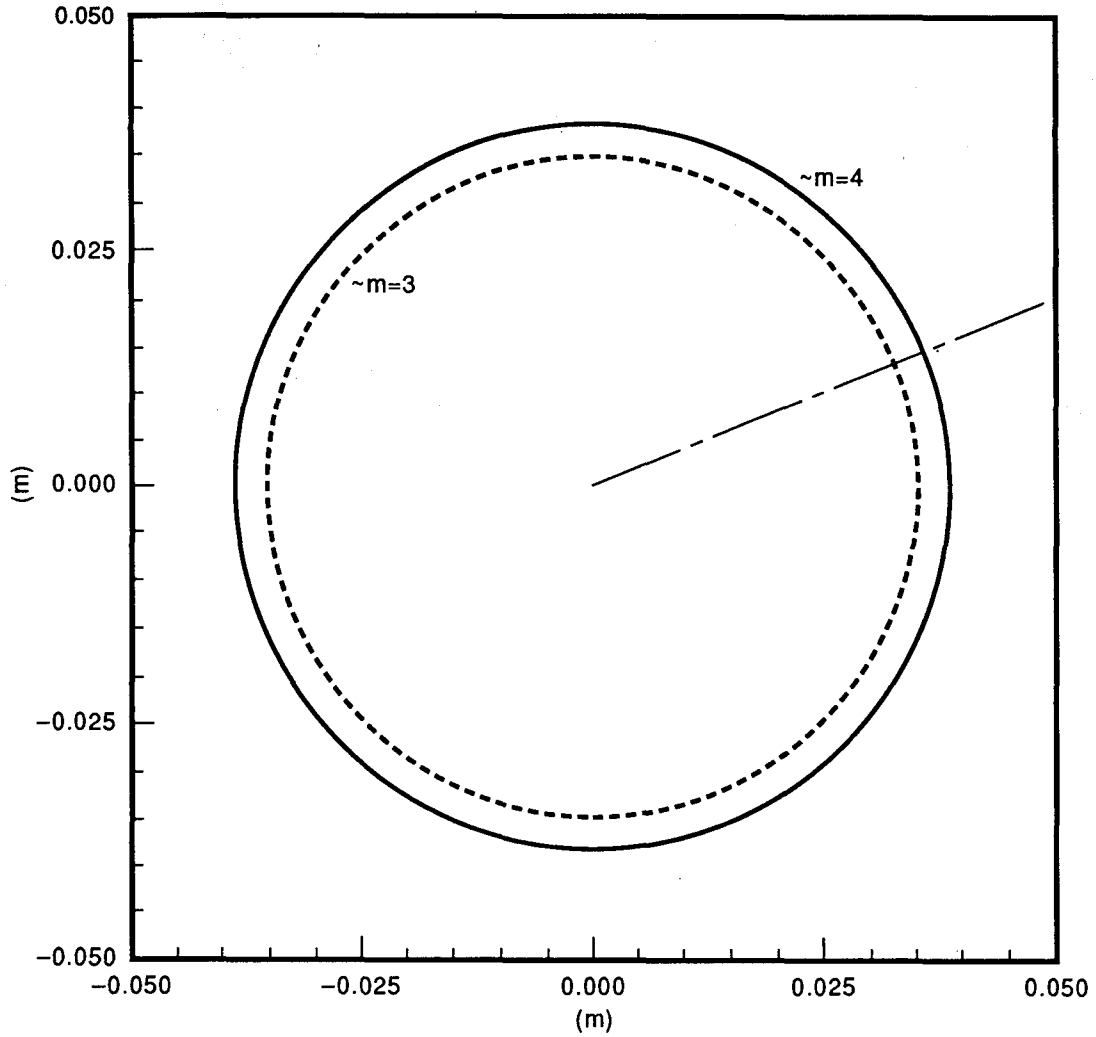

plume shape	overall size	interior svp	number of tiles	annealed wireframe?
sphere	2 m	uniform: 500 m/s	16 – dashed 192 – solid	no

pressure-relief interface?	center depth	receiver direction	source direction	amplitude; phase of source(s)
yes	2 m	azim 0–360° elev 85°	azim 22.5° elev 88°	1.0; 0°

Fig. 9 – Scattering amplitude as a function of azimuth at 125 Hz

that both the $m = 3$ wireframe (with eight equatorial tiles) and the $m = 4$ wireframe (with 16) will be symmetric in azimuth about the source direction. Thus the scattering amplitude as a function of receiver azimuth should inherit that same symmetry. The figure does indeed have the expected symmetry relative to the source direction (the broken straight line). Given the diameter, frequency, and interior sound speed, the marginal tiling estimate (from Eq. (30), see Appendix E) for the minimum number of tiles required is 29. Indeed, the $m = 3$ case (dashed), which has only 16 tiles, is about 10% below the $m = 4$ case (solid) with 192. The scattering amplitude is small (only about 0.04) for these near-grazing source and receiver elevations (5° and 2° below the horizontal, respectively). We will see that this is because these elevations lie in a horizontal notch in the vertical dipole-type beam pattern formed by the plume and its surface image.

6.1.2 Resonance Spectrum

Figure 10 examines the frequency dependence of scattering from the same plume *without* the pressure-release interface. Here the relevant angle is simply the total scattering angle $\vartheta = \arccos(-\hat{\mathbf{s}}\cdot\hat{\mathbf{r}})$, which is taken to be 45°. Results from the present computer model are shown as circles — o for $m = 3$ and • for $m = 4$. The heavy line represents the scattering amplitude as computed by the semi-analytic partial wave method described in Appendix F. The broken lines are the individual $\ell = 0, \cdots, 3$ partial wave contributions — s, p, d, f-wave scattering in atomic physics jargon. The peaks clearly correspond to scattering resonances. The ℓth one lies very close to the frequency $(\ell + 1) \times 125$ Hz that would be anticipated from a "back of the envelope" calculation using $c_{ext} = \infty$ and it can be expected to exhibit the familiar $(\ell + 1)$-lobed structure in the angle ϑ (Appendix F). The Q-factor (i.e., the peak frequency divided by the half-width) increases with frequency: $Q \approx 1, 3, 10$ for $\ell = 0, 1, 2$.

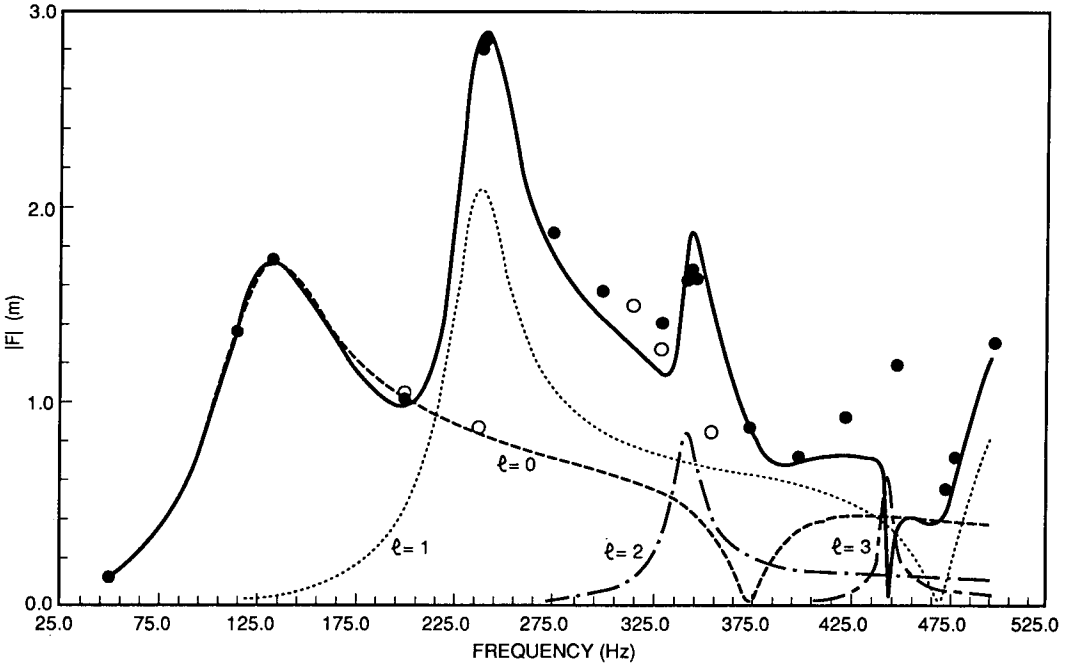

Fig. 10 – Model results for $m = 3$ (o) and $m = 4$ (•). For comparison, computations from Appendix F: $|F|$ (heavy line) and $|F_\ell|$ for $\ell = 0, 1, 2, 3$ (broken lines) as functions of f

A marginal tiling estimate indicates that the $m = 3, 4$ contributions should be accurate up to 92 Hz and 320 Hz, respectively. According to the figure, however, this kind of estimate is overly conservative. The o symbols depart from the heavy line somewhere beyond 195 Hz and the • symbols are adequately close to it through at least 405 Hz. The numerical model exceeds the marginal tiling expectations, failing only with the the onset of the $\ell = 3$ resonance around 445 Hz. This can be understood by considering the radiation pattern for this resonance. It has four lobes in the range $0 < \vartheta < \pi$ while the wireframe (Fig. 5) has only eight "latitude bands" of tiles in that interval. That angular undersampling — only two tiles per angular lobe — appears to cause the breakdown at this point. The method should work at least this well for smaller or faster plumes, since their resonances will be shifted to higher frequencies [16, Chapter VI, Section 2].

For the same situation, Fig. 12 shows the dependence on output elevation in the entire vertical half-plane containing the source direction. The source direction is indicated as usual by the broken line. Back-scattering corresponds to the right half of the figure and forward scattering is on the left. The dashed curves are for frequencies above the resonance peak. All of the curves have a high degree of forward/backward symmetry, evidently because only the symmetric s-wave resonance contributes in this frequency range.

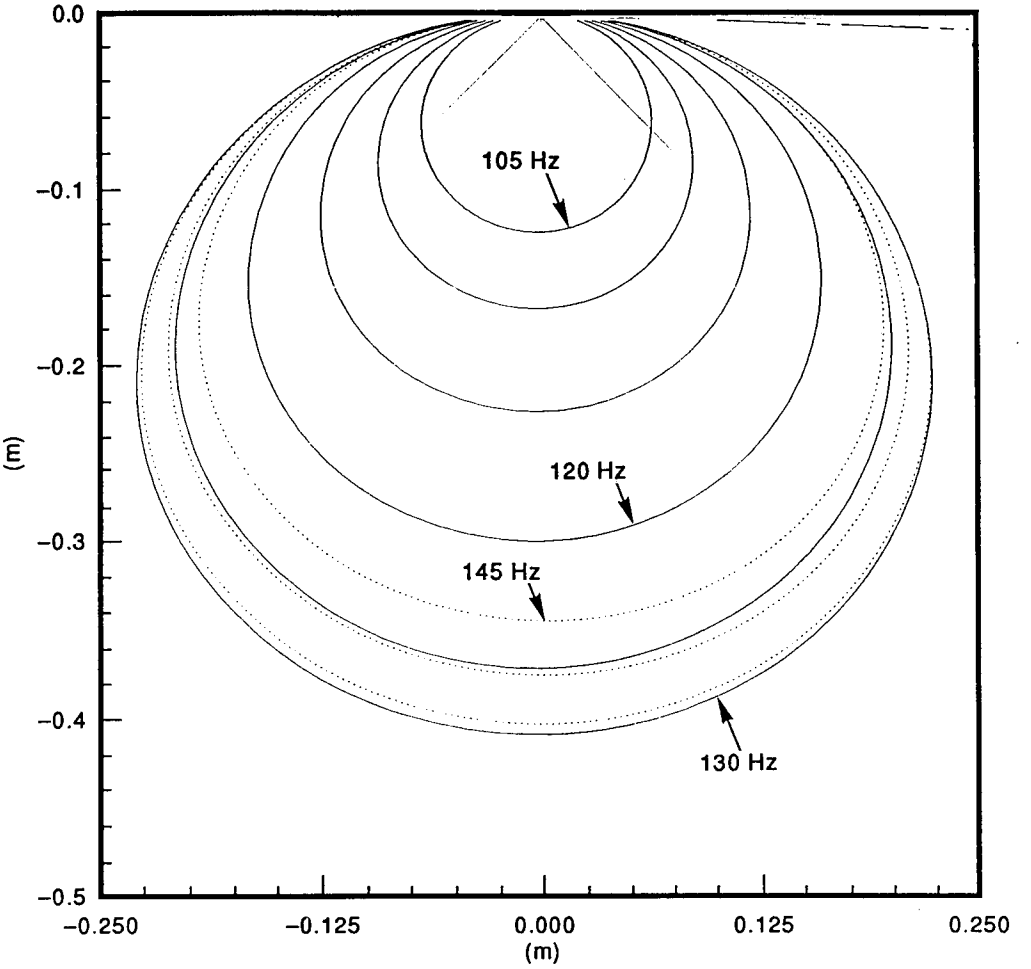

plume shape	overall size	interior svp	number of tiles	annealed wireframe?
sphere	2 m	uniform: 500 m/s	192	no

pressure-relief interface?	center depth	receiver direction	source direction	amplitude; phase of source(s)
yes	2 m	azim 202.5°, 22.5° elev 0–90°	azim 22.5° elev 88°	1.0; 0°

Fig. 12 – Scattering amplitude as a function of elevation, parameterized by frequency. The discrete frequencies are the same as in Fig. 11: 105 Hz to 145 Hz in 5 Hz steps. Solid: $f \leq 130$ Hz, dashed: 130 Hz $< f$.

Figure 13 repeats the computations of Fig. 12 in the vicinity of the p-wave resonance, 205 to 255 Hz. Again, the dashed curves represent frequencies above the resonance peak. Here the forward/backward symmetry is broken by the coherent interplay between the near-resonant p-wave response and the nonresonant s-wave response.

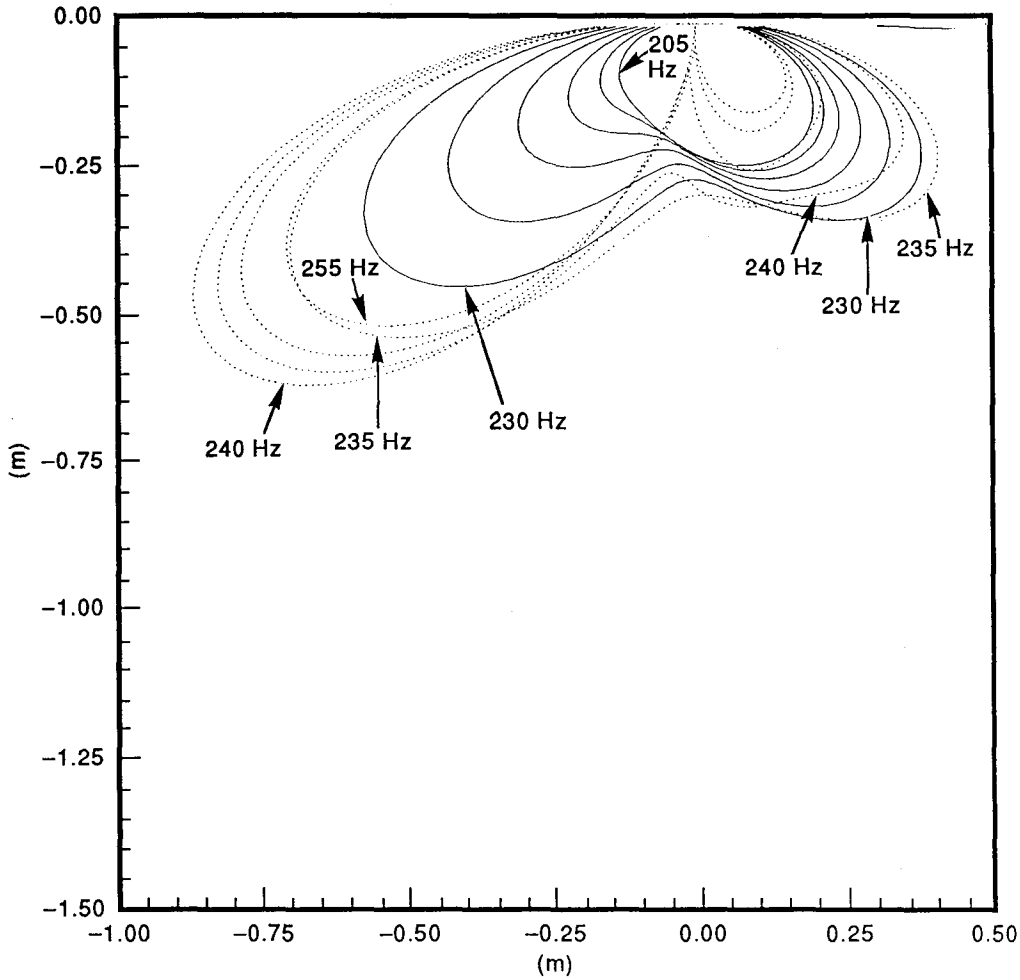

plume shape	overall size	interior svp	number of tiles	annealed wireframe?
sphere	2 m	uniform: 500 m/s	192	no

pressure-relief interface?	center depth	receiver direction	source direction	amplitude; phase of source(s)
yes	2 m	azim 202.5°, 22.5° elev 0–90°	azim 22.5° elev 88°	1.0; 0°

Fig. 13 – Scattering amplitude as a function of elevation, parameterized by frequency. The discrete frequencies run from 205 Hz to 255 Hz in 5 Hz steps. Solid: $f \leq 230$ Hz; dashed: 230 Hz $< f$.

6.1.4 Depth Dependence

For the same plume, Fig. 14 shows the near-vertical scattering response to a near-vertical arrival as a function of the plume's center depth d in the interval 2 m$\leq d \leq$4 m. For comparison, consider what Fig. 14 would look like if, rather than this large resonant plume, we were dealing with a small nonresonant object — a "point target." Then, because both elevations are nearly vertical, the d dependence would be $\sin^2(k_{ext}d)$. This vanishes at the surface and at $d = \lambda_{ext}/2 = 6$ m and is symmetric about its peak at $d = 3$ m. The actual curve in Fig. 14 is similar to that in functional form but has its peak shifted upward by about 0.75 m, presumably due to the plume's finite size and internal structure.

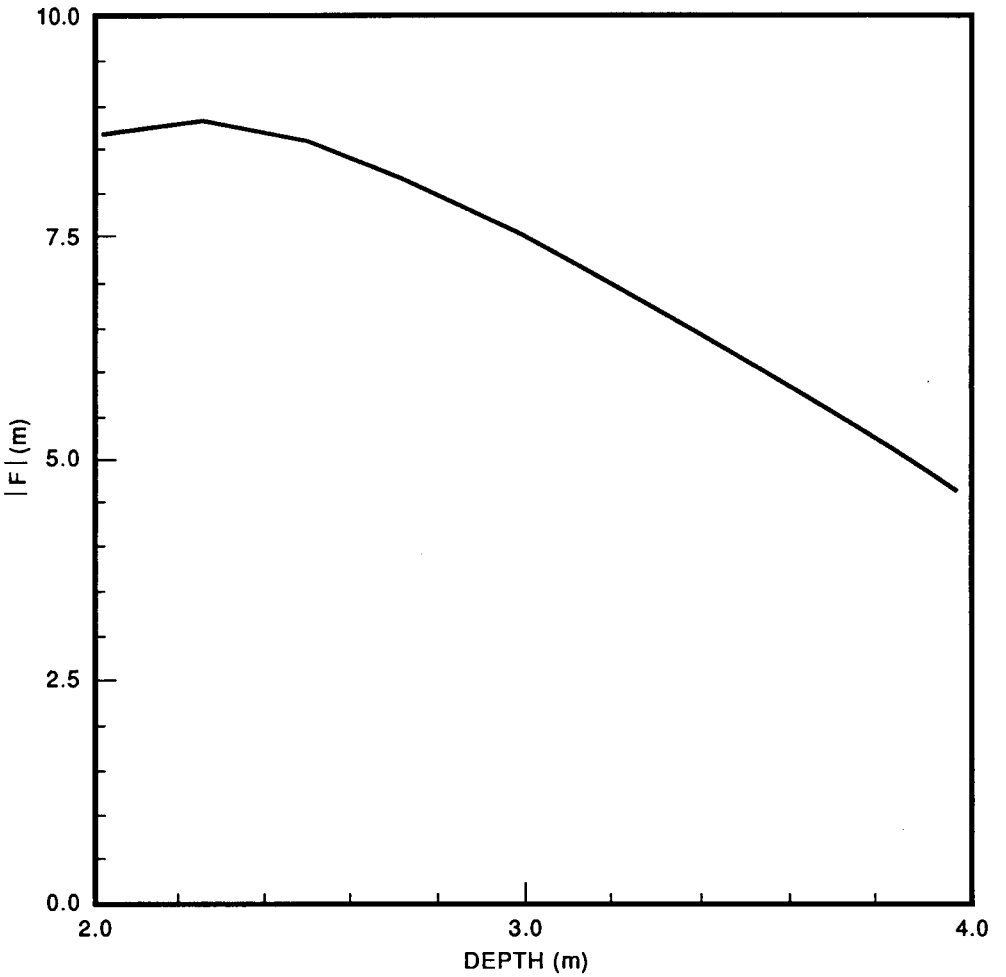

plume shape	overall size	interior svp	number of tiles	annealed wireframe?
sphere	2 m	uniform: 500 m/s	192	no
pressure-relief interface?	**center depth**	**receiver direction**	**source direction**	**amplitude; phase of source(s)**
yes	2–4 m	azim 180° elev 5°	azim 0° elev 5°	1.0; 0°

Fig. 14 – Scattering amplitude for near-vertical elevations as a function of plume center depth at 125 Hz

Next we turn to the near-grazing geometry where, in view of its greater practical importance, we go into more detail. The source and receiver are held at grazing angles of 2.5° and, except as noted, other parameters remain as indicated in the caption to Fig. 14. The object is again to determine the depth dependence of the response in the interval 2 m $\leq d \leq$ 4 m. This was done through BIRPS simulations at 0.25 m intervals. First, as a benchmark case, the plume diameter D was reduced to only 0.5 m. The plume is small relative to the exterior wavelength ($D \ll \lambda_{ext}$) so that, as $d \rightarrow$ 4 m, the response should exhibit the quadratic depth dependence characteristic of a point target in this grazing geometry. The simulations accurately confirm the expected d^2 dependence. For the second simulation series, the 2 m diameter was reinstated and the result was found to be more nearly *linear* in d. Since this plume was resonant at the frequency considered here, it was not clear whether this nonquadratic depth dependence was produced by the resonance or simply by the larger size. The third simulation series addressed that question. Here, the interior sound speed was increased to 1000 m/s, which shifted the lowest resonance well above the operating frequency. The result for this large nonresonant plume was roughly linear for $d \approx$ 2 m but became quadratic for $d >$ 4 m. Figure 15 summarizes all three near-grazing simulations. If it is assumed that the depth dependence follows some power law $|F(d)| \propto d^p$, then the exponent can be assessed from the simulations by plotting $p = |F(d)|'d/|F(d)|$ vs d. This is done in Fig. 15 with the depth derivative estimated by finite differences. The small-plume result is the top curve which, as expected, indicates $p = 2$. The middle curve corresponds to the large nonresonant plume. Its depth dependence starts out as rather linear at $d =$ 2.25 m but becomes effectively quadratic by $d =$ 3.75 m. The bottom curve is the result for the large resonant plume. The behavior is more nearly linear for $d <$ 4 m, although the trend, if extrapolated, is toward quadratic behavior at greater depths. Thus, the deviation from quadratic dependence seems to be in part a result of large D/d. Resonance, however, enhances it, possibly by giving the plume a larger effective diameter. Of course, a finite diameter and a resonant interior do more than just alter the depth dependence of a plume's scattering response. They will both raise the absolute level too, as shown in Fig. 16. The large nonresonant plume scatters at levels 10–12 dB greater than the "point-target" plume and resonance adds another 10–12 dB.

6.1.5 Summary

We find that the low-frequency scattering responses of spherical model intermediate plumes contain multiple weak-to-moderate resonances. The lowest-frequency resonance is an s-wave feature with a uniform azimuth response and an elevation response similar to that of a vertical dipole. The next resonance has a p-wave character so that its azimuth response has forward and backward lobes and its elevation response is quadrupole-like. As the frequency increases through this resonance, the nature of the response shifts from weakly back scattering to strongly forward scattering. Thus, for a receiver in the forward direction and an incident signal with a power spectrum concentrated around the second resonance frequency, the scattered signal would be high-pass filtered. It is also clear that the depth dependence of scattering from realistic intermediate plumes in the first few meters below the surface is very different from what would be expected from a point target — especially at resonance frequencies.

6.2 Effects of Multiple Arrivals

Now we turn to an application in shallow water with several propagation multipaths. For this simulation, we used eight vertical arrivals from a source in a shallow Pekeris environment. Figure 17 summarizes the simulation parameters and the eight multipaths. These multipaths are

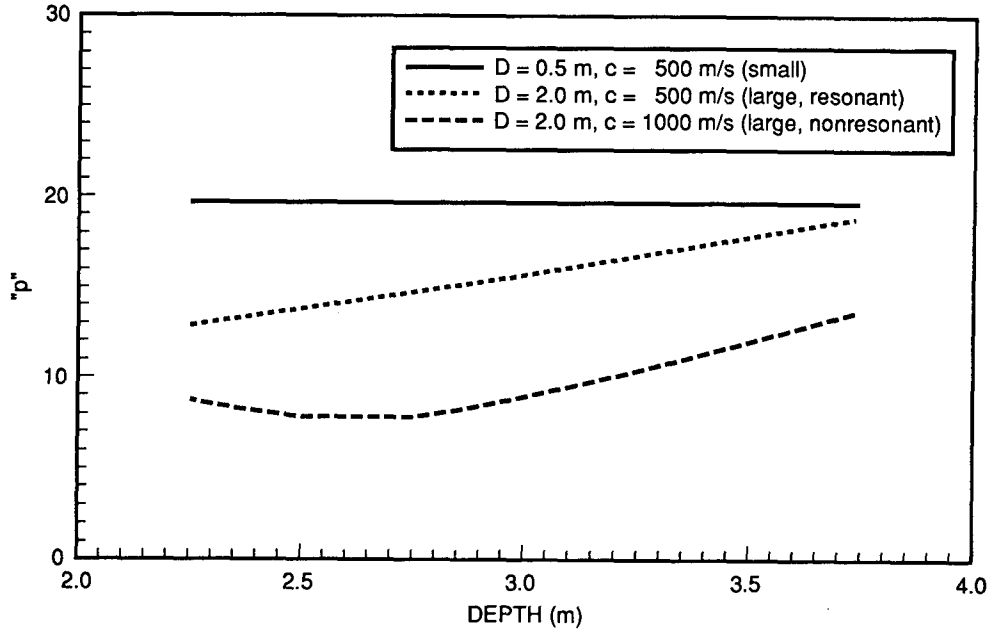

Fig. 15 – Power-law analysis of the depth dependence of the scattering amplitude for near-grazing elevations at 125 Hz

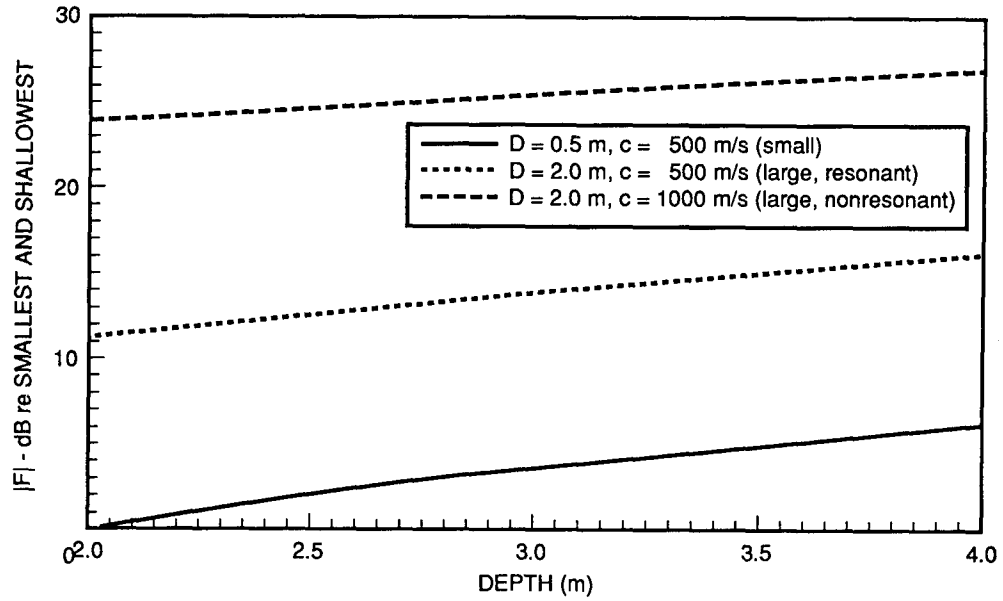

Fig. 16 – Scattering amplitude for near-grazing elevations as a function of plume center depth at 125 Hz. Vertical axis is in dB relative to the value for $D = 0.5$ m, $d = 2$ m.

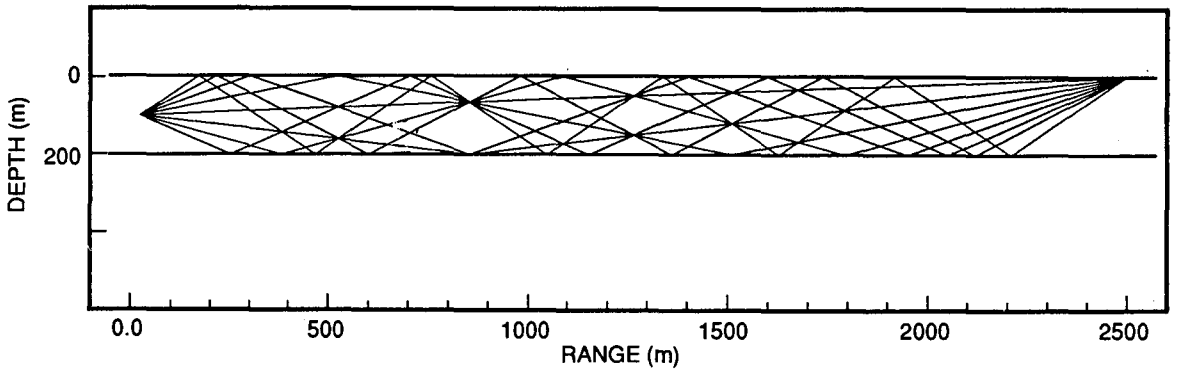

water sound speed	1500.0	m/s	range	2500.0	m
sediment sound speed	1750.0	m/s	source depth	100.0	m
water density	1.0	gm/cc	water depth	200.0	m
sediment density	1.8	gm/cc	critical angle	59.0	deg

Fig. 17 – Eigenray multipaths and simulation parameters

the eigenrays that undergo total reflection at the sediment in this geometry. The partially reflected rays all had power levels at least 16 dB lower and have been neglected. Figure 18 shows the azimuth dependence of the scattering at the lowest resonance frequency. This figure is a multipath version of Fig. 9. It has the necessary symmetry but the amplitude is larger in this case by a factor of more than twenty, which may at first glance seem unreasonably high. Indeed, even if all of the rays somehow managed to arrive at the direct path elevation (87.71°) and combine in phase, that could account for no more than a factor of eight. It turns out that most of this increase is caused by the strong dependence of the scattering amplitude on source elevation. The rays that produce the greatest response are those with the steepest grazing angles. In fact, separate simulations have shown that the steepest ray (elevation 59.04° and 4 bottom bounces) accounts for 60% of the total scattering response in Fig. 18 while the near-grazing direct arrival (87.71° elevation) produces only 3%. It may be worth noting here that, for shorter ranges, even some of the partially reflected rays may need to be included.

Figure 19 shows the scattering response as a function of output azimuth at the second resonance frequency. Here, as in Fig. 13, there are distinct forward and backward lobes due to the 'p-wave' nature of the resonance and the proximity of the pressure-release boundary. This is further illustrated in Figs. 20 and 21 which show the elevation dependence at the first and second resonances.

6.3 Effects of Nonspherical Plume Shape

In this section we consider the scattering response of the ellipsoidal plume shown in Fig. 6. The semiaxes are aligned with the standard x, y, z directions, but their lengths are in the proportions 1:2:3 so that this is not a figure of revolution. As before, the largest overall dimension is 2.0 m, so we are dealing with a plume that stands 2 m tall (in the z direction), has a width (y direction) of $1\frac{1}{3}$ m and is $\frac{2}{3}$ m thick (x direction).

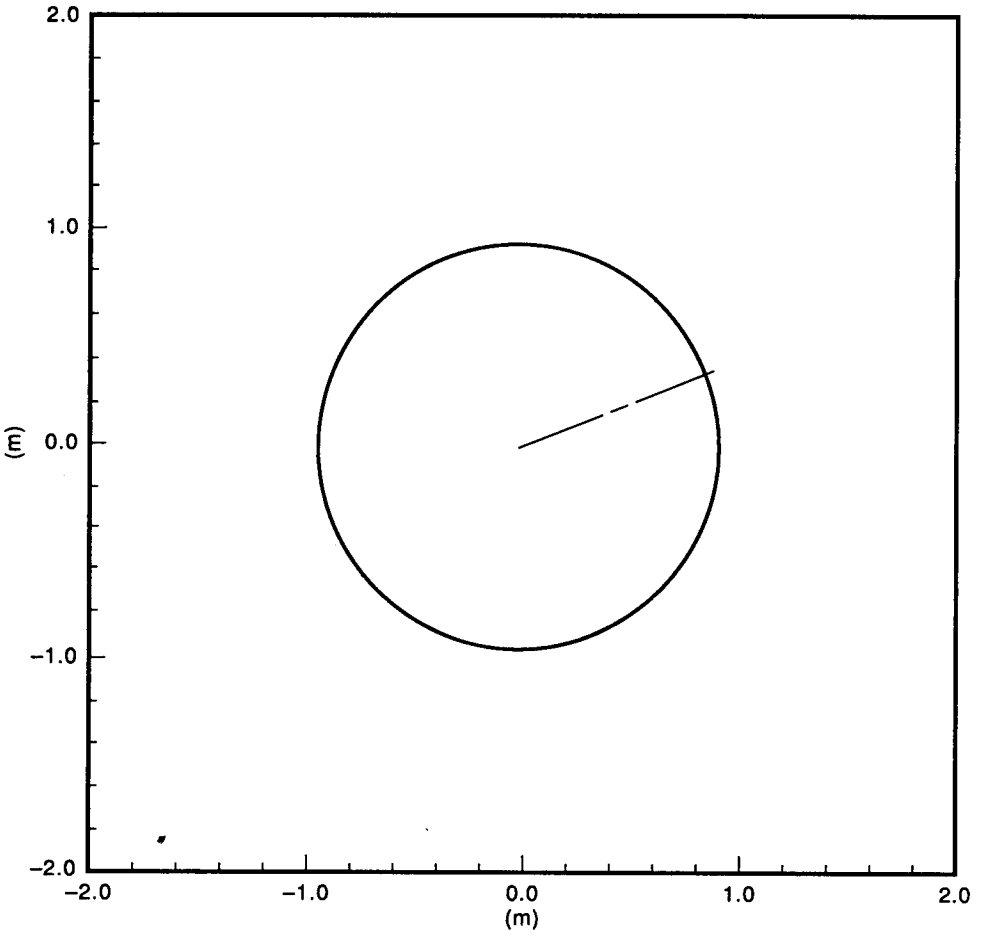

plume shape	overall size	interior svp	number of tiles	annealed wireframe?
sphere	2 m	uniform: 500 m/s	192	no

pressure-relief interface?	center depth	receiver direction	source direction	amplitude; phase of source(s)
yes	2 m	azim 0–360°	azim 22.50°	
		elev 85°	elev 87.71°	1.000; 0.00°
			elev 83.16°	0.994; 105.57°
			elev 78.69°	0.981; 31.60°
			elev 74.36°	0.964; 133.94°
			elev 70.20°	0.942; −112.10°
			elev 66.25°	0.916; −165.67°
			elev 62.53°	0.888; −111.52°
			elev 59.04°	0.858; 117.82°

Fig. 18 – Scattering amplitude as a function of azimuth at 125 Hz. This is a version of Fig. 9 with eight arrivals. For simplicity, only the $m = 4$ result is plotted.

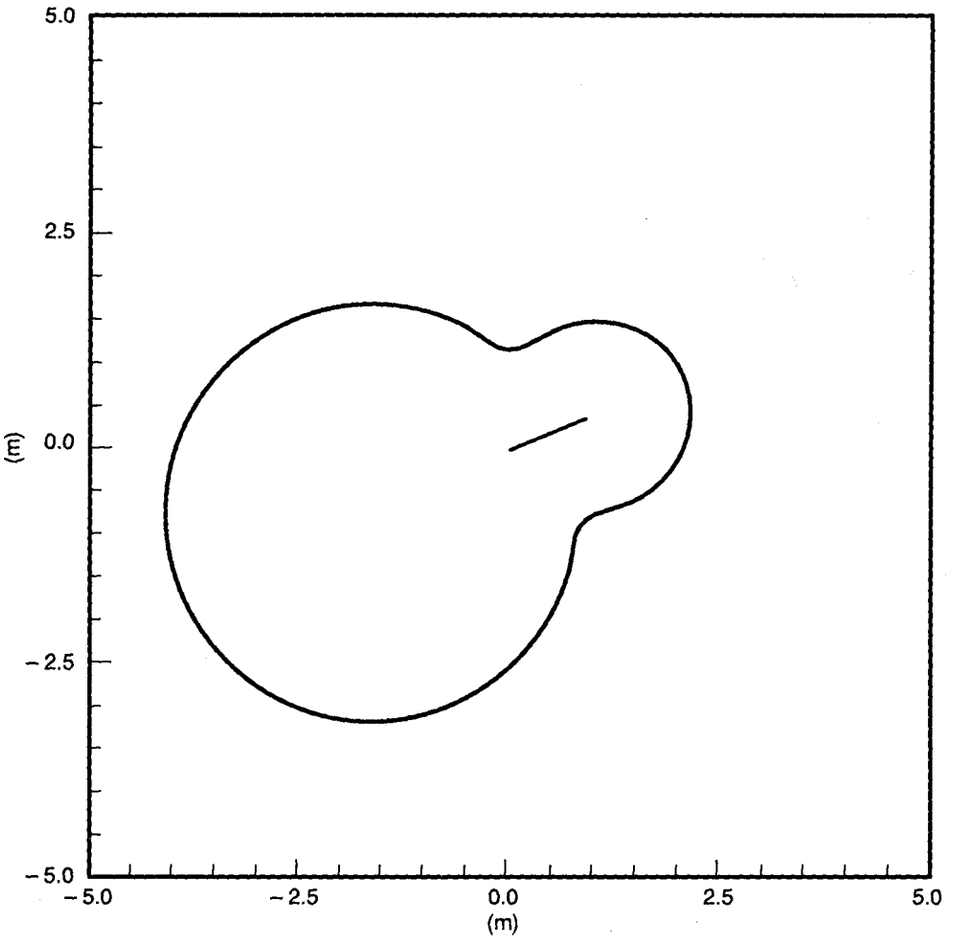

plume shape	overall size	interior svp	number of tiles	annealed wireframe?
sphere	2 m	uniform: 500 m/s	192	no

pressure-relief interface?	center depth	receiver direction	source direction	amplitude; phase of source(s)
yes	2 m	azim 0–360°	azim 22.50°	
		elev 85°	elev 87.71°	1.000; 0.00°
			elev 83.16°	0.994; 105.57°
			elev 78.69°	0.981; 31.60°
			elev 74.36°	0.964; 133.94°
			elev 70.20°	0.942; −112.10°
			elev 66.25°	0.916; −165.67°
			elev 62.53°	0.888; −111.52°
			elev 59.04°	0.858; 117.82°

Fig. 19 – Scattering amplitude as a function of azimuth at 240 Hz

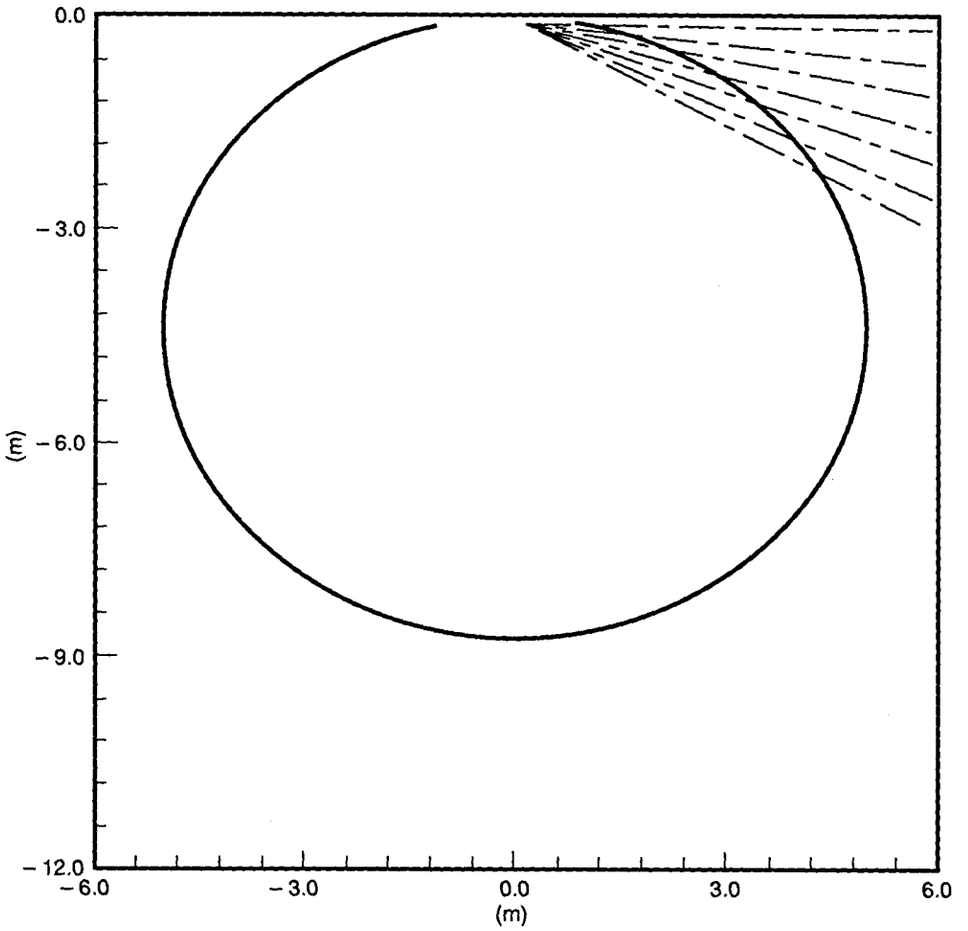

plume shape	overall size	interior svp	number of tiles	annealed wireframe?
sphere	2 m	uniform: 500 m/s	192	no

pressure-relief interface?	center depth	receiver direction	source direction	amplitude; phase of source(s)
yes	2 m	azim 202.5°, 22.5°	azim 22.50°	
		elev 0–90°	elev 87.71°	1.000; 0.00°
			elev 83.16°	0.994; 105.57°
			elev 78.69°	0.981; 31.60°
			elev 74.36°	0.964; 133.94°
			elev 70.20°	0.942; −112.10°
			elev 66.25°	0.916; −165.67°
			elev 62.53°	0.888; −111.52°
			elev 59.04°	0.858; 117.82°

Fig. 20 – Scattering amplitude as a function of elevation at 125 Hz

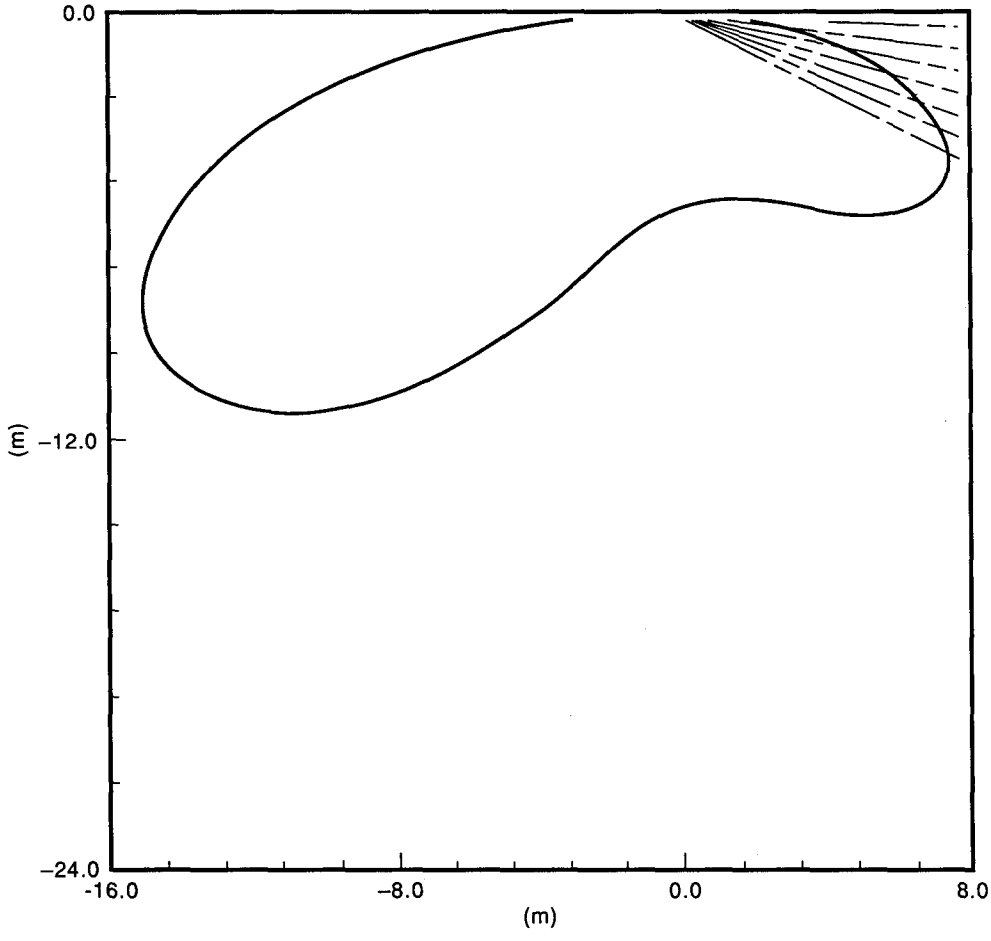

plume shape	overall size	interior svp	number of tiles	annealed wireframe?
sphere	2 m	uniform: 500 m/s	192	no

pressure-relief interface?	center depth	receiver direction	source direction	amplitude; phase of source(s)
yes	2 m	azim 202.5°, 22.5°	azim 22.50°	
		elev 0–90°	elev 87.71°	1.000; 0.00°
			elev 83.16°	0.994; 105.57°
			elev 78.69°	0.981; 31.60°
			elev 74.36°	0.964; 133.94°
			elev 70.20°	0.942; −112.10°
			elev 66.25°	0.916; −165.67°
			elev 62.53°	0.888; −111.52°
			elev 59.04°	0.858; 117.82°

Fig. 21 – Scattering amplitude as a function of elevation at 240 Hz

Figure 22 examines the resonance spectrum for scattering from this structure. To avoid unnecessary complications, this is done *without* the pressure-relief interface. The model results are plotted as circles — ○ for the nonannealed wireframe of Fig. 6 and • for the annealed wireframe of Fig. 7. Since this plume is physically smaller and less symmetric than the preceding spherical one, its resonant eigen-frequencies should be higher and less degenerate [16, Chapter VI, Section 2]. This expectation is supported by the vertical dashed lines that estimate the lowest few resonance frequencies according to analytic formulas from Morse and Feshbach [17, page 1420]. These formulas,

$$f \simeq \frac{c}{A}(0.7655 + 0.191e) \quad \cdots \quad B/A \approx 1 \tag{37}$$

and

$$f \simeq \frac{c}{\pi B}\left(1 + \frac{1}{6}(B/A)^2\right) \quad \cdots \quad B/A \ll 1, \tag{38}$$

yield the frequencies listed in Table 1. They actually represent estimates for the lowest resonance of a 2-D elliptical region with semi-axes A, B $(B < A)$ and eccentricity $e = \sqrt{1 - (B/A)^2}$. For the y-z plane, for example, $B/A = 2/3 = 0.67$. The interior sound speed is c and the exterior sound speed is effectively infinite. Equation (37) applies to a nearly circular ellipse and Eq. (38) to a highly eccentric one. Two observations may be made from Fig. 22. First, annealing is important since, without it, the result computed for the lowest resonance is about 20 % too high. Secondly, the locations of the resonances agree with the predictions from Morse and Feshbach [17] about as well as could be expected, considering that the latter derive from a 2-D depiction of the problem with $c_{ext} = \infty$. The lowest resonance, for example, is about 20 Hz below the 256 Hz estimate from Eq. (38). The nature of the peak at 540 Hz is not absolutely certain. A marginal tiling estimate indicates that the modeling results for this wireframe should be reliable up to at least 475 Hz. However, since this type of estimate has proved too conservative in the spherical case, the peak in question may well be an authentic spectral feature analogous to a p-wave peak for spherical plumes; i.e., a genuine resonance which is simply not predicted by Eqs. (37–38) because it is of higher order.

Table 1 — Approximate Resonance Frequencies from Morse and Feshbach

Plane of Ellipse	B/A	Frequency (Hz) From Eq. (37)	Frequency (Hz) From Eq. (38)
y-z	0.67	454	256
x-z	0.33	473	486
x-y	0.50	698	497

Figures 23 and 24 use the annealed wireframe and incorporate the pressure-relief interface. Like Figs. 9 and 12, they are done at the lowest resonance frequency of the plume concerned. However, because this plume is not symmetric with respect to the incident azimuth, Fig. 23 need not retain the circular symmetry of Fig. 9. A close inspection bears this out. The figure is flattened by a factor of 0.94 in y direction and exhibits reflection symmetry relative to the x and y axes rather than to the source direction. This is normal for the response of an object driven at an isolated resonance. Although the power level of the resonant radiation will certainly depend on the direction from which the object is excited, the directional pattern will depend only on the structure of the object. Figure 23 inherits its x-y symmetry from that of the plume. Likewise, the elevation display in Fig. 24 retains the forward/backward symmetry of the plume itself. Figure 24 also confirms the impression made by Fig. 22 that this lowest resonance is a lower Q feature for the flattened ellipsoid than for the sphere.

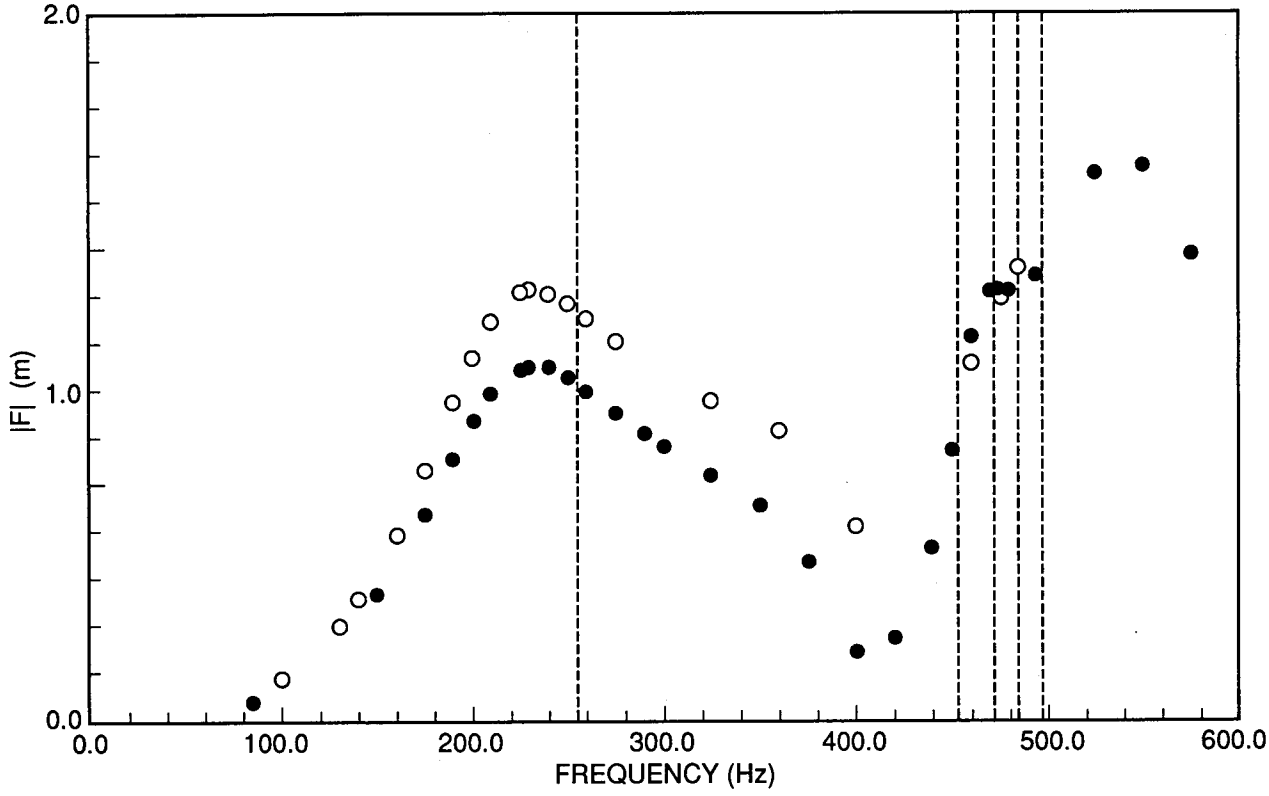

plume shape	overall size	interior svp	number of tiles	annealed wireframe?
ellipsoid (1:2:3)	2 m	uniform: 500 m/s	192	no – ○ yes – ●

pressure-relief interface?	center depth	receiver direction	source direction	amplitude; phase of source(s)
no	2 m	azim 157.5° elev 85°	azim 22.5° elev 88.5°	1.0; 0°

Fig. 22 – Scattering amplitude as a function of frequency. Dashed lines indicate analytic estimates of the resonance frequencies as described in the text.

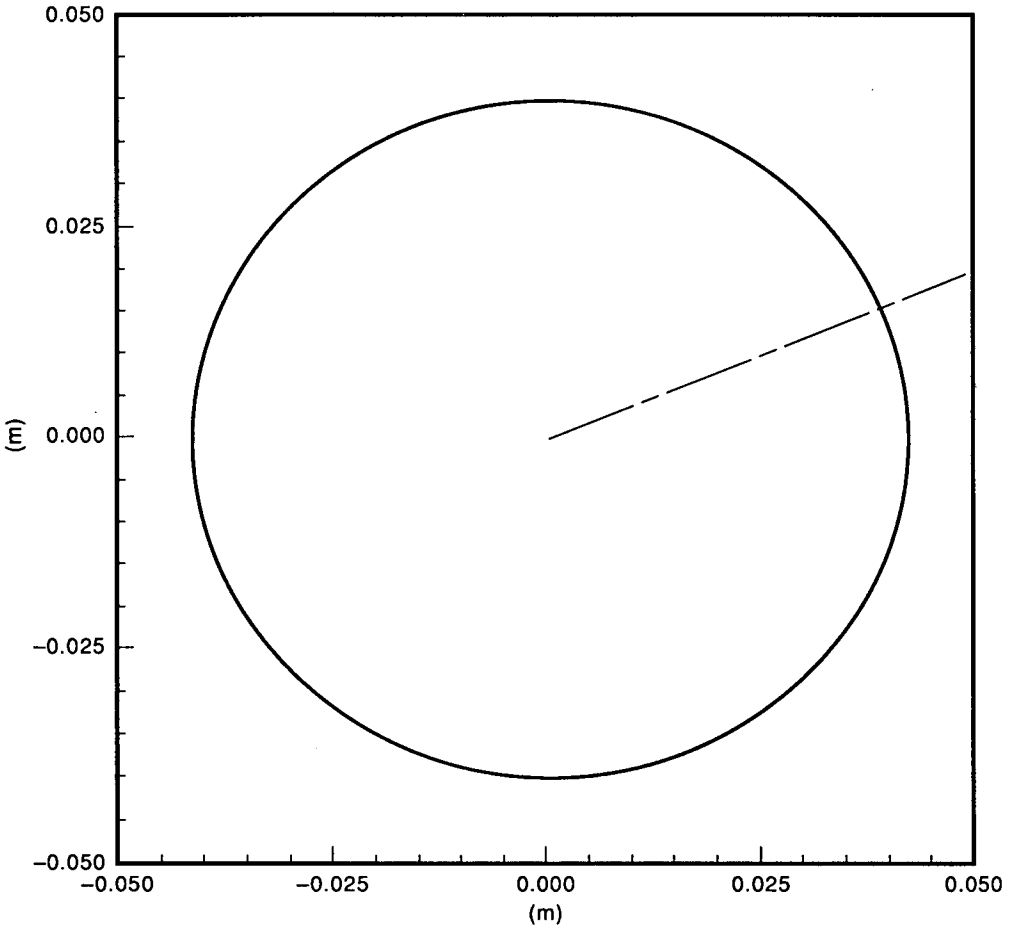

plume shape	overall size	interior svp	number of tiles	annealed wireframe?
ellipsoid (1:2:3)	2 m	uniform: 500 m/s	192	yes

pressure-relief interface?	center depth	receiver direction	source direction	amplitude; phase of source(s)
yes	2 m	azim 0–360° elev 85°	azim 22.5° elev 88°	1.0; 0°

Fig. 23 – Scattering amplitude as a function of azimuth at 240 Hz

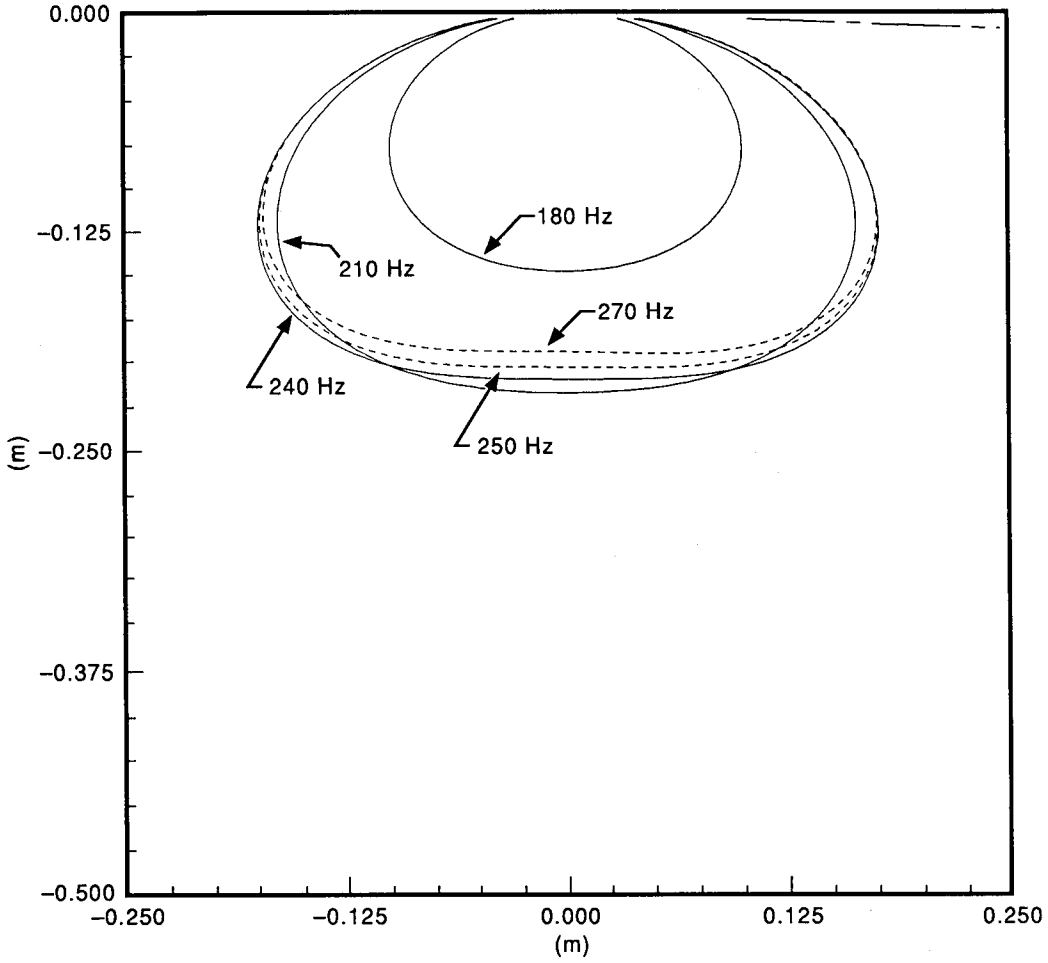

plume shape	overall size	interior svp	number of tiles	annealed wireframe?
ellipsoid (1:2:3)	2 m	uniform: 500 m/s	192	yes

pressure-relief interface?	center depth	receiver direction	source direction	amplitude; phase of source(s)
yes	2 m	azim 202.5°, 22.5° elev 0–90°	azim 22.5° elev 88°	1.0; 0°

Fig. 24 – Scattering amplitude as a function of elevation, parameterized by frequency. The discrete frequencies are 180, 210, 240 Hz (solid) and 250, 270 Hz (dashed).

6.4 Effects of the Gross Features of the Interior SVP

We continue with the ellipsoidal plume envelope from the previous section, but here we allow two features of the interior sound speed — the central value c_0 and the vertical gradient c' — to be adjustable parameters.

6.4.1 Weak Vertical Gradient

The gradient will be a constant $c' = 50$ (m/s)/m. Thus, relative to the sound speed c_0 at the center of the plume, the medium is 50 m/s slower at the top and 50 m/s faster at the bottom. Without firm data about the gradients actually present in intermediate plumes in the ocean, we are unable to be any more realistic about it. However, since buoyancy should concentrate more air at the top, this is at least a step in the right direction. For this case, Eq. (18) yields $\varepsilon_{WKB} \approx c'/\omega \approx 0.03$ so that the use of Eq. (19a) for the interior Green's function is well justified.

The first computation uses a sound speed of $c_0 = 500$ m/s at the center. Figure 25 examines the impact on the azimuth dependence of the scattering at 240 Hz. The solid curve is produced with the annealed wireframe of Fig. 7. It is indistinguishable from the result in Fig. 23 which has the same 500 m/s sound speed everywhere without any gradient. If a gradient of this size has any effect at all, it is not to be found at near-grazing elevations. It was anticipated that annealing might be especially important here because its effect is to reconfigure the tiles of the upper half of the wireframe so as to improve coverage near the top where the shortest interior wavelengths occur. The dashed curve was computed using the unannealed wireframe of Fig. 6. Evidently, annealing is important here too, although no more so than in the constant-svp case of Fig. 22. Figure 26 shows the effect of the sound speed gradient on the elevation and frequency dependence. Again, the sound speed gradient makes virtually no difference. There are only a few minor deviations from Fig. 24, mainly at higher frequencies. The conclusion is clearly that interior sound speed gradients in this regime are unimportant.

6.4.2 Reduced Central Speed

Figure 27 examines the impact of the central sound speed on the azimuth dependence — again at 240 Hz. The weak sound speed gradient is retained but the speed at the center of the plume is reduced to $c_0 = 400$ m/s. Again, the solid curve is produced with the annealed wireframe. This curve differs from the one in Fig. 25 in two important respects: (a) the level of the scattered radiation is reduced and (b) although the entire plume is still reflection-symmetric with respect to the x and y axes, its scattering response no longer is. Both phenomena can be explained by the fact that, due to its altered internal structure, this plume is no longer being driven at resonance. Whenever a driven system is detuned from a resonance, its output level is lowered by an amount related to the Q of the resonance and the amount of detuning. The asymmetry here is to be expected for any case that is not dominated by a single resonance. When the frequency lies between two resonance peaks, they both affect the scattering response and neither one can fully impose its characteristic symmetry on the result.

Figure 28 shows the effect of the lower central sound speed on the elevation and frequency dependence. The "groundstate" resonance, which was in the 210 to 240 Hz range when c_0 was 500 m/s, has been shifted down to at least 180 Hz — roughly in proportion to c_0, as would be expected. As anticipated from its slight asymmetry, the 240 Hz azimuth response shown in Fig. 27 is somewhat off resonance (by roughly 30 to 60 Hz).

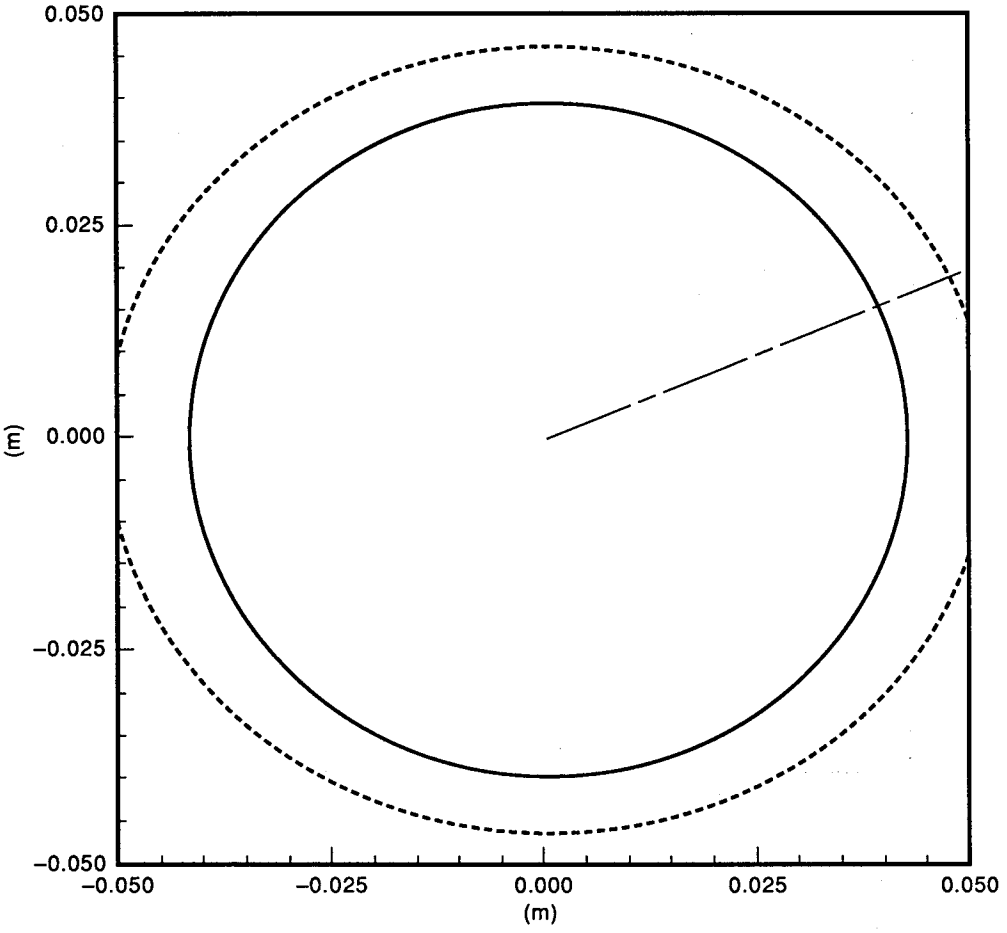

plume shape	overall size	interior svp	number of tiles	annealed wireframe?
ellipsoid (1:2:3)	2 m	at center: 500 m/s z-gradient: 50 (m/s)/m	192	no – dashed yes – solid

pressure-relief interface?	center depth	receiver direction	source direction	amplitude; phase of source(s)
yes	2 m	azim 0–360° elev 85°	azim 22.5° elev 88°	1.0; 0°

Fig. 25 – Scattering amplitude as a function of azimuth at 240 Hz. This is a version of Fig. 23 with a vertical gradient in the interior svp, both with and without annealing in the wireframe construction.

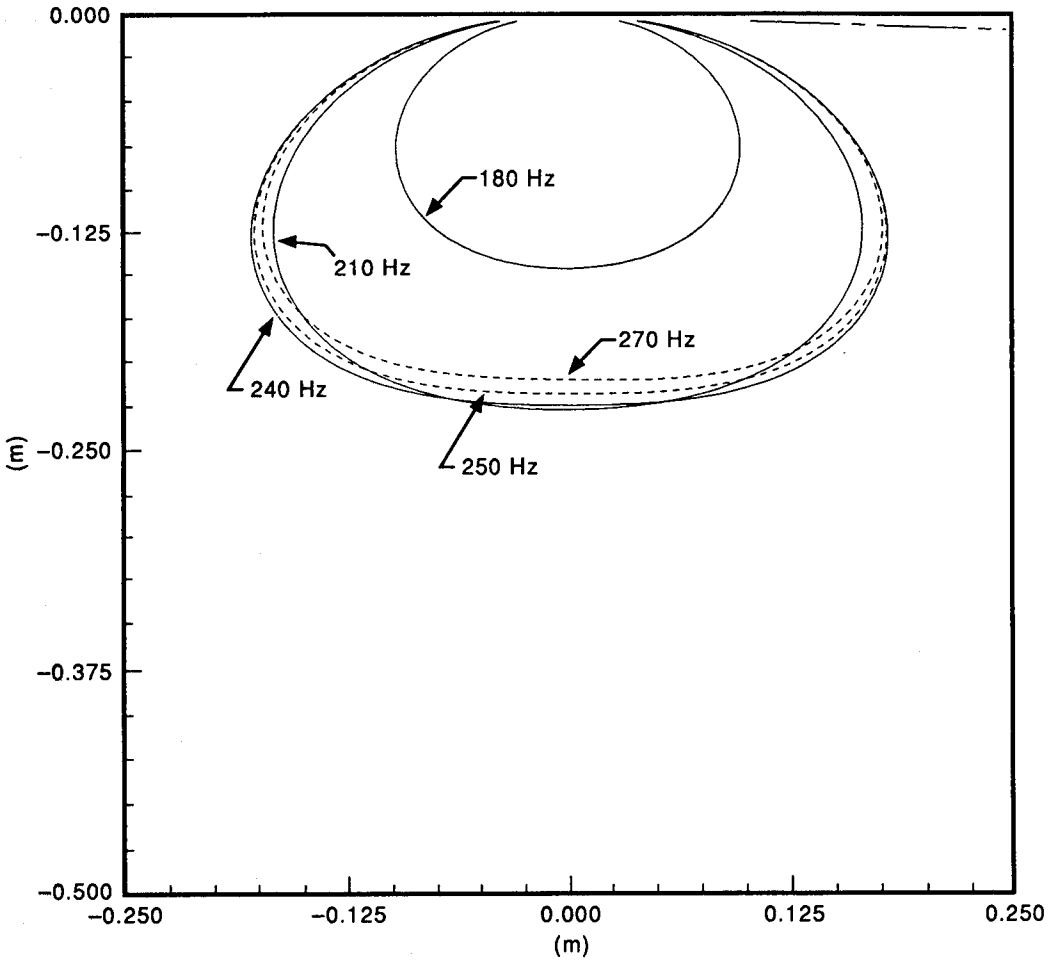

plume shape	overall size	interior svp	number of tiles	annealed wireframe?
ellipsoid (1:2:3)	2 m	uniform: 500 m/s z-gradient: 50 (m/s)/m	192	yes

pressure-relief interface?	center depth	receiver direction	source direction	amplitude; phase of source(s)
yes	2 m	azim 202.5°, 22.5° elev 0°	azim 22.5° elev 88°	1.0; 0°

Fig. 26 – Scattering amplitude as a function of elevation, parameterized by frequency. The discrete frequencies are 180, 210 and 240 Hz (solid) and 250 and 270 Hz (dashed). This is similar to Fig. 24 but with a weak vertical gradient in the interior svp.

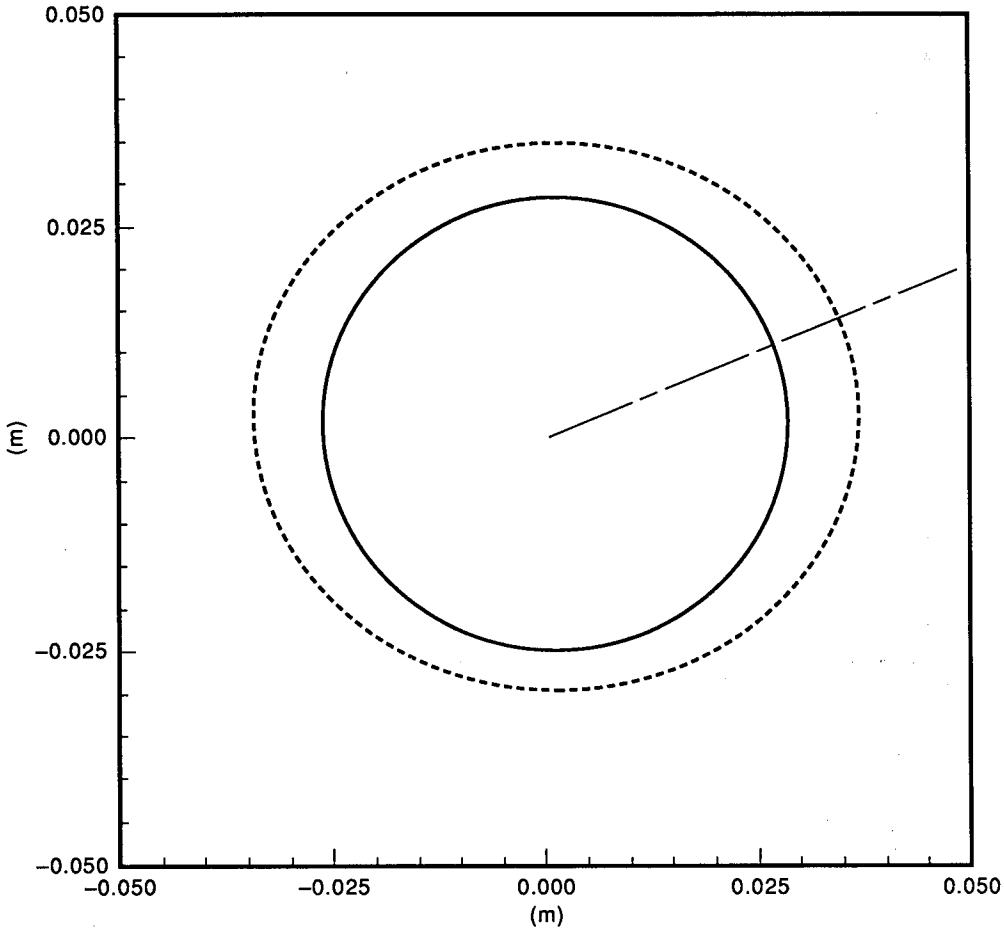

plume shape	overall size	interior svp	number of tiles	annealed wireframe?
ellipsoid (1:2:3)	2 m	at center: 400 m/s z-gradient: 50 (m/s)/m	192	no – dashed yes – solid

pressure-relief interface?	center depth	receiver direction	source direction	amplitude; phase of source(s)
yes	2 m	azim 0–360° elev 85°	azim 22.5° elev 88°	1.0; 0°

Fig. 27 – Scattering amplitude as a function of azimuth at 240 Hz. This is a version of Fig. 25 with a lower central sound speed, both with and without annealing in the wireframe construction.

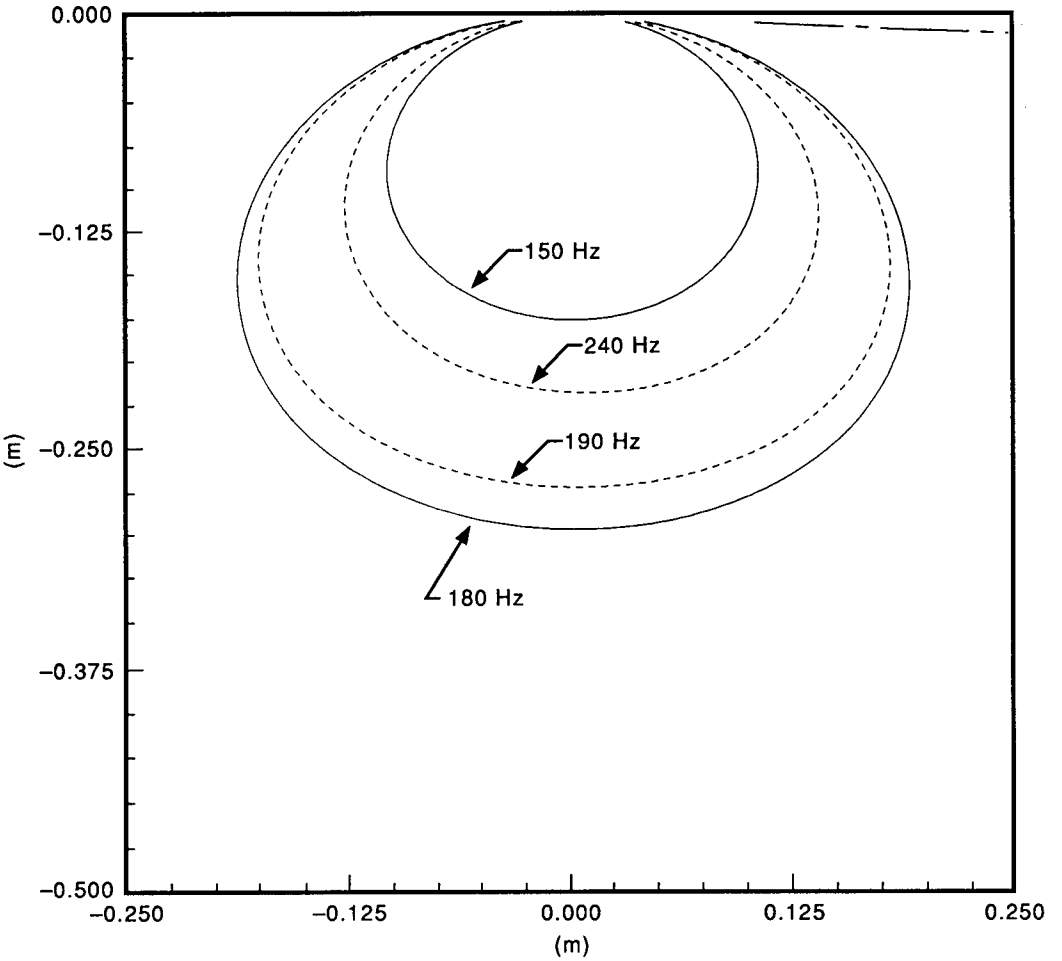

plume shape	overall size	interior svp	number of tiles	annealed wireframe?
ellipsoid (1:2:3)	2 m	at center: 400 m/s z-gradient: 50 (m/s)/m	192	yes

pressure-relief interface?	center depth	receiver direction	source direction	amplitude; phase of source(s)
yes	2 m	azim 202.5°, 22.5° elev 0°	azim 22.5° elev 88°	1.0; 0°

Fig. 28 – Scattering amplitude as a function of elevation, parameterized by frequency. The discrete frequencies are 150 and 180 Hz (solid) and 190 and 240 Hz (dashed). This is similar to Fig. 26 with a lower central sound speed.

6.4.3 Strong Vertical Gradient

We now return c_0 to its original value of 500 m/s and apply the strongest gradient that we can accommodate with confidence in the neighborhood of 240 Hz. First we adopt a maximum allowable value of 0.2 for the parameter $\varepsilon_{WKB} \approx c'/\omega$ to be used in the modeling. Since $\varepsilon_{WKB} \ll 1$, we are justified in using Eq. (19a) for the interior Green's function. Then we use the maximum gradient consistent with that choice at 240 Hz; i.e., $c' = 0.2 \times 2\pi \times 240 \approx 300$ (m/s)/m. It may be seen in Fig. 29 that the effect of this strong vertical gradient is to sharpen the resonance (raise the Q) but not to shift it.

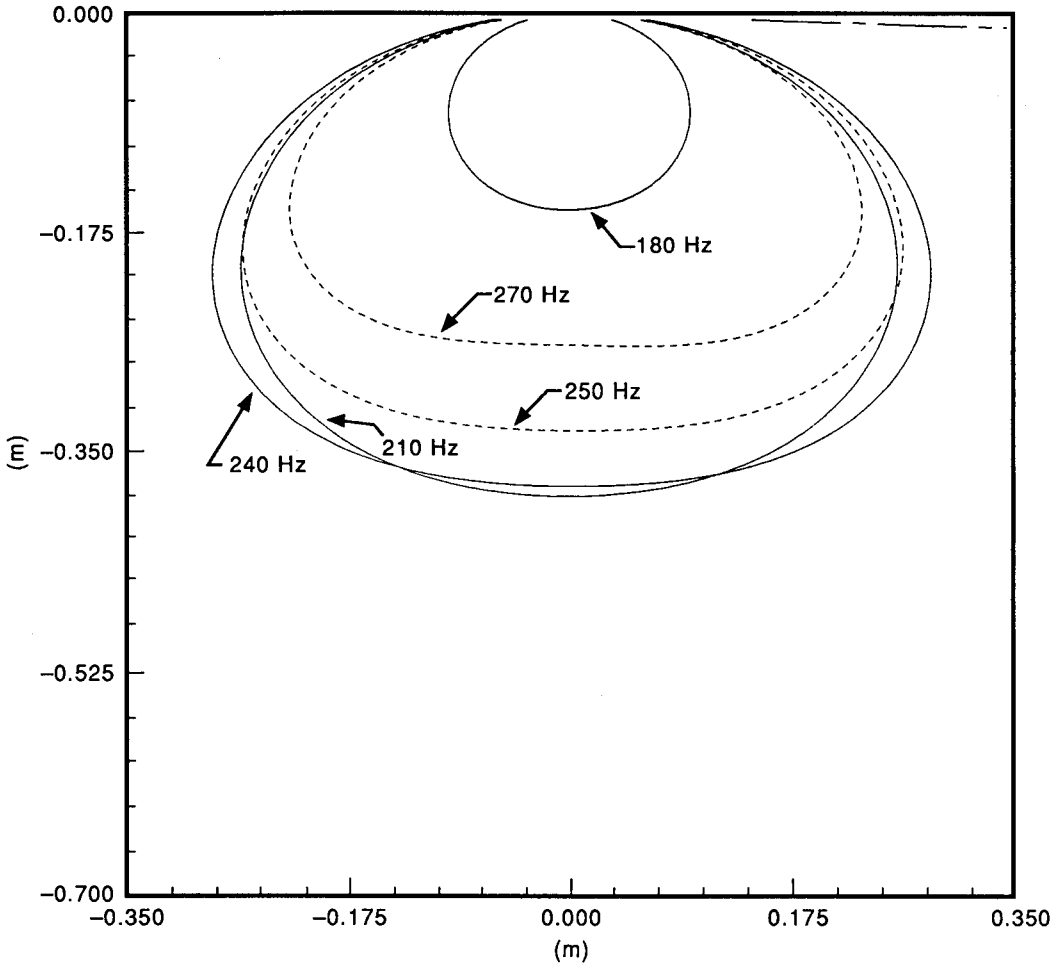

plume shape	overall size	interior svp	number of tiles	annealed wireframe?
ellipsoid (1:2:3)	2 m	uniform: 500 m/s z-gradient: 300 (m/s)/m	192	yes

pressure-relief interface?	center depth	receiver direction	source direction	amplitude; phase of source(s)
yes	2 m	azim 202.5°, 22.5° elev 0°	azim 22.5° elev 88°	1.0; 0°

Fig. 29 – Scattering amplitude as a function of elevation, parameterized by frequency. The discrete frequencies are 180 210 and 240 Hz (solid) and 250 and 270 Hz (dashed). This is similar to Fig. 24 but with a strong vertical gradient in the interior svp.

7. SUMMARY AND CONCLUSIONS

We have developed a numerical implementation of the boundary integral treatment of scattering from acoustically penetrable bubble structures of very general type. The underlying theory includes the effects of collective bubble resonances and our implementation provides options for the presence of a pressure-release sea surface and for coherent multipath arrivals. The implementation, in the form of the BIRPS software, provides a numerical modeling component for the investigation of low-frequency surface reverberation and has the potential for wider application to the study of resonant scattering from other complex bodies.

We have been able to compute the complex scattering amplitudes of model structures at frequencies up to a few hundred Hz for a range of size, shape, depth, and interior sound speed profile. These computations were done with parameter values chosen to simulate plumes of the "intermediate" type. We find that such plumes have multiple weak-to-moderate resonances in the sub-kHz band of interest. The nonresonant scattering response for near-grazing geometries is about 10 dB higher than point-target levels and tends be linear in the depth near 2 m, changing to quadratic by 4 m. Resonance adds approximately another 10 dB to the level and extends the linear dependence to greater depths. Typically, the lowest-frequency resonance is a low-Q feature whose response has a weak frequency dependence with a vertical dipole-like dependence on elevation angle. As frequency is increased, the next resonance encountered has a higher Q and exhibits forward and backward scattering lobes. As the driving frequency is swept upward through such a resonance, the dominant component of the response shifts from backscattering to forward scattering at a rate dependent on the Q. Features with a significant impact on the resonance spectrum of a plume, and on the scattering response in general, are the "primary parameters" (size, shape, and mean interior sound speed) and the depth. Strong sound speed gradients enhance the Q of the resonant responses, while weak gradients have no appreciable effect.

This work has focused on the resonance effects of bubble structures. We have neglected "tenuous" bubble clouds (the large, persistent features sustained by Langmuir circulation) for that reason. These may be of considerable potential importance in ocean acoustics, but they are weak, nonresonant scatterers. This neglect, however, was purely a matter of emphasis. The BIRPS software is certainly also applicable to tenuous clouds and may be useful in that regime, particularly as a means of validating the approximations made in other approaches.

Two limitations of the present technique are that it treats the sea surface as flat and the plume as static. Although surface curvature on a scale comparable to plume dimensions would need separate treatment, curvature on larger and smaller scales could be addressed with only moderate additional effort. For example, swell might be simulated as a time-dependent surface tilt and small-scale roughness could be incorporated in a surface reflection coefficient. As it stands, our approach could deal with scattering from plumes of the "dense" class — provided they remained static. (Very strong interior sound speed gradients, if present in such plumes, would require an improved formulation of the interior Green's function, but the approach is still sound.) Actual dense plumes, however, have such short lifetimes that the present CW implementation of BIRPS is probably not adequate for them. Such fast-evolving structures would require a broadband implementation to represent their time-dependent scattering. Incorporating surface swell and roughness and broadband signal capability into BIRPS are promising areas for future work.

The work reported in this publication was not done in a vacuum. Numerous sources have proved valuable to the authors in acquiring the background to tackle the subject and a few have provided inspiration for the particular approach adopted here. We have included a complete account of this in Appendix G to help put our work in context and to assure that appropriate credit is given.

8. ACKNOWLEDGMENTS

This work was supported by the Office of Naval Research, Code 1125OA and by the Office of Naval Technology, Code 234. The authors also wish to thank Dr. Nolan R. Davis for his advice and assistance on the subject of simulated annealing.

REFERENCES

1. P. M. Ogden and F. T. Erskine, "An Empirical Prediction Algorithm for Low-Frequency Acoustic Surface Scattering Strengths," NRL Report 9377, April 1992.

2. R. J. Urick, *Fundamentals of Underwater Sound* (McGraw-Hill, New York, 1985).

3. K. W. Commander and A. Prosperetti, "Linear Pressure Waves in Bubbly Liquids: Comparison Between Theory and Experiment," *J. Acoust. Soc. Am.* **85**, 732–746 (1989).

4. S. A. Thorpe, "On the Clouds of Bubbles Formed by Breaking Wind Waves in Deep Water, and their Role in Air-Sea Gas Transfer," *Phil. Trans. Roy. Soc. London* **A304**, 155–210 (1982).

5. E. C. Monahan and M. Lu, "Acoustically Relevant Bubble Assemblages and their Dependence on Meteorological Parameters," *IEEE J. Oceanic Eng.* **OE-15**, 340–349 (1990).

6. R. Kittappa and R. E. Kleinman, "Acoustic Scattering by Penetrable Homogeneous Objects," *J. Math. Phys.* **16**, 421–432 (1975).

7. E. Mertzbacher, *Quantum Mechanics* (Wiley & Son, New York, 1961).

8. D. Colton and R. Kress, *Integral Equation Methods in Scattering Theory* (Wiley-Interscience, New York, 1983).

9. F. Ingenito, "Scattering from an Object in a Stratified Medium," *J. Acoust. Soc. Am.* **82**, 2051–2059 (1987).

10. J. Perkins, W. A. Kuperman, K. D. Heaney, and G. T. Murphy, "Scattering from an Object in a Three-Dimensional Ocean," presented at the 20th annual Technical Cooperation Program (TTCP), Subgroup G, Technical Panel GTP–9, Sonar Technology, NUSC, New London CT, October 1991.

11. W. H. Press, B. P. Flannery, S. A. Teukolsky, and W. T. Vetterling, *Numerical Recipes* (Cambridge University Press, Cambridge, 1986).

12. D. Farmer, T. Ewart, F. Henyey, K. Melville, and A. Prosperetti, "Tests of Hypotheses for Enhanced Surface Reverberation at Low Frequencies," ONR Air-Sea Executive Committee memo (December 1991).

13. F. S. Henyey, "Acoustic Scattering from Ocean Microbubble Plumes in the 100 Hz to 2 kHz Region," *J. Acoust. Soc. Am.* **80**, 399–405 (1991).

14. B. E. McDonald, "Echoes from Vertically Striated Subresonant Bubble Clouds: A Model for Ocean Surface Reverberation," *J. Acoust. Soc. Am.* **89**, 617–622 (1991).

15. S. W. Yoon, L. A. Crum, A. Prosperetti, and N. Q. Lu, "An Investigation of the Collective Oscillations of a Bubble Cloud," *J. Acoust. Soc. Am.* **89**, 700–706 (1991).

16. R. Courant and D. Hilbert, *Methods of Mathematical Physics, Vol. I* (Interscience, New York, 1953).

17. P. M. Morse and H. Feshbach, *Methods of Mathematical Physics* (McGraw-Hill, New York, 1953).

Appendix A

UNIFORM 1-D OBJECT

This appendix reviews the solution to the one-dimensional problem of CW scattering by a uniform object, as shown in Fig. A1. For simplicity, the density is the same inside and outside the scatterer. For a unit-amplitude field incident from the left, the solution is found via the following steps:

1. Form the total field in each region —

$$\begin{array}{cc} \underline{\text{field}} & \underline{\text{region}} \\ 1e^{+ik_1x} + Re^{-ik_1x} & -\infty < x < 0 \\ Ae^{+ik_0x} + Be^{-ik_0x} & 0 < x < w \\ Te^{+ik_1x} & w < x < +\infty \ . \end{array} \tag{A1}$$

   R and T are the complex reflection and transmission coefficients.

2. Impose continuity on the field and its x-derivative at $x = 0,\ w$.

3. Solve the resulting equations for $T,\ R$.

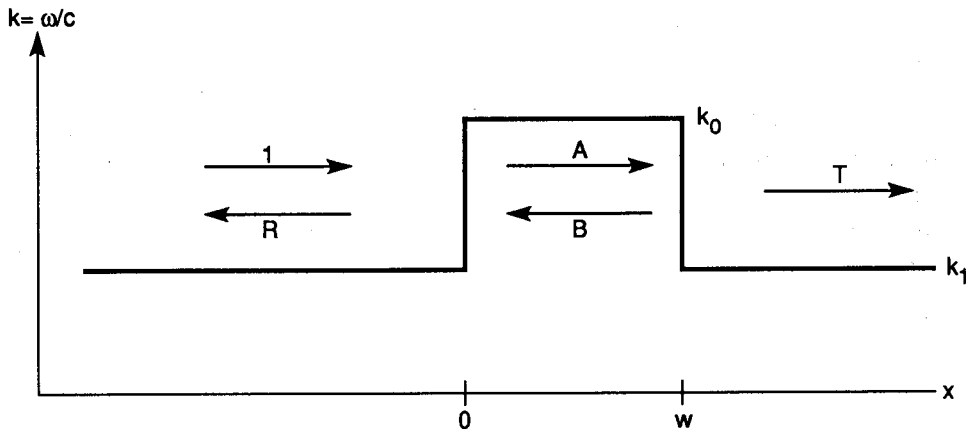

Fig. A1 – Sketch of a 1-D problem, showing the notation used

It is easily seen that, with $\mu = e^{+ik_0 w}$, the conditions that accomplish step 2 are

$$\begin{pmatrix} \mu & \mu^* & 0 & -1 \\ k_0\mu & -k_0\mu^* & 0 & -k_1 \\ 1 & 1 & -1 & 0 \\ k_0 & -k_0 & k_1 & 0 \end{pmatrix} \begin{pmatrix} A \\ B \\ R \\ T \end{pmatrix} = \begin{pmatrix} 0 \\ 0 \\ 1 \\ k_1 \end{pmatrix}. \tag{A2}$$

With the determinant

$$D = \begin{vmatrix} \mu & \mu^* & 0 & -1 \\ k_0\mu & -k_0\mu^* & 0 & -k_1 \\ 1 & 1 & -1 & 0 \\ k_0 & -k_0 & k_1 & 0 \end{vmatrix} = (k_1 + k_0)^2\mu^* - (k_1 - k_0)^2\mu, \tag{A3}$$

we have

$$AD = \begin{vmatrix} 0 & \mu^* & 0 & -1 \\ 0 & -k_0\mu^* & 0 & -k_1 \\ 1 & 1 & -1 & 0 \\ k_0 & -k_0 & k_1 & 0 \end{vmatrix} = 2\mu^* k_1(k_1 + k_0) \tag{A4}$$

$$BD = \begin{vmatrix} \mu & 0 & 0 & -1 \\ k_0\mu & 0 & 0 & -k_1 \\ 1 & 1 & -1 & 0 \\ k_0 & k_1 & k_1 & 0 \end{vmatrix} = -2\mu k_1(k_1 - k_0) \tag{A5}$$

$$RD = \begin{vmatrix} \mu & \mu^* & 0 & -1 \\ k_0\mu & -k_0\mu^* & 0 & -k_1 \\ 1 & 1 & 1 & 0 \\ k_0 & -k_0 & k_1 & 0 \end{vmatrix} = -2i(k_1 - k_0)(k_1 + k_0)\sin(k_0 w) \tag{A6}$$

$$TD = \begin{vmatrix} \mu & \mu^* & 0 & 0 \\ k_0\mu & -k_0\mu^* & 0 & 0 \\ 1 & 1 & -1 & 1 \\ k_0 & -k_0 & k_1 & k_1 \end{vmatrix} = 4k_0 k_1 \ . \tag{A7}$$

Resonances may be located graphically by plotting $|R|$ or $|T|$ vs frequency. They should occur at approximately the frequencies where the bound states occur in the $c \to \infty$ limit, namely at $f = n\,\Delta f$ for $n > 0$, with an even spacing $\Delta f = c_0/2w$. This is borne out in the body of the report in Fig. 1. From that figure it is also clear that, even without attenuation, the acoustic resonances have finite widths.

Appendix B

SURFACE TILE INTEGRALS

This appendix evaluates W_n and S_n — the integrals that appear in the matrix elements of the wireframe continuity condition of Section 4.

Let $\mathbf{v}_1$, $\mathbf{v}_2$, $\mathbf{v}_3$ denote vectors from the center of the plume to the vertices of the nth tile. The endpoint of the vector $\mathbf{v} = (\mathbf{v}_1 + \mathbf{v}_2 + \mathbf{v}_3)/3$, then, lies at the geometric center of the tile. We will scale $\mathbf{v}$ up or down as required so that its endpoint lies on the plume itself and denote the resulting vector by $\mathbf{a}$. Thus, the endpoints of $\mathbf{v}_1$, $\mathbf{v}_2$, $\mathbf{v}_3$ form the base of a pyramid whose apex is at $\mathbf{a}$ as in Fig. B1. The vectors $\mathbf{p}_j = \mathbf{v}_j - \mathbf{a}$ locate the corners of that pyramid relative to the apex.

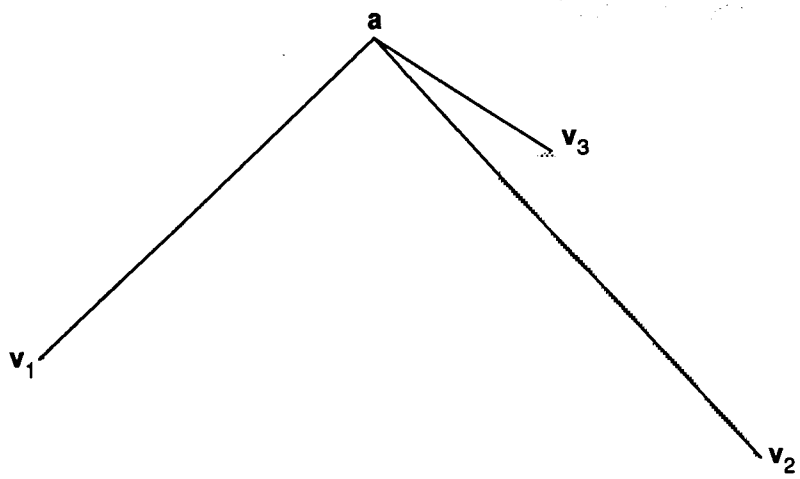

Fig. B1 – Pyramid having a tile as its base and its apex on the bubble plume

We first consider the shaded triangular part of one face of the pyramid shown in Fig. B2, with $\mathbf{r} = (r, \theta)$ denoting a radius vector from the apex to a point lying on that face, and compute

$$M = \int\int r\, dr\, d\theta \left(\frac{1}{r}\right)$$

over this region by adding the contributions from the subregions I and II: $M = M_I + M_{II}$ where

$$M_I = \int_0^{\Theta} d\theta \int_0^{q} dr = \Theta q \tag{B1}$$

$$M_{II} = \int_q^{p} dr \int_{\cos^{-1}(q/r)}^{\Theta} d\theta$$

$$= (p-q)\Theta - \int_q^{p} dr\, \cos^{-1}(q/r)\ . \tag{B2}$$

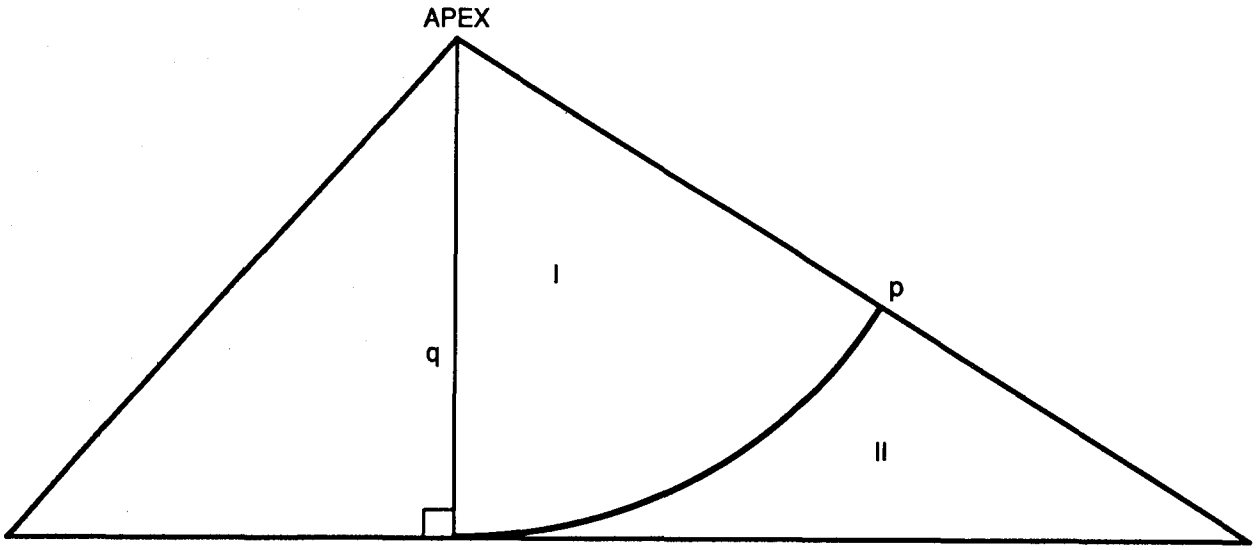

Fig. B2 – A pyramid face with polar coordinates

Addition and a little algebra result in

$$M = pH(q/p) \tag{B3}$$

where

$$H(\xi) = \xi \log\left(\frac{1+\sqrt{1-\xi^2}}{\xi}\right) . \tag{B4}$$

W_n is the sum of the contributions from all six such regions (two for each face). In terms of the perpendicular distance,

$$q_{ij} = \frac{|\mathbf{p}_i \times \mathbf{p}_j|}{|\mathbf{p}_i - \mathbf{p}_j|} \tag{B5}$$

from the apex to base edge i-j as shown in Fig. B3,

$$\begin{aligned} W_n &= p_1\left(H\left(\frac{q_{31}}{p_1}\right) + H\left(\frac{q_{12}}{p_1}\right)\right) \\ &+ p_2\left(H\left(\frac{q_{12}}{p_2}\right) + H\left(\frac{q_{23}}{p_2}\right)\right) \\ &+ p_3\left(H\left(\frac{q_{23}}{p_3}\right) + H\left(\frac{q_{31}}{p_3}\right)\right) . \end{aligned} \tag{B6}$$

The roughest estimate for S_n would be simply the area of the tile; i.e., the area of the pyramid's base

$$S_n = |\mathbf{p}_1 \times \mathbf{p}_2 + \mathbf{p}_2 \times \mathbf{p}_3 + \mathbf{p}_3 \times \mathbf{p}_1|/2 . \tag{B7}$$

We use a more accurate estimate,

$$S_n = \left(|\mathbf{p}_1 \times \mathbf{p}_2| + |\mathbf{p}_2 \times \mathbf{p}_3| + |\mathbf{p}_3 \times \mathbf{p}_1|\right)/2 , \tag{B8}$$

the sum of the areas of the three faces. The improvement that this provides over Eq. (B7) is significant when the height of the pyramid is a significant fraction of its base; i.e., when the number of tiles is small.

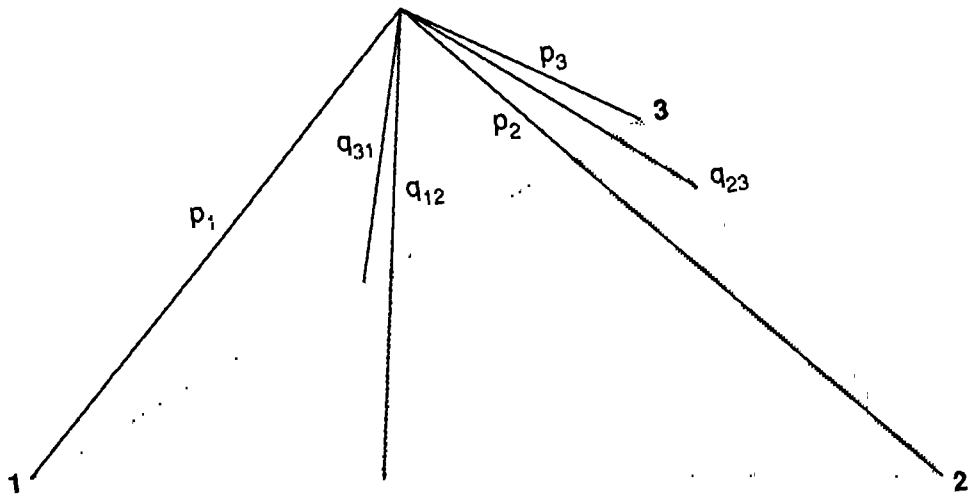

Fig. B3 – Pyramid showing p_j and q_{ij} for all three faces

Appendix C

DIAGONAL MATRIX ELEMENTS

To obtain the diagonal matrix elements given in Eq. (28), it is necessary to evaluate Eqs. (17) and (19) in the limit $\vec{x} \to \vec{x}_m$ where $\vec{x}_m$ is the coordinate at the center of the mth tile. In this limit, singularities occur in the integrands. These are dealt with as follows. The integrand is expanded in a Laurent series about the point $|\vec{x} - \vec{x}_m| = 0$. Cancellations occur, and at worst only a simple pole in $|\vec{x} - \vec{x}_m|$ remains. This quantity is integrable over the two-dimensional surface of the tile, and it is evaluated analytically. The resulting nonsingular expressions are suitable for numerical evaluation.

An intermediate result crucial to obtaining the Laurent series is given by

$$\lim_{\vec{x}\to\vec{x}_m} \frac{\hat{n}\cdot\hat{u}}{u} = -\frac{1}{2}\hat{u}\cdot\overleftrightarrow{\rho}_{\vec{x}_m}\cdot\hat{u} - \frac{1}{3}\hat{u}_i\hat{u}_j\hat{u}_k\chi^{ijk}_{\vec{x}_m}\,, \tag{C1}$$

where $\vec{u} \equiv \vec{x} - \vec{x}_m$ and $\overleftrightarrow{\rho}_{\vec{x}_m}$ is the curvature tensor $\overleftrightarrow{\rho} = (1 - \hat{n}\hat{n})\cdot\vec{\nabla}\hat{n}$ evaluated at $\vec{x} = \vec{x}_m$. The third order tensor χ is related to the second derivative of the normal. Terms containing $\chi_{\vec{x}_m}$ eventually vanish when angular integrations are performed. For a sphere of radius R,

$$\rho = -\frac{1}{R}\begin{pmatrix} 1 & 0 \\ 0 & 1 \end{pmatrix}. \tag{C2}$$

Equation (C1) was derived by using a coordinate system with the z-axis normal to the surface at $\vec{x}_m$. An expansion in the surface height was performed, and finally, the results were converted to a coordinate-independent form.

With W_m as defined in Appendix B, and assuming for the moment that no air-sea interface is present, the diagonal matrix elements are

$$A_{mm} = \frac{1}{16\pi}\left(1 - \frac{\rho_{ext}}{\rho_{int}}\right)\mathrm{Tr}(\rho)\,W_m - \frac{i}{8\pi}\frac{\rho_{ext}}{\rho_{int}}\hat{n}(\vec{x}_m)\cdot\vec{\nabla}k_{int}(\vec{x}_m)\,S_m \tag{C3}$$

$$B_{mm} = \frac{i\,(k_{ext} - k_{int}(\vec{x}_m))}{4\pi}S_m \tag{C4}$$

$$\begin{aligned} C_{mm} = {} & \frac{1}{8\pi}\left(k^2_{ext} - k^2_{int}(\vec{x}_m)\right)W_m + \frac{i}{12\pi}\left(k^3_{ext} - k^3_{int}(\vec{x}_m)\right)S_m \\ & + i\left[-\frac{1}{6}\mathrm{Tr}\left(\vec{\nabla}_T\vec{\nabla}_T k_{int}(\vec{x}_m)\right) + \frac{1}{4}\mathrm{Tr}(\rho)\,\hat{n}(\vec{x}_m)\cdot\vec{\nabla}k_{int}(\vec{x}_m)\right]S_m \end{aligned} \tag{C5}$$

$$D_{mm} = \frac{1}{16\pi}\left(1 - \frac{\rho_{int}}{\rho_{ext}}\right)\mathrm{Tr}(\rho)\,W_m + \frac{i}{8\pi}\frac{\rho_{int}}{\rho_{ext}}\hat{n}(\vec{x}_m)\cdot\vec{\nabla}k_{int}(\vec{x}_m)\,S_m. \tag{C6}$$

The operator $\vec{\nabla}_T$ is the derivative tangential to the surface. Recall that the ansatz used to generate the interior Green's function implicitly made use of the WKB approximation. In the version of the approximation used, the second derivative of k_{int} was neglected, and it is therefore consistent to do so in the equations above.

Equation (28) is obtained by combining the above results with additional terms resulting from the presence of the air-sea interface. The latter are nonsingular and their contributions to the surface integral are found by simply evaluating the corresponding integrands at the centers of the tiles and multiplying by the respective tile areas.

Appendix D

WIREFRAME ANNEALING

Our wireframes, originally designed for optimal fit on a sphere, suffer distortion when they are projected onto nonspherical plume shapes. In this appendix, we describe the method used to correct that distortion by adapting the wireframe to the new shape.

The goal of the procedure is to produce a nonspherical wireframe whose tiles are, as nearly as possible, identical equilateral triangles. Generally this can only be achieved in an approximate way, so the key is to quantify the phrase "as nearly as possible." For this, we first number the tile edges (the line segments connecting the adjacent vertices) with an index $j = 1, 2, \cdots, L$ and denote the length of the jth edge by e_j. The edge lengths then have a mean value of

$$\mu = \frac{1}{L} \sum_{j=1}^{L} e_j \tag{D1}$$

and an absolute deviation, relative to that mean, of

$$E = \frac{1}{L} \sum_{j=1}^{L} |e_j - \mu| / \mu \geq 0 \ . \tag{D2}$$

We note that E reaches its theoretical minimum value of zero for the ideal wireframe of identical equilateral triangles. If the vertices are allowed to move about on the plume surface, the configuration that minimizes E will approximate that ideal as nearly as possible given the shape of the plume and the topology of the vertex connections. Thus we adopt E as an objective function to be minimized.

With this objective function in hand, we need an efficient method for sampling the vertex configurations and converging to the minimum. The method we chose is a novel synthesis of two well-known techniques — the downhill simplex method and simulated annealing — that was recently implemented as the AMEBSA algorithm*. It provides a natural way to use annealing methods in continuous control spaces. For this approach, a wireframe configuration is specified by the angular coordinates of all the N vertices. Each configuration may be thought of as a point

$$\mathbf{w} = (\theta_1, \phi_1, \theta_2, \phi_2, \cdots, \theta_N, \phi_N) \tag{D3}$$

in a control space of $2N$ dimensions. To initialize the procedure, a simplex of such configurations (a set of $2N + 1$ points in the $2N$-dimensional space) is constructed. The bare downhill simplex algorithm would operate by applying a set of "moves" (reflections, contractions, expansions, or multiple contractions) to the vertices of this simplex, proceeding in the "downhill" direction defined by $E(\mathbf{w})$. AMEBSA enhances that procedure by using simulated annealing to inject an element of randomness into these moves. The result is an algorithm that, as the annealing temperature T

*W. H. Press and S. A. Teukolsky, "Simulated Annealing Optimization over Continuous Spaces," *Comput. Phys.*, Jul/Aug 1991.

is gradually lowered, takes the system point efficiently downhill along any narrow valleys in the control space and at the same time avoids getting stuck in local minima. The procedure is aptly described by AMEBSA's authors as follows*:

> At a finite value of T, the simplex expands to a scale that approximates the size of the region that can be reached at this temperature, and then executes a stochastic, tumbling Brownian motion within that region, sampling new, approximately random points as it does so. The efficiency with which a region is explored is independent of its narrowness (for an ellipsoidal valley, the ratio of its principal axes) and orientation. If the temperature is reduced sufficiently slowly, it becomes highly likely that [the] simplex will shrink into that region containing the lowest relative minimum encountered.

The effectiveness of the method for wireframe optimization can be seen in the following two figures that were generated during the evolution of the annealed ellipsoidal wireframe of Fig. 7 from its unannealed predecessor in Fig. 6. Figure D1 shows the progress of the procedure as a function of the number of annealing iterations. While the annealing temperature is reduced monotonically (according to an empirically determined cooling schedule), the objective function $E(\mathbf{w})$ decreases in a regular way, "freezing" into its minimum value after about 100 iterations. Figure D2 displays the areas of the tiles in the final annealed wireframe. The "northern hemisphere" tiles are on the left in this figure and the "southern hemisphere" tiles are on the right. The left and right halves are nearly identical only because the plume shape on which the annealing was done is symmetric across its equator. The dotted line marks the average tile area and the dashed line indicates a theoretical reference value — the plume area divided by the number of tiles. The average is satisfyingly close to the reference value and there are only a few statistical outliers. These outlier tiles, the ones with areas above 0.01 (tile numbers near 1 and 100) turn out to be the eight tiles connected to the north pole and the corresponding eight at the south pole. The annealing implementation used in this report did not adjust these polar tiles effectively. Although we did not think the effect significant enough to justify recomputing the results in this report, we have devised an improved scheme for future use.

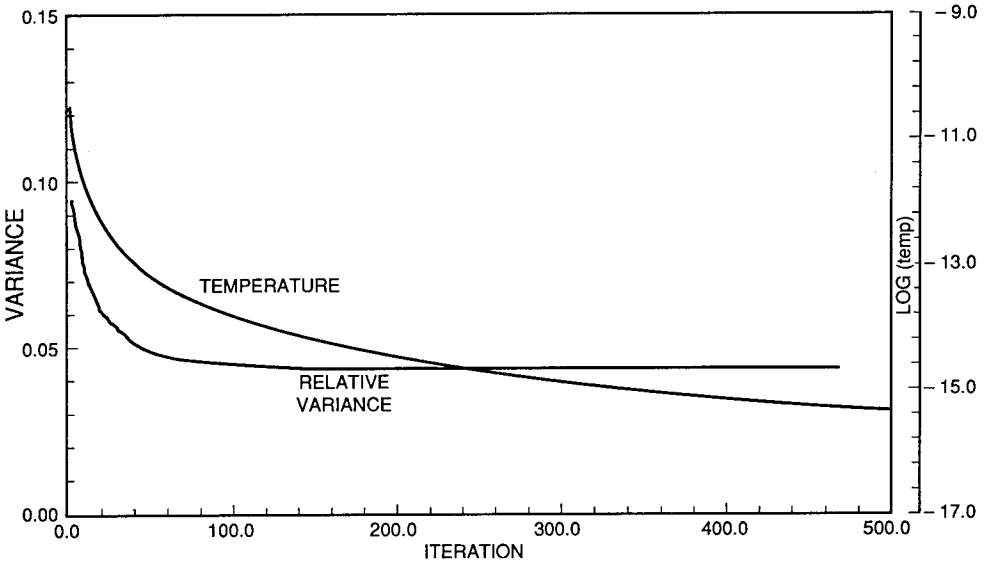

Fig. D1 – Relative variance and temperature as functions of the number of annealing iterations

*ibid.

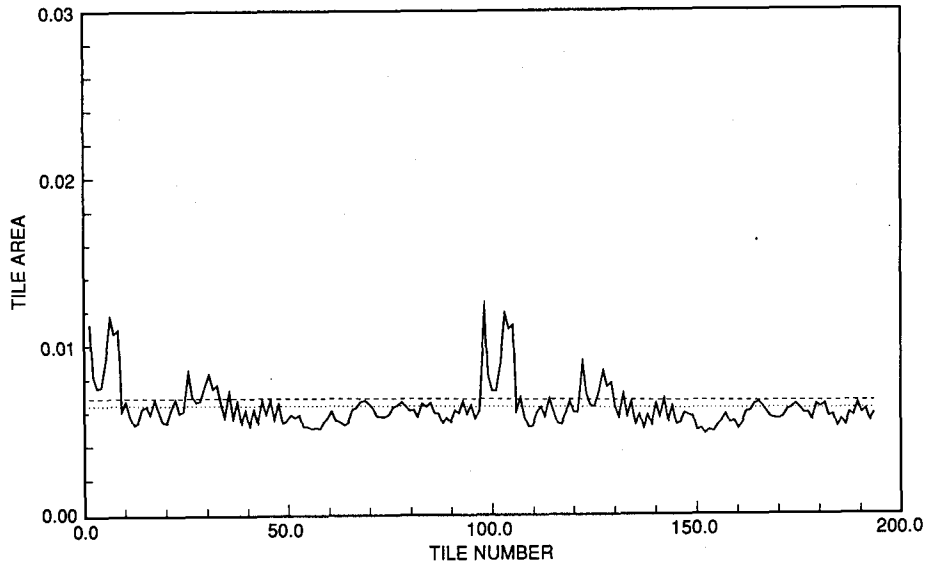

Fig. D2 – Tile areas of the annealed wireframe. The dotted line is the average. The dashed line is the theoretical limit described in the text.

Appendix E

COMPUTATIONAL PRACTICALITY

This appendix investigates the practical issues involved in the computer solution of the discrete continuity condition as proposed in Section 5 of this report.

As noted there, the continuity condition is a $2N$-dimensional linear system of the form

$$\underbrace{\mathsf{M}}_{2N\times 2N}\ \underbrace{\mathsf{x}}_{2N\times 1} = \underbrace{\mathsf{b}}_{2N\times 1} \tag{E1}$$

with a known constant matrix M. First b is calculated and then the system is solved for x. For speed and efficiency, it is desirable to do this entirely "in core." In that case, the need for $(2N)^2$ complex RAM storage locations for M is the critical factor. This storage requirement grows with the square of the number of surface tiles. Since the linear dimension of each tile must remain smaller than an interior wavelength, it is clear that the number of them needed to form a surface wireframe will be proportional to the square of the acoustic frequency. Thus, the storage needed for M will increase in proportion to f^4.

The wireframe approach will always be practical at low enough frequencies, but it will rapidly exhaust the RAM available in any given computing environment as higher frequencies are considered. For a quantitative estimate of the maximum practical frequency, we consider a spherical plume with a diameter D. If $\bar{c}_{int}$ is a typical interior sound speed, then the corresponding interior wavelength at frequency f is $\lambda_{int} = \bar{c}_{int}/f$. The edges of the tiles can be no larger than a fraction $\beta\lambda_{int}$ of this length, where $\beta \lesssim 0.25$ for instance, so that the coherent details of the internal field can be adequately sampled. The area of a typical tile can be expressed as $\alpha(\beta\lambda_{int})^2$ where $\alpha \leq 1$. A square tile, for example, would have $\alpha = 1.0$, while an equilateral triangle would have $\alpha = \sin(60°)/2 = 0.43$. Thus

$$N = \frac{\pi}{\alpha}\left(\frac{Df}{\beta\bar{c}_{int}}\right)^2. \tag{E2}$$

For the present numerical estimate we use triangular tiles whose sides are one quarter of an interior wavelength on average; i.e., $\alpha = 0.5$, $\beta = 0.25$. Tables E1 through E3 list the resulting values of $2N$ for D values ranging from 1 to 3 meters and f in the band $[50, 300]$ Hz with $\bar{c}_{int} = 100$, 200, and 300 m/s. If we suppose that the available RAM is 8 MB, then at 4 bytes per single precision real number (as on a VAX machine), M, a single-precision complex matrix, can be held "in core" provided that

$$2N \leq \left(\frac{8\times 10^6}{2\times 4}\right)^{1/2} = 1000.$$

Inspection of these tables confirms that most realistic plume diameters and frequencies can be handled.

Table E1 – $2N$ for typical f and D values with $\bar{c}_i = 100$ m/s

	50 Hz	100 Hz	150 Hz	200 Hz	250 Hz	300 Hz
1 m	50	201	452	804	1256	1809
2 m	201	804	1809	3216	5026	7238
3 m	452	1809	4071	7238	11309	16286

Table E2 – $2N$ for typical f and D values with $\bar{c}_i = 200$ m/s

	50 Hz	100 Hz	150 Hz	200 Hz	250 Hz	300 Hz
1 m	12	50	113	201	314	452
2 m	50	201	452	804	1256	1809
3 m	113	452	1017	1809	2827	4071

Table E3 – $2N$ for typical f and D values with $\bar{c}_i = 300$ m/s

	50 Hz	100 Hz	150 Hz	200 Hz	250 Hz	300 Hz
1 m	5	22	50	89	139	201
2 m	22	89	201	357	558	804
3 m	50	201	452	804	1256	1809

Appendix F

PARTIAL WAVE COMPUTATION

This appendix deals with acoustic scattering from a spherical fluid body whose interior sound speed is a function of the radial coordinate only. The analytic approach to the problem is briefly reviewed first and then a numerical implementation is developed. The close analogy to quantum-mechanical scattering from a spherically symmetric potential is exploited by following, wherever possible, the analytic treatment of the problem in Mertzbacher's popular text [F1] and by adopting the notation used there.

The scattering body is embedded in a uniform fluid medium and both of them have the same density. The acoustic field for this situation obeys

$$\left(\frac{\partial}{\partial \mathbf{r}} \cdot \frac{\partial}{\partial \mathbf{r}} + T(r,k) \right) U(\mathbf{r},k) = 0 \tag{F1}$$

where $k = \omega/c_{ext}$ is the exterior wavenumber, $n(r) = c_{ext}/c(r)$ is the refractive index, and $T(r,k) = n^2(r)k^2$ is the square wavenumber at r — the analog of the kinetic energy in the Schrodinger equation.

F1. PARTIAL-WAVE ANALYSIS

In spherical coordinates $\mathbf{r} = (r, \theta, \phi)$, the partial wave series

$$U(\mathbf{r},k) = \sum_{\ell=0}^{\infty} \sum_{m=-\ell}^{+\ell} U_{\ell m} Y_\ell^m(\theta,\phi) u_\ell(r,k)/r \tag{F2}$$

applies with each radial eigenfunction $u_\ell(r,k)$ satisfying

$$u_\ell''(r,k) + K_\ell(r,k) u_\ell(r,k) = 0 \tag{F3}$$

where

$$K_\ell(r,k) = T(r,k) - \ell(\ell+1)/r^2 \tag{F4}$$

is the "kinetic energy" with the centrifugal term included. When $\ell > 0$, the differential equation is singular at the origin. The physical solution is the one for which $u_\ell(r,k)/r$ remains bounded.

The elastic scattering amplitude has the partial wave series $F(\vartheta,k) = \sum_{\ell=0}^{\infty} F_\ell(\vartheta,k)$, where ϑ is the scattering angle and

$$F_\ell(\vartheta,k) = (2\ell+1) P_\ell(\cos\vartheta) \times \alpha_\ell(k)/k \; . \tag{F5}$$

The first factor is a known real quantity and the second involves the complex expression

$$\alpha_\ell(k) = e^{i\delta_\ell(k)} \sin\delta_\ell(k) \tag{F6}$$

in which $\delta_\ell(k)$ is the ℓth phase shift. For a body of radius a, classical arguments [F1, pages 234-235] indicate that the series can be terminated at roughly $\ell = b \stackrel{def}{=} ka$.

The problem of calculating F, then, reduces to finding a finite number of these α_ℓ terms. This is customarily done with the aid of the real-valued auxiliary quantities $\xi_\ell(k)$, $s_\ell(k)$, $\Delta_\ell(k)$, $\beta_\ell(k)$ which satisfy

$$\exp\left(i2\xi_\ell(k)\right) = -\frac{h_\ell^{(2)}(b)}{h_\ell^{(1)}(b)} \tag{F7a}$$

$$s_\ell(k) = \frac{1}{b|h_\ell^{(1)}(b)|^2} \tag{F7b}$$

$$\Delta_\ell(k) = -is_\ell(k) + b\frac{h_\ell^{(1)\prime}(b)}{h_\ell^{(1)}(b)} \tag{F7c}$$

$$\beta_\ell(k) = \left(\frac{a}{u_\ell(r,k)}\frac{du_\ell(r,k)}{dr}\right)_{r=a} - 1 \tag{F7d}$$

where $h_\ell^{(1)}$, $h_\ell^{(2)}$ are spherical Hankel functions and $'$ indicates differentiation with respect to the argument. $\beta_\ell(k)$ is the log-derivative of the radial factor $u_\ell(r,k)/r$ at $r = a$ and ξ_ℓ is the $\beta_\ell \to 0$ "hard sphere" limit of δ_ℓ. In terms of these quantities, Eq. (F6) becomes

$$\alpha_\ell = e^{i2\xi_\ell}\left(\frac{s_\ell}{\beta_\ell - (\Delta_\ell + is_\ell)} + e^{-i\xi_\ell}\sin\xi_\ell\right) . \tag{F8}$$

Another quantity of some interest is the S-matrix eigenvalue

$$S_\ell(k) = \exp\{i2\delta_\ell(k)\} \tag{F9a}$$

$$= \exp\{i2\xi_\ell(k)\}\left\{1 + b\frac{\frac{h_\ell^{(1)\prime}(b)}{h_\ell^{(1)}(b)} - \frac{h_\ell^{(2)\prime}(b)}{h_\ell^{(2)}(b)}}{\beta_\ell(k) - b\frac{h_\ell^{(1)\prime}(b)}{h_\ell^{(1)}(b)}}\right\} \tag{F9b}$$

which is the ratio of outgoing and incoming amplitudes in the ℓth radial factor.

It is convenient to formulate the numerical computations in terms of ordinary cylinder functions by exploiting the following standard expressions [F2]

$$q_\nu(x) = \sqrt{\frac{\pi}{2x}}Q_{\nu+1/2}(x) \tag{F10}$$

$$Q'_\nu(x) = -Q_{\nu+1}(x) + \frac{\nu}{x}Q_\nu(x) \tag{F11}$$

in which ν is any real index, Q is one of the cylinder functions $J, Y, H^{(1)}, H^{(2)}$ and q is its spherical counterpart among $j, y, h^{(1)}, h^{(2)}$. Specific forms used in the following are

$$\frac{h_\ell^{(2)}(x)}{h_\ell^{(1)}(x)} = \frac{H_{\ell+1/2}^{(2)}(x)}{H_{\ell+1/2}^{(1)}(x)} \tag{F12}$$

$$\frac{h_\ell^{(1)\prime}(b)}{h_\ell^{(1)}(b)} = \left(\frac{h_\ell^{(2)\prime}(b)}{h_\ell^{(2)}(b)}\right)^* = \frac{\ell H_{\ell+1/2}^{(1)}(b) - bH_{\ell+3/2}^{(1)}(b)}{bH_{\ell+1/2}^{(1)}(b)} . \tag{F13}$$

The computation of α_ℓ proceeds as follows:

- Find $\exp\{i2\xi_\ell(k)\}$ by Eq. (F7a),
- Compute $\xi_\ell(k) = \arg\left(\exp\{i2\xi_\ell(k)\}\right)/2$,
- Compute $s_\ell(k)$ by Eq. (F7b),
- Evaluate $\beta_\ell(k)$ by solving Eq. (F3),
- Find $\Delta_\ell(k)$ from Eq. (F7c), and
- Find $\alpha_\ell(k)$ from Eq. (F8).

To aid in the interpretation of results, one may also compute:

- $S_\ell(k)$ by Eq. (F9b)
- $\delta_\ell(k) = \arg\left(\exp\{i2\delta_\ell(k)\}\right)/2$.

$\xi_\ell(k)$, $s_\ell(k)$ and $\Delta_\ell(k)$ require nothing more than some well-known special functions. The crux of the matter is to compute $\beta_\ell(k)$ by integrating the radial equation from $r = 0$ to a.

F2. SOLUTION OF THE RADIAL EQUATION

With k and ℓ dependence suppressed for the moment, the definitions $v = u'$ and

$$\begin{aligned} \mathsf{U}(r) &= \begin{pmatrix} u(r) \\ v(r) \end{pmatrix} \\ \mathsf{A}(r) &= \begin{pmatrix} 0 & 1 \\ -K(r) & 0 \end{pmatrix} \end{aligned} \tag{F14}$$

put the radial equation into the form

$$\mathsf{U}'(r) - \mathsf{A}(r)\mathsf{U}(r) = 0\ . \tag{F15}$$

The evolution of $\mathsf{U}(r)$ from some point $r = \rho$ to $r = a$ can be expressed in terms of $\mathsf{P}(a, \rho)$, the propagator matrix [F3]

$$\mathsf{U}(a) = \mathsf{P}(a, \rho)\mathsf{U}(\rho). \tag{F16}$$

$\mathsf{P}(a, \rho)$ performs the transformation from initial values given at ρ to final values at a and usually needs to be found by numerical integration. For this we use an adaptation of the trusty fourth order Runge-Kutta routine in *Numerical Recipes* [F4]. The implementation is fairly straightforward with special attention needed for only two details, namely the singularity of the equation at the origin and the numerical instability that can occur in intervals where $K(r)$ is negative. These are discussed below.

F2.1 Singularity

For $\ell = 0$, the origin is a regular point of Eq. (F3), and Eq. (F16) can be invoked with $\rho = 0$ using the initial value

$$\mathsf{U}(0) = \begin{pmatrix} 0 \\ 1 \end{pmatrix} . \tag{F17}$$

For $\ell > 0$, this cannot be done because the origin is a singular point. Instead, we first find an analytic approximation for the regular solution $\mathsf{U}(\rho)$ at a point ρ near the origin, and then apply Eq. (F16). The Taylor expansion

$$c(r) = c(0) + \gamma r + \cdots , \tag{F18}$$

where γ is the radial derivative at the origin, implies a similar series

$$n^2(r) = n^2(0) \left(1 - \frac{2\gamma}{c(0)} r + \cdots\right) \tag{F19}$$

for the square of the refractive index. Thus, $2|\gamma|r/c(0)$ estimates the fractional error incurred in approximating n^2 by its value at the origin. To put it another way, for a set tolerance δ, the estimate $n^2(r) \approx n^2(0)$ is valid out to a radius

$$\tilde{r} = \frac{c(0)\delta}{2|\gamma|} . \tag{F20}$$

The approximate radial equation in the interval $[0, \tilde{r}]$, i.e., Eq. (F3) with

$$K_\ell(r, k) = T(0, k) - \ell(\ell + 1)/r^2 , \tag{F21}$$

has a regular solution that is easily found to be proportional to

$$r^{\ell+1} \left(1 + \frac{T(0,k)}{4\ell + 6} r^2 + \cdots\right) . \tag{F22}$$

To a fixed tolerance η, then, $u \propto r^{\ell+1}$ and $u/v = \rho/(\ell + 1)$ out to a radius

$$\hat{r} = \sqrt{\eta \frac{4\ell + 6}{T(0,k)}} . \tag{F23}$$

Thus, finally, we find that the proper initial value for Eq. (F16) is

$$\mathsf{U}(\rho) = \begin{pmatrix} \rho \\ \ell + 1 \end{pmatrix} \tag{F24}$$

at the starting point $\rho = \min(\tilde{r}, \hat{r})$.

F2.2 Stability

Because the eigenvalues of $\mathsf{A}(r)$ are $\mu(r) = \pm\sqrt{-K(r)}$, the character of the solution $\mathsf{U}(r)$ depends on the sign of $K(r)$. When it is positive, the fundamental solutions that make up $\mathsf{U}(r)$ are both sinusoidal. Since neither of them grows to dominate the other, the numerical ode-solver has no trouble. For negative $K(r)$, however, the fundamental solutions are exponential, with one of

them growing and the other decaying. Whatever the computer wordlength, if K remains negative over a large enough interval, these exponentials will eventually differ so greatly that the ode-solver will be unstable due to roundoff error. In the present case, the most convenient remedy for this is to generate the solution in a series of sufficiently short subintervals and "re-orthogonalize" [F5].

An estimate of what is "sufficiently short" can be based on the case where K is constant over an interval $[r_i, r_f]$ of length $w = |r_f - r_i|$. Here the fundamental solutions starting from r_i are $\exp(+|r - r_i|\mu)$ and $\exp(-|r - r_i|\mu)$. For initial values to be faithfully propagated to r_f without significant roundoff problems, the wordlength must be sufficient for the computer to distinguish $\exp(-2w\mu)$ from $0 + \exp(-2w\mu)$. The requirement is $\exp(-2w\mu) = B\epsilon$ where ϵ is the machine roundoff and B is a large number. Thus,

$$w_{max}(\mu) = -\log(B\epsilon)/2\mu \tag{F25}$$

is the largest interval that the ode-solver can be expected to handle correctly. For $\epsilon = 10^{-6}$ (typical of VAX machines) and $B = 10^3$, for instance, $w_{max}(\mu) = 3.5/\mu$.

In the general nonuniform case, we denote the maximum eigenvalue over the interval by $\bar{\mu}$ and refine the interval into N equal subintervals $[r_i, r_1], [r_1, r_2], \cdots, [r_{N-1}, r_f]$, each much shorter than $w_{max}(\bar{\mu})$. With that done, we may compute the solution at r_f without significant roundoff problems by

$$\mathsf{U}(r_f) = \{\mathsf{P}(r_f, r_{N-1})\{\mathsf{P}(r_{N-1}, r_{N-2}) \cdots \{\mathsf{P}(r_2, r_1)\{\mathsf{P}(r_1, r_i)\}\} \cdots\}\}\mathsf{U}(r_i) \tag{F26}$$

in which the ode-solver is invoked to compute each of the P's. Since $\mathsf{P}(r, r_j)$ is the solution to the initial value problem [F3]

$$\mathsf{P}'(r, r_j) - \mathsf{A}(r)\mathsf{P}(r, r_j) = 0 \tag{F27}$$

$$\mathsf{P}(r_j, r_j) = 1, \tag{F28}$$

we can generate $\mathsf{P}(r_{j+1}, r_j)$ by simply applying the ode-solver twice, with each application using one column of the unit matrix as initial values. The order of operations mandated by the curly brackets is crucial. The ordering

$$\mathsf{U}(r_f) = \{\mathsf{P}(r_f, r_{N-1})\{\mathsf{P}(r_{N-1}, r_{N-2}) \cdots \{\mathsf{P}(r_2, r_1)\{\mathsf{P}(r_1, r_i)\mathsf{U}(r_i)\}\} \cdots\}\}, \tag{F29}$$

while analytically identical to Eq. (F26), is numerically equivalent to $\mathsf{U}(r_f) = \mathsf{P}(r_f, r_i)\mathsf{U}(r_i)$ and thus does nothing at all to alleviate roundoff troubles.

F3. SAMPLE RESULTS

For the following results, the scattering body is one meter in radius and the exterior speed is 1500 m/s. Figure 10 displays $|F(\vartheta, k)|$ together with $|F_\ell(\vartheta, k)|$ for $\ell = 0, \cdots, 3$ as functions of frequency. The scattering angle is 45° and the interior sound speed is a uniform 500 m/s. Resonances are to be expected near the frequencies $f_n = n \times 125$ Hz indicated by a "back of the envelope" calculation using $c_{ext} = \infty$. These are confirmed in that figure. Figure F1 shows the modulus of the total scattering amplitude as a function of frequency for the same situation except that the interior sound speed is a linear function of radius. The average sound speed $(c(0) + c(a))/2$ is held at 500 m/s as in Fig. 10 by shifting $c(0)$ and $c(a)$ by multiples of 10 m/s

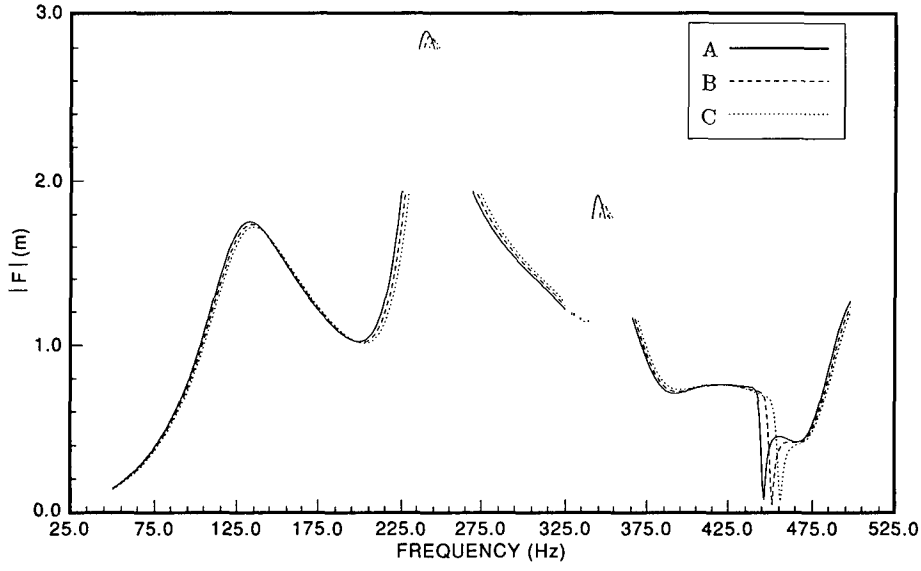

Fig. F1 – $|F|$ as a function of f at $\vartheta = 45°$. $c_{int}(r)$ is linear with $c_{int}(0), c_{int}(a)$ taking on the following values: (A) 500, 500 m/s; (B) 490, 510 m/s; (C) 480, 520 m/s.

in opposite senses. The figure illustrates a maxim of scattering theory: the *average* sound speed determines the lowest resonance and the finer details of $c_{int}(r)$ impact the higher resonances. Figure F2 shows the dependence of the total scattering amplitude on angle as well as frequency for the same case investigated in Fig. 10. In this figure, f is varied in 1 Hz steps over the range [50 Hz, 500 Hz] and ϑ extends from 10° (near backscatter) to 170° (near forward scatter) in 10° increments. The resonances are clearly visible as ridgelike structures parallel to the angle axis. Because of the symmetry of the problem, each of them can be associated with a unique ℓ. As expected, the ℓth resonance exhibits an $(\ell + 1)$-lobed angular structure.

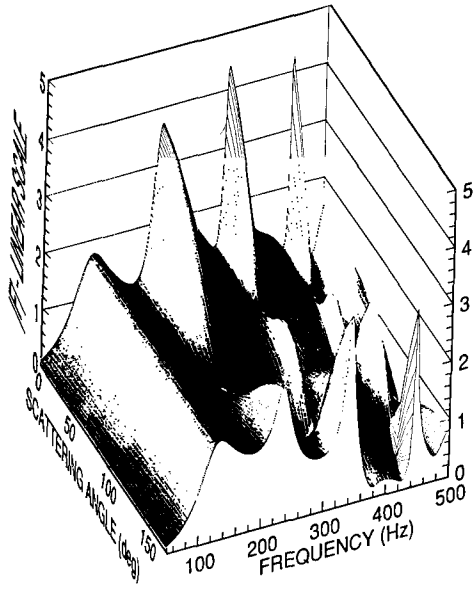

Fig. F2 – $|F|$ as a function of f and ϑ for the same case as Fig. 10

REFERENCES

F1. E. Mertzbacher, *Quantum Mechanics* (Wiley & Son, New York, 1961).

F2. M. Abramowitz and I. A. Stegun, *Handbook of Mathematical Functions* (Dover, New York, 1972).

F3. J. D. Dollard and C. N. Friedman, *Product Integration with Applications to Differential Equations*, Vol. 10 of *The Encyclopedia of Mathematics and its Applications*, G.-C. Rota, ed. (Addison-Wesley, Reading, MA, 1979).

F4. W. H. Press, B. P. Flannery, S. A. Teukolsky, and W. T. Vetterling, *Numerical Recipes* (Cambridge University Press, Cambridge, 1986).

F5. A. Davey, "A Simple Numerical Method for Solving Orr-Sommerfeld Problems," *Q. Jl. Mech. Appl. Math.* **XXVI**, 401–411 (1973).

Appendix G

RELATION TO EARLIER WORK

This appendix provides further details about the place of our work within the context of earlier efforts.

G1. RELATED PROBLEMS

Among the scattering problems that are close kin to ours, the simplest are the exterior problems. These deal with impenetrable targets. Some fixed boundary condition is imposed on the surface and the scattered field is inferred in the exterior. The first of such problems to be solved involved scattering from symmetric bounded shapes. Reference G1, for example, derives the scattering amplitudes for shapes such as spheres and spheroids with either hard or soft boundary conditions as closed-form expressions involving special functions. But that approach is practical in only a few cases. A more comprehensive approach is described in Ref. G2, which treats electromagnetic scattering from perfect conductors of arbitrary shape, addressing both analytic methods and computer implementation. An extension of this type of problem is the treatment of scattering from bossed surfaces [G3, G4]. In such problems, boundary conditions are applied on an infinite planar target with irregularities, the bosses, protruding from it at regular or random locations. Here again, classical methods based on special functions can produce valuable results when the bosses have simple shapes. Any scattering situation is essentially an exterior problem if the target is either totally absorbing or totally reflecting, but these two extremes do not cover the important cases in which the target is penetrable.

Scattering from a penetrable object is necessarily an interior/exterior problem. On the surface of the object, physical continuity conditions, rather than extinction conditions, are applied and these serve to connect the interior and exterior wave solutions. In such problems, the target's internal structure is important. Penetrable targets with spherical symmetry have been analyzed with great success using methods that were perfected in the quantum mechanical study of scattering from radial potentials [G5]. The main effect of the interior structure is the occurrence of resonances — analogs of the nearly bound "virtual states" in atomic scattering. For individual bubbles, the lowest-frequency resonance, a monopole feature, has been analyzed with special thoroughness [G6]. Scattering from spatial arrays of such resonant monopoles has received considerable attention [G7, G8] and collective effects have been recognized. These particular analyses have been limited to small, precisely positioned arrays and have focused on coherent phenomena such as "superresonance" [G9–G11]. However, incoherent collective effects in large-scale ensembles of elementary scatterers have also been analyzed. As will be described in more detail shortly, the fundamental acoustic result of introducing large numbers of bubbles into water is an incoherent effect — the reduction of the effective sound speed in the medium. Scattering from plumes formed of such anomalously slow bubbly water clearly is an interior/exterior problem. Traditional methods are adequate for simple shapes with homogeneous interiors, but more realistic cases call for a theoretical approach that is both comprehensive and numerically implementable.

G2. BOUNDARY INTEGRAL EQUATION METHODS

Both direct and indirect numerical approaches are possible for the general scattering problem. Direct methods operate by first generating a 3-D grid throughout the target and some of the surrounding medium and then applying a finite difference solution method on the grid. This straightforward approach has its drawbacks. One of these is the large number of mesh points needed for the 3-D grid. Another is the strong dependence of solutions on the dissipation/dispersion properties of the finite difference method that is used. Boundary integral equation (BIE) methods circumvent those problems by an indirect approach. They need far fewer mesh points since they use a 2-D grid (on the target surface). They also readily incorporate the far-field limit. BIE methods begin by formulating the scattering problem in terms of 3-D volume integrals. They then exploit Green's integral identities to convert these to 2-D integrals over the target surface. The main historical drawbacks connected with the BIE approach have been (a) nonuniqueness of the solution at interior resonance frequencies and (b) troublesome ($1/r^3$) singularities in the surface integrands. Recently, however, it has been discovered that a more adroit BIE formulation can eliminate both of these.

The earliest applications of BIE methods were to exterior scattering problems. As Lamb explained long ago [G12, article 290], direct application of an elementary BIE approach in this case fails to produce a unique solution at the eigen-frequencies of the corresponding interior problem. However, this no longer constitutes a barrier to the use of the method. Techniques have been developed to overcome the nonuniqueness difficulty where it occurs [G13, G14] so that BIE methods are now in common use [G15–G17]. Besides, many important exterior problems lie outside the troublesome frequency range [G18].

It should be emphasized that the exterior scattering problem itself is mathematically well-posed. When nonuniqueness occurs in BIE solutions, it is an artifact of the particular way the BIE method is formulated. The same is true of the interior/exterior scattering problem. Here, however, techniques to preserve uniqueness have never been widely used. Indeed, they have not been needed at all since Kittappa and Kleinman [G19] developed an interior/exterior BIE formulation with explicitly unique and stable solutions [G20]. Actually, Ref. G19 demonstrates uniqueness for only a restricted range of wavenumbers, but the proof is extended in Ref. G21 to all realistic wavenumbers.

Reference G19 also provides a means of "regularizing" the singular kernels in the surface integrals, i.e., isolating the singular parts into a separate term which is manifestly well-behaved. This regularized expression appears to be a promising starting point for further analysis. We do not use it here because it does not seem to facilitate numerical computations. In numerical applications, the weak singularity of the kernels has been handled either by boundary displacement [G15] or, more recently, by variational reformulation of the problem [G18, G22]. Since neither of these techniques seemed appealing from a practical standpoint for targets with arbitrarily specified shapes and interiors, we identified and dealt with the singularities using our own method.

G3. TREATMENT OF BUBBLY MEDIA

The rigorous theory of wave propagation in media containing large random distributions of scatterers (bubbly liquids, for instance) has been formulated in the full nonlinear by Caflisch et al. [G23]. The result essentially validates the earlier heuristic, physically motivated results of

van Wijngaarten [G24]. Prosperetti et al. [G25] have developed an approach that is especially suited to describing the internal dynamics of the bubbles themselves. The linearized theory was presented by Fouldy [G26] and somewhat later by Lax [G27]. Over the past decade and a half, Prosperetti and his co-workers have further developed the mathematical language needed for sound propagation through a bubbly medium [G28–G31]. This work has shown that a bubbly mixture can be modeled as a fluid characterized by a complex effective index of refraction [G30]. For frequencies well below the resonance frequency of the individual bubbles, the index of refraction is real and given by the well-known Minneart formula [G32, G33].

G4. SCATTERING FROM NEAR-SURFACE BUBBLE STRUCTURES

More recently this group has applied these results to studies of the related questions of ambient noise due to bubble structures in the ocean and acoustic scattering from these structures [G32, G34, G35]. As a first calculation, Prosperetti et al. [G32] considered a hemisphere under a flat surface. They solved the problem by the method of partial waves and used the results to estimate backscattering strengths in the ocean, obtaining values compatible with the Chapman-Harris curves. The effects of radial layering in such clouds were also considered and were found to be of minor importance.

Sarkar and Prosperetti [G35] examined the sensitivity of the scattering cross-section to the shape of the cloud (again, for clouds attached to the surface). They first used a T-matrix method. This approach can, in principle, provide scattering solutions for hemispheroids or cones. However, it turns out that the T-matrix technique is not very well behaved numerically. The situation deteriorates as the frequency is decreased, and the problems also get worse the greater the difference between the cloud's radius and depth. To handle this situation, they obtained a perturbative solution valid for small cloud depths, where the bubble structure is approximated by a boss rather than by a penetrable cloud.

REFERENCES

G1. J. J. Bowman, T. B. A. Senior, and P. L. E. Uslenghi, eds., *Electromagnetic and Acoustic Scattering from Simple Shapes* (North-Holland, Amsterdam, 1969).

G2. A. K. Aziz, M. R. Dorr, and R. B. Kellogg, "Calculation of Electromagnetic Scattering by a Perfect Conductor," *J. Comp. Phys.* **45**, 403–416 (1982).

G3. R. J. Lucas and V. Twersky, "Low-Frequency Reflections and Scattering by Ellipsoidally Embossed Surfaces," *J. Acoust. Soc. Am.* **78**, 1838–1850 (1985).

G4. R. J. Lucas and V. Twersky, "High-Frequency Reflections and Scattering by Ellipsoidally Embossed Surfaces," *J. Acoust. Soc. Am.* **83**, 2005–2011 (1988).

G5. K. A. Sage, J. George, and H. Überall, "Multipole Resonances in Sound Scattering from Gas Bubbles in a Liquid," *J. Acoust. Soc. Am.* **65**, 1413–1422 (1979).

G6. G. Gaunard, K. P. Scharnhorst, and H. Überall, "Giant Monopole Resonances in the Scattering of Waves from Gas-filled Spherical Cavities and Bubbles," *J. Acoust. Soc. Am.* **65**, 573–594 (1979).

G7. V. Twersky, "Multiple Scattering by Finite Regular Arrays of Resonators," *J. Acoust. Soc. Am.* **87**, 25–41 (1990).

G8. V. Twersky, "Regular Polygonal Arrays of Resonant Scatterers," *J. Acoust. Soc. Am.* **89**, 991–998 (1991).

G9. I. Tolstoy, "Properties of Superresonant Systems of Scatterers," *IEEE J. Oceanic Eng.* **OE-12**, 327–332 (1987).

G10. I. Tolstoy and A. Tolstoy, "Superresonant Systems of Scatterers. II," *J. Acoust. Soc. Am.* **83**, 2086–2096 (1988).

G11. I. Tolstoy and A. Tolstoy, "Line and Plane Arrays of Resonant Monopole Scatterers," *J. Acoust. Soc. Am.* **87**, 1038–1043 (1990).

G12. H. Lamb, *Hydrodynamics*, 6th ed (Dover, New York, 1945).

G13. H. A. Schenck, "Improved Integral Formulation for Acoustic Radiation Problems," *J. Acoust. Soc. Am.* **44**, 41–58 (1967).

G14. A. J. Burton and G. F. Miller, "The Application of Integral Equation Methods to the Numerical Solution of some Exterior Boundary-value Problems," *Proc. Roy. Soc. Lond. Ser. A* **323**, 201–210 (1971).

G15. K. A. Cunefare, G. Koopmann, and K. Brod, "A Boundary Element Method for Acoustic Radiation Valid for all Wavenumbers," *J. Acoust. Soc. Am.* **85**, 39–48 (1989).

G16. A. F. Seybert, B. Soenarko, F. J. Rizzo, and D. J. Shippy, "An Advanced Computational Method for Radiation and Scattering of Acoustic Waves in Three Dimensions," *J. Acoust. Soc. Am.* **77** 362–368 (1985).

G17. A. F. Seybert and D. K. Casey, "An Integral Equation Method for Coupled Fluid/Fluid Scattering in Three Dimensions," *J. Acoust. Soc. Am.* **84**, 379–384 (1988).

G18. P. Malbéqui, S. M. Candel, and E. Rignot, "Boundary Integral Calculations of Scattered Fields: Application to a Spacecraft Launcher," *J. Acoust. Soc. Am.* **82**, 1771–1781 (1987).

G19. R. Kittappa and R. E. Kleinman, "Acoustic Scattering by Penetrable Homogeneous Objects," *J. Math. Phys.* **16**, 421–432 (1975).

G20. G. T. Schuster and L. C. Smith, "A Comparison among Four Direct Boundary Integral Methods," *J. Acoust. Soc. Am.* **77**, 850–864 (1985).

G21. R. Kress and G. F. Roach, "Transmission Problems for the Helmholtz Equation," *J. Math Phys.* **19**, 1433–1437 (1988).

G22. M. A. Hamdi, "Une Formulation Variationnelle par Équations Intégrales pour la Résolution de l'Équation de Helmholtz avec des Conditions aux Limites Mixtes," *Compt. Rend. Acad. Sc. Paris* **292** (1991).

G23. R. E. Caflisch, M. J. Miksis, G. C. Papanicolaou, and L. Ting, "Effective Equations for Wave Propagation in Bubbly Liquids," *J. Fluid Mech.* **153**, 259–273 (1985).

G24. L. van Wijngaarten, "On Equations of Motion for Mixtures of Liquid and Gas Bubbles," *J. Fluid Mech.* **33**, 465–474 (1968).

G25. A. Prosperetti, L. A. Crum, and K. W. Commander, "Nonlinear Bubble Dynamics," *J. Acoust. Soc. Am.* **83**, 505–513 (1988).

G26. L. L. Fouldy, "The Multiple Scattering of Waves, I. General Theory of Isotropic Scattering by Randomly Distributed Scatterers," *Phys. Rev.* **67**, 107–119 (1945).

G27. M. Lax, "Multiple Scattering of Waves," *Rev. Mod. Phys.* **23**, 287–310 (1951).

G28. A. Prosperetti, "Thermal and Damping Mechanisms in the Forced Radial Oscillations of Gas Bubbles in Liquids," *J. Acoust. Soc. Am.* **61**, 17–27 (1977).

G29. A. Prosperetti, "A Model of Bubbly Liquids," *J. Wave-Mater.* **1**, 413–432 (1986).

G30. K. W. Commander and A. Prosperetti, "Linear Pressure Waves in Bubbly Liquids: Comparison Between Theory and Experiment," *J. Acoust. Soc. Am.* **85**, 732–746 (1989).

G31. A. Prosperetti and A. Lezzi, "Bubble Dynamics in a Compressible Liquid. Part 1. First-order Theory," *J. Fluid Mech.* **168**, 457–478 (1986).

G32. A. Prosperetti, N. Q. Lu, and H. S. Kim, "Active and Passive Acoustic Behavior of Hemispherical Bubble Clouds," *J. Acoust. Soc. Am.*, in press.

G33. M. Minneart, "On Musical Air Bubbles and the Sound of Running Water," *Phil. Mag.* **16**, 235-248 (1933).

G34. N. Q. Lu and A. Prosperetti, "Active and Passive Acoustic Behavior of Bubbly Layers," *J. Acoust. Soc. Am.*, in press.

G35. K. Sarkar and A. Prosperetti, "Backscattering of Underwater Noise by Bubble Clouds," *J. Acoust. Soc. Am.*, submitted.